UNIVERSITY OF CONCEPCIÓN
FACULTY OF PHYSICAL SCIENCES AND MATHEMATICS

WISE2MBH

A scaling-based algorithm for probing supermassive black hole masses through WISE photometry

By: Joaquín Hernández Yévenes

Thesis presented to the Faculty of Physical Sciences and Mathematics of the University of Concepción to obtain the Masters Degree in Astronomy

January, 2024
Concepción, Chile

Advisor: Neil Nagar
Department of Astronomy

Pierdes años en la vida y, frente a la muerte, mendigas un momento.

You lose years in life and, in the face of death, you beg for a moment.

Nicolae Iorga

Agradecimientos

Quisiera agradecer a todos quienes estuvieron presentes durante este proceso (para nada sencillo) del Magíster. Fue un periodo de bastantes sorpresas, altos, bajos, pero por sobre todo, experiencias, y es de eso de lo que aprendemos.

A mi familia, Carolina y Marcelo, madre y padre que siempre estuvieron conmigo, dándome su apoyo y cariño de manera incondicional durante estos 6 años de universidad, en especial estos últimos 2 años de Magíster, donde más experiencias he vivido. A Marcelo y Carolina, hermano y cuñada (chistoso, ¿no?) que siempre han dado espacio para que yo pueda estar con ellos en Valdivia, ya mi segunda casa a esta altura, sabiendo dar lo mejor de ellos, a pesar de estar aprendiendo aún la convulsa vida de casados. Y no quiero dejar fuera a mis queridas abuelitas, tías, tíos, primos y primas con quienes he compartido bonitas jornadas estos años. Un gran saludo a mis abuelos Luis y Artemio (Q.E.P.D.), sé que esto significaría mucho para ellos.

A absolutamente todos mis amigos, no hay forma de que pueda mencionarlos a todos, he aprendido a disfrutar cada momento que puedo con ellos, a apoyarlos, a conversar de todo con tal de lograr algo positivo en ellos, porque he aprendido que nada es más satisfactorio que ver bien a tus amigos, personas por las que verdaderamente me preocupo.

A todos los académicos que supieron darme una mano cuando la necesité, Dhanya, Yuri, Thomas, Angelo, Dominic y por sobre todo a mi guía, Neil, quien vio algo en mí, un potencial que yo no podía ver en su momento, brindándome apoyo, oportunidades y consejos para seguir con mi trabajo y desarrollar mejor mi potencial como astrónomo. A día de hoy siento que no sería la misma persona ni hubiera aprendido tanto en estos 2 años si no hubiera sido por él. Muchas gracias, Neil.

Y por último, gracias Hardstyle, querido Hardstyle.

Acknowledgements

I would like to thank everyone who was present during this (by no means simple) Master's journey. It was a period of many surprises, highs, lows, but above all, experiences, and that is what we learn from.

To my family, Carolina and Marcelo, my mother and father who have always been with me, giving me their support and unconditional love during these 6 years of university, especially these last 2 years of the Master's, where I have lived many experiences. To Marcelo and Carolina, brother and sister-in-law (funny, isn't it?) who have always made space for me to be with them in Valdivia, now my second home at this point, showing the best of themselves, despite still learning the tumultuous life of marriage. And I don't want to leave out my dear grandmothers, aunts, uncles and cousins with whom I have shared beautiful moments over these years. A big greeting to my grandparents Luis and Artemio (R.I.P.), I know this would mean a lot to them.

To absolutely all my friends, there is no way I can mention everyone. I have learned to enjoy every moment I can with them, to support them, to talk about everything in order to achieve something positive in their lives, because I have learned that nothing is more satisfying than seeing your friends doing well, people I truly care about.

To all the academics who knew how to lend me a hand when I needed it, Dhanya, Yuri, Thomas, Angelo, Dominic, and above all, to my advisor, Neil, who saw something in me, a potential that I couldn't see at the time, offering me support, opportunities, and advice to continue with my work and develop my potential as an astronomer. Today, I feel that I wouldn't be the same person or have learned so much in these 2 years if it hadn't been for him. Thank you very much, Neil.

And lastly, thanks Hardstyle, dear Hardstyle.

Resumen

Los Agujeros Negros Supermasivos (SMBHs) se encuentran comúnmente en el centro de galaxias masivas. Estimar sus masas (M_{BH}) es crucial para entender la coevolución entre las galaxias y los SMBH. Presentamos WISE2MBH, un algoritmo eficiente que utiliza magnitudes catalogadas del Wide-field Infrared Survey Explorer (WISE) para estimar la masa estelar total (M_*) y escalarla a la masa del bulbo (M_{Bulge}) y M_{BH}, estimando el tipo morfológico (T_{Type}) y la fracción del bulbo (B/T) en el proceso. WISE2MBH utiliza relaciones de escala de la literatura o desarrolladas en este trabajo, proporcionando un enfoque simplificado para derivar estos parámetros. También distingue cuásares (QSOs) de galaxias y estima el T_{Type} de la galaxia utilizando colores de WISE con una relación entrenada con el 2MASS Redshift Survey. WISE2MBH funciona bien hasta $z \sim 0.5$ gracias a K-correcciones en magnitudes y colores. Después de una pequeña compensación empírica, las estimaciones de M_{BH} de WISE2MBH coinciden muy bien con las de una muestra seleccionada de galaxias locales con mediciones de M_{BH} o estimaciones confiables: se obtuvo un puntaje de Spearman de $\sim$0.8 y un RMSE de $\sim$0.63. Cuando se aplica a la muestra ETHER a $z \leq 0.5$, WISE2MBH proporciona alrededor de $\sim$2 millones de estimaciones de M_{BH} (78.5% nuevas) y alrededor de $\sim$109 mil límites superiores. La función de masa de agujeros negros (BHMF) local derivada está en buen acuerdo con las BHMF de la literatura existente. Proyectos demográficos de galaxias, incluida la selección de objetivos para el Telescopio del Horizonte de Eventos, pueden beneficiarse de WISE2MBH para obtener parámetros de galaxias y estimaciones de M_{BH} actualizados. El algoritmo WISE2MBH está disponible públicamente en GitHub.

Abstract

Supermassive Black Holes (SMBHs) are commonly found at the centers of massive galaxies. Estimating their masses (M_{BH}) is crucial for understanding galaxy-SMBH co-evolution. We present WISE2MBH, an efficient algorithm that use cataloged Wide-field Infrared Survey Explorer (WISE) magnitudes to estimate total stellar mass (M_*) and scale it to bulge mass (M_{Bulge}), and M_{BH}, estimating the morphological type (T_{Type}) and bulge fraction (B/T) in the process. WISE2MBH uses scaling relations from the literature or developed in this work, providing a streamlined approach to derive these parameters. It also distinguishes QSOs from galaxies and estimates the galaxy T_{Type} using WISE colors with a relation trained with the 2MASS Redshift Survey. WISE2MBH performs well up to $z \sim 0.5$ thanks to K-corrections in magnitude and colors. After a small empirical compensation, WISE2MBH M_{BH} estimates agree very well with those of a selected sample of local galaxies with M_{BH} measurements or reliable estimates: a Spearman score of $\sim$0.8 and a RMSE of $\sim$0.63 were obtained. When applied to the ETHER sample at $z \leq 0.5$, WISE2MBH provides $\sim$2 million M_{BH} estimates (78.5% new) and $\sim$109 thousand upper limits. The derived local black hole mass function (BHMF) is in good agreement with existing literature BHMFs. Galaxy demographic projects, including target selection for the Event Horizon Telescope, can benefit from WISE2MBH for up-to-date galaxy parameters and M_{BH} estimates. The WISE2MBH algorithm is publicly available on GitHub.

Contents

List of Tables

List of Figures

Chapter 1

Introduction

Supermassive black holes (SMBH) are characterized by having masses ($M_{\rm BH}$) ranging from $\sim 10^5$ to $10^{10} M_\odot$ and are believed to be located at the centers of all galaxies with a bulge, including the Milky Way (e.g., Ferrarese and Ford, 2005; Graham, 2016). The presence of SMBH is inferred from observations of stellar and gas motions in galactic nuclei (e.g., Genzel et al., 2010; Saglia et al., 2016), as well as strong nuclear X-ray to radio emission (e.g., Broderick et al., 2015; Liu et al., 2022). The Event Horizon Telescope (EHT) has provided the most direct evidence of the existence of SMBH (Event Horizon Telescope Collaboration et al., 2019, 2022). SMBH play a crucial role in shaping the evolution and structure of galaxies, as they can affect the surrounding stars and gas through 'feedback', and they are expected to co-evolve with their host galaxies (Kormendy and Ho, 2013).

Active galactic nuclei (AGN) are a manifestation of SMBH that are powered by a luminous accretion process at the centers of numerous galaxies. AGN emission can cover the entire electromagnetic spectrum (Padovani et al., 2017). At infrared (IR) wavelengths, the emission is primarily attributed to a toroidal arrangement of dust, which absorbs the radiation emitted by the central accretion disk and re-radiates it at IR (Netzer, 2015; Hickox and Alexander, 2018).

Quasars (QSO) are a type of extremely luminous AGN (with bolometric luminosity, $\log L_{\rm bol}$, in the range of 44 to 48 erg s^{-1}) that are powered by high accretion rates onto SMBH ($L_{\rm bol}/L_{\rm Edd} \sim 10^{-2.9}$ to $10^{1.8}$, Kong and Ho, 2018). Given these high accretion rates, QSOs are among the most luminous objects in the universe, making it difficult (though not completely impossible) to discriminate the morphology
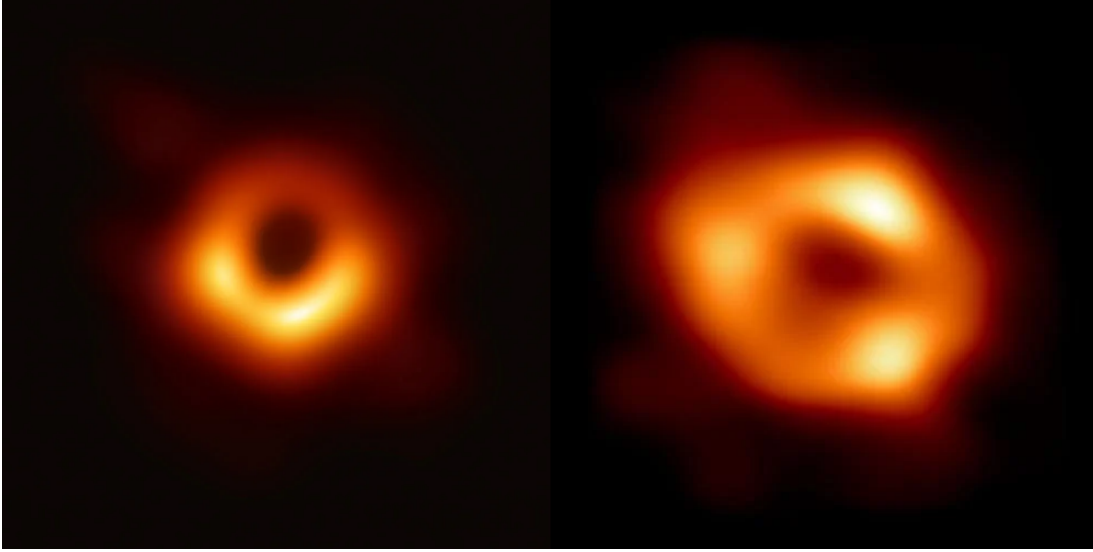
Figure 1.0.1: EHT images of M87* (left) and Sgr A* (right) from observations in the 2017 campaign. The images are the average of three different imaging methods after convolving each with a circular Gaussian kernel to give matched resolutions (Event Horizon Telescope Collaboration et al., 2019, 2022).

of their host galaxies at any redshift (z) (Dunlop et al., 2003). QSOs are among the earliest and most distant observable objects (e.g., $z \sim 7.64$, Wang et al., 2021), and are thought to be important probes of the early universe and the formation and growth of galaxies and their SMBHs (Inayoshi et al., 2020).

The Wide-field Infrared Survey Explorer (WISE, Wright et al., 2010) was a NASA IR−Wavelength astronomical space telescope that surveyed the entire sky in four IR bands, with central wavelengths at 3.4 μm, 4.6 μm, 12 μm, and 22 μm (W1, W2, W3 and W4, respectively). These bands can be used to study several features of a galaxy. The shorter wavelength bands (W1 and W2) predominantly capture emission from stars (e.g., Jarrett et al., 2011; Jarrett et al., 2012; Norris et al., 2014, see Fig. 1.0.3) and warm dust (e.g., Lyu et al., 2019; Noda et al., 2020; Li and Shen, 2023), providing insights into stellar populations in galaxies (e.g., Kettlety et al., 2018). The longer wavelength bands (W3 and W4) are sensitive to emission from cooler dust, revealing regions of colder dust associated with older stars (e.g., Singh et al., 2021; Li et al., 2023), allow estimation of star formation rates (SFRs, e.g. Lee et al., 2013; Cluver et al., 2017, see Fig. 1.0.4) and potentially highlighting the presence of AGN (e.g., Lyu and Rieke, 2022; Hviding et al., 2022). By analyzing the relative intensities and the spatial distribution of emission across these bands, it is possible to obtain the temperature, composition,
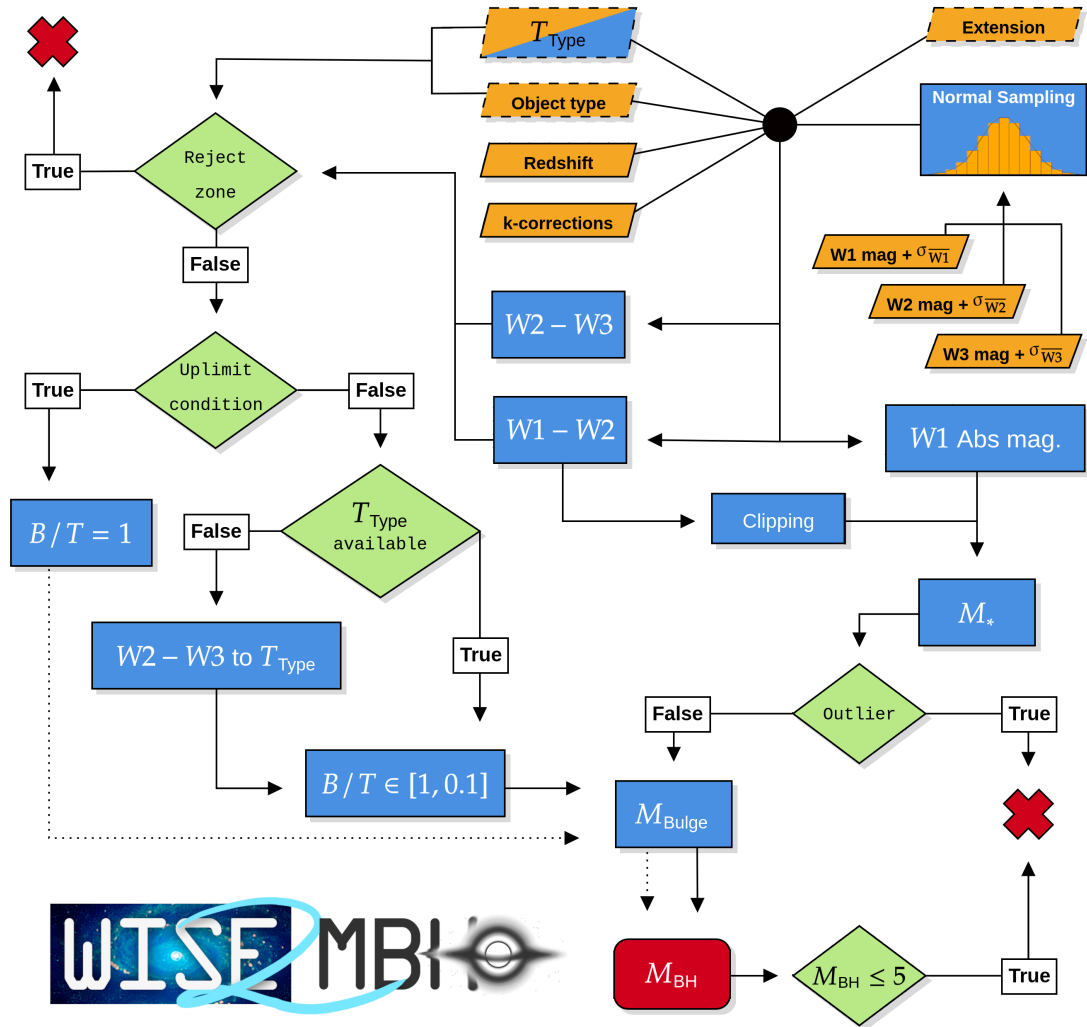
Figure 1.0.2: WISE2MBH: A simple algorithm that makes use of WISE cataloged data and a spectroscopic redshift to estimate the stellar mass, morphological type, bulge fraction, and M_{BH} of an extragalactic source. Solid (dotted) lines represent the main path to estimate a value (or upper limit), or to reject an object from the algorithm. Orange (blue) boxes show the input (derived) quantities; boxes with both colors can either be provided to or are estimated by the algorithm. Inputs in dashed boxes are optional. WISE magnitudes with their respective mean photometric errors ($\sigma_{\overline{WX}}$) are used to generate random normal samples of size 10^4 for a Monte Carlo approach to error propagation.

and distribution of a galaxy's dust and stars, thereby unraveling its evolutionary history and physical characteristics. All of this can be seen in Fig. 1.0.5.

One of the most relevant physical characteristics that can be estimated with WISE photometry is the total stellar mass of a galaxy (M_*). As stated by Cluver et al. (2014, hereafter C14) the W1 band is the most sensitive to the light emitted by the bulk of stellar population in galaxies (e.g., Meidt et al., 2012; Norris et al., 2014), thus allowing a determination of the mass attributed to the mass-dominant stellar population by using a mass-to-light (M/L) ratio (e.g., Kettlety et al., 2018). The M/L ratio can be constrained using the W1−W2 color. More recently, Jarrett et al. (2023, hereafter J23) have refined this process, developing a more stringent method to obtain stellar mass estimates from only the W1 band and assuming a global M/L ratio of ∼0.35 for all galaxies. Early-type galaxies have shown higher M/L (∼0.8) ratios, so that WISE-based estimates obtained using individual M/L ratios give results that are significantly different from the W1-only estimate. In instances of low uncertainty in WISE colors, the M/L ratio can be obtained through the use of the W1−W2 or W1−W3 color, and hence better correct for the range of M/L that is observed from early to late-types.

Another relevant property of galaxies is their morphology, how to classify them according to the latter, and how it evolves (e.g., Abraham et al., 1994; Abraham and van den Bergh, 2001; Willett et al., 2013). Many studies (e.g., Abraham et al., 1996; Whyte et al., 2002; Pahre et al., 2004) suggest that IR morphological classifications of galaxies can be superior to optical classifications, due to the physical properties that can be studied in the mid-IR, e.g., SFR and stellar populations, which evolve with the morphological type of the galaxy. Using WISE, distinct populations of early-type and late-type galaxies shown clearly different IR colors (e.g., Wright et al., 2010; Lee et al., 2017; Yao et al., 2020). Recently, Jarrett et al. (2019) showed a Hubble sequence-like evolution with the W2−W3 color for a sample of well-known nearby galaxies, where early-type galaxies showed redder (stellar-dominated) colors compared to late-type (ISM + stellar colors) galaxies, with a clear star formation sequence from the early-type to late-type. When combined with M_* estimates (e.g., C14, J23), the most massive galaxies were shown to be dominated by high fractions (≥ 0.8) of spheroid-like galaxies. These authors found the same behavior when exploring the bulge-to-total ratios (B/T): galaxies with $B/T \geq 0.9$ are dominantly at W2−W3 ≤ 1.5, which was set
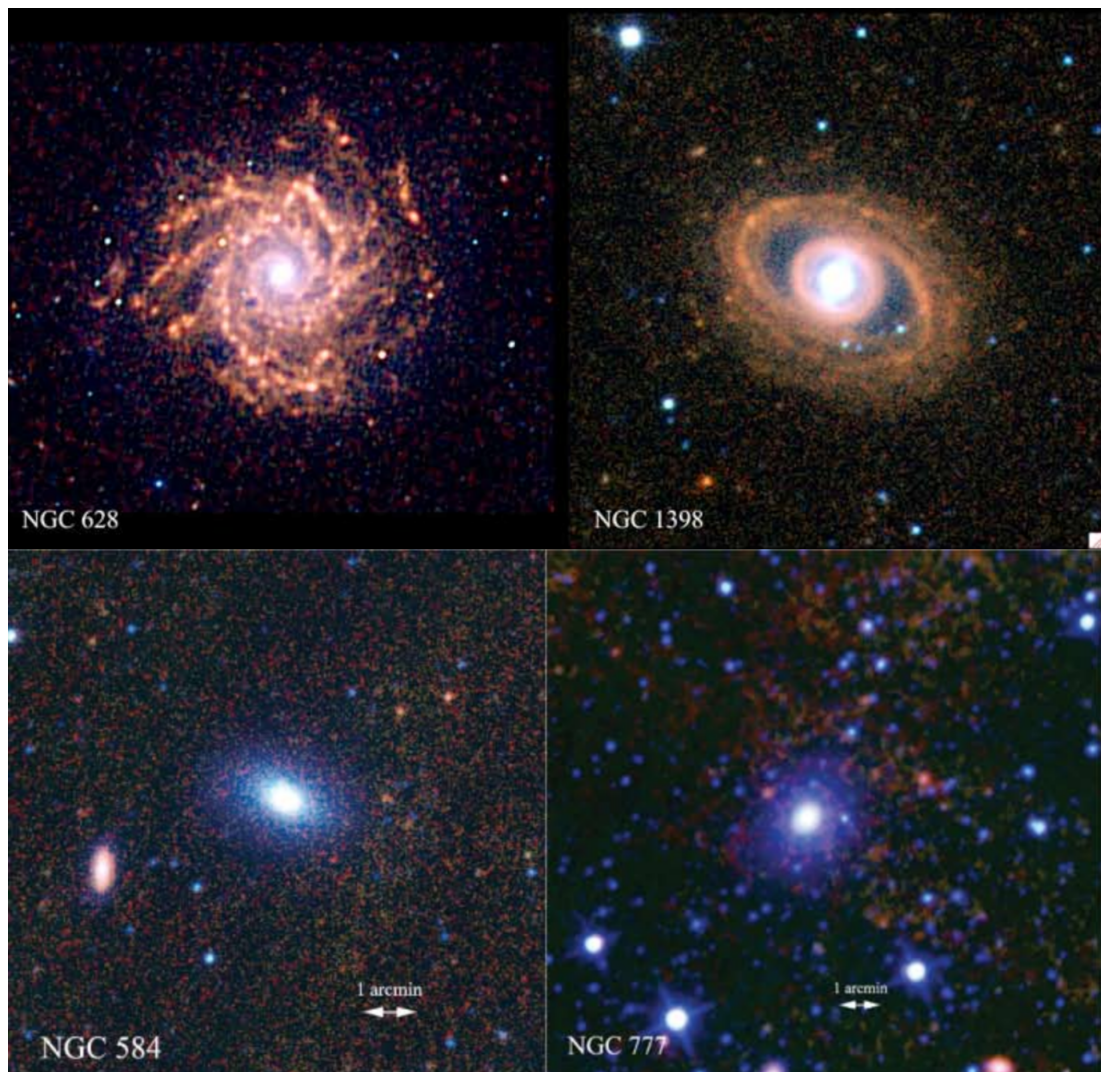
Figure 1.0.3: WISE view of late-type, spiral galaxies NGC 628 and NGC 1398 (top) and early-type, elliptical galaxies NGC 584 and NGC 777 (bottom). The colors correspond to WISE bands: 3.4μm (blue), 4.6μm (green), 12.0μm (orange), and 22μm (red). The different colors represent different stellar populations present in the galaxies. Extracted from Jarrett et al. (2012, Figs. 1 and 2)
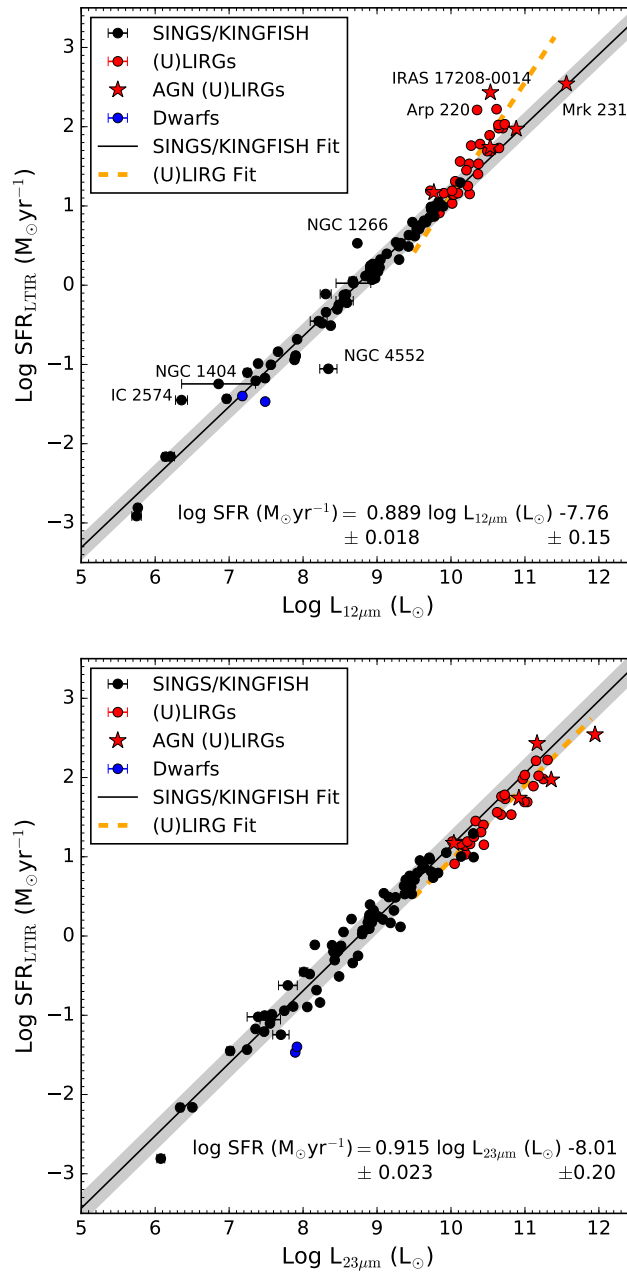
Figure 1.0.4: L_{TIR}-derived star formation rates (SFRs) are plotted against the WISE W3 12 μm (top) and W4 12 μm (bottom) luminosities and the best fit line to the SINGS/KINGFISH sample is shown (solid line); the 1σ scatter is indicated by the shaded region of 0.15 and 0.18 dex, respectively. For comparison, a sample of (U)LIRGs and dwarf galaxies is also shown. A fit to the (U)LIRG sample is shown by the dashed line in both cases. The trend suggests that L_{TIR} gives a higher SFR compared to the W3-derived value for high-luminosity sources and that W4 is marginally overestimating the SFR compared to L_{TIR} at high luminosity. Extracted from Cluver et al. (2017, Figs. 5 and 6)
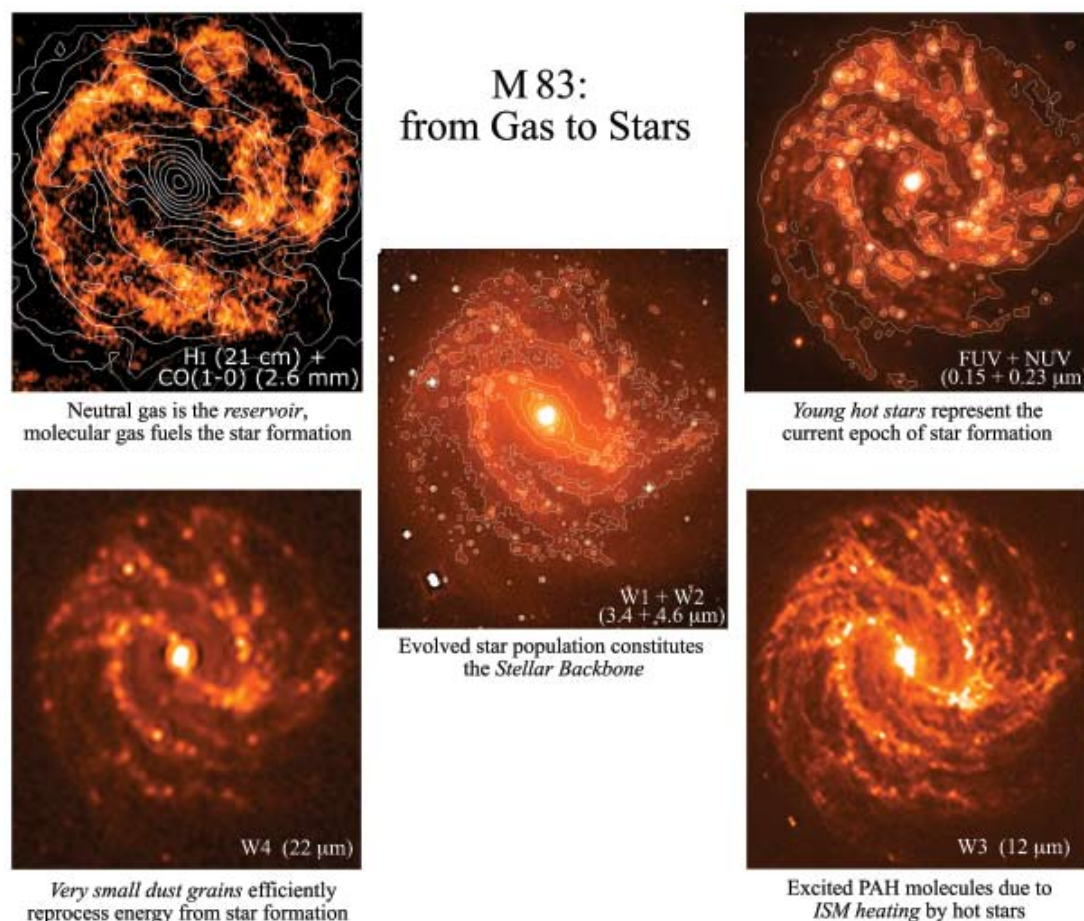
Figure 1.0.5: The many faces of M 83, highlighting the evolution from gas to stars. The 10 acmin panels show: the neutral (H I grayscale) and molecular hydrogen (CO contours) gas content, massive star formation as viewed by GALEX NUV (grayscale) and FUV (white contours), WISE view of 11.3 μm PAH emission (W3 band) and reprocessed starlight (W4 band) both associated with star formation, and the center panel shows the stellar distribution of the previous generations of star formation as viewed with the W1 (3.4 μm; grayscale) and W2 (4.6 μm; white contours) bands. Extracted from Jarrett et al. (2012, Fig. 14)

as the cutoff between spheroid galaxies and intermediate disks. Other studies have also shown that early-type and late-type galaxies showed distinct distributions of W2$-$W3 color (e.g., Sadler et al., 2014), specially in Cluver et al. (2020), the former being once again the most massive galaxies: in their sample with $\log M_* \geq 11.2$, the percentage of early-type galaxies reaches $\sim 80\%$.

Powerful AGN are characterized by their high IR luminosity, resulting in strong WISE detections. WISE can differentiate between those strong AGN and galaxies using WISE color-color criteria (e.g., Jarrett et al., 2011; Hviding et al., 2022). This differentiation is important as AGN play a crucial role in the evolution of galaxies: they have the capability to heat the surrounding gas and dust, suppress the formation of new stars, and ultimately quench star formation. Stern et al. (2012) proposed a simple W1$-$W2 cutoff to successfully identify AGN to a depth of W2 ~ 15. This cutoff was exploited, improved, and used for the creation of the WISE AGN catalog (Assef et al., 2018) and to derive new criteria to identify low luminosity AGN ($\log L_{\mathrm{bol}}$ in the range of 40 to 44 erg s^{-1}; Hviding et al., 2022).

Empirically, a strong correlation is observed between the M_{BH} and the bulge mass (M_{Bulge}) in elliptical galaxies, as well as in spiral galaxies with pseudo-bulges and classical bulges (e.g., Häring and Rix, 2004; Kormendy and Ho, 2013; Schutte et al., 2019) with previous theoretical approaches supporting this idea (e.g., Croton, 2006). Combining this with the observed evolution of B/T with the T_{Type} of a galaxy (e.g., Wang et al., 2019; Dimauro et al., 2022; Quilley and de Lapparent, 2022), it is possible to exploit the WISE data and scale from M_* to M_{Bulge} and finally to M_{BH}.

Combining all of the above, WISE photometry can be used to distinguish between different types of extragalactic objects, e.g. QSOs, ULIRGS, AGN, and galaxies, and to estimate the galaxy morphology using colors between the W1, W2, and W3 bands (e.g., Wright et al., 2010, C14, J23) and estimate M_{Bulge} and M_{BH}.

In this work, we introduce a new algorithm, WISE2MBH, which takes advantage of existing relationships derived from WISE data, the proportionality between the masses of the galaxy bulge and its SMBH, and new scaling relationships derived here. The WISE2MBH algorithm is capable of classifying regular galaxies, estimating their morphological type, and thus their bulge to total mass ratio, and estimating the mass of the SMBH. Additionally, it can identify QSOs from

WISE colors; due to the AGN contamination, the algorithm provides upper limit values for these. This algorithm and the resulting sample of SMBH masses are relevant to the study of individual sources using powerful instruments such as the EHT and the next-generation EHT (ngEHT, Johnson et al., 2023; Doeleman et al., 2023), as well as to studies of SMBH populations and evolution. In Sect. 2 we introduce the data used as input to the algorithm, in Sect. 3 we explain, in detail, the main steps of the algorithm. In Sect. 4 we present the main results and statistics of the WISE2MBH final sample generated by the algorithm, in Sect. 5 we briefly discuss the results, their relevance, main assumptions and limitations, and lastly in Sect. 6 we present our conclusions.

Throughout this work, we use Vega magnitudes and adopt the cosmological parameters of Planck Collaboration et al. (2020): $\Omega_{\rm m} = 0.31$, $\Omega_\Lambda = 0.69$, and $H_0 = 67.66$ km s^{-1}Mpc^{-1}.

Chapter 2

Data

2.1 ETHER sample

The Event Horizon and Environs sample (ETHER) aims to be the definitive sample and database from which to choose targets for the EHT and ngEHT. The database, its algorithms, and references for data sources, was first presented in Ramakrishnan et al. (2023, hereafter R23). ETHER has since been expanded by including the following literature and database samples: (a) all galaxies in the HyperLeda[1] (Makarov et al., 2014) database with recessional velocity (defined nonrelativistically, i.e., $z = v/c$) less than 100.000 km/s; (b) the Million Quasar catalog (Milliquas, Flesch, 2023); (c) the Veron-Cetty and Veron AGN catalog (Version 13, Véron-Cetty and Véron, 2010) with updates from (Flesch, 2013); (d) the 2M++ redshift survey (Lavaux and Hudson, 2011); (e) the ROMA BZCAT blazar catalog (5th Edition, Massaro et al., 2016); (f) the 2MRS sample (Huchra et al., 2012); and (g) the $\sim$ million galaxies with SDSS and WISE photometry in the catalog of Chang et al. (2015). Several other individual black hole masses and radio fluxes from the literature have also been incorporated. Full details on the updated ETHER sample will be published in Nagar et al. (in prep).

Given the above updates and after consolidating multiple entries from the same source, the ETHER sample currently contains 3.8 million extragalactic sources, of which 233 have M_{BH} measurements and $\sim$860,000 have M_{BH} estimates. Of the estimates, $\sim$331,000 are from the M-sigma relationship, $\sim$525,000 are from single-

---

[1]HyperLeda is available at: https://leda.univ-lyon1.fr/

epoch reverberation mapping estimations, ∼3,000 are from M-L$_{\text{bulge}}$ estimations, and ∼600 are from other 'fundamental-plane' type relationships (see R23 for details).

Astroqueries to the NASA Extragalactic Database (NED) and SIMBAD are used to incorporate and update positions, spectroscopic redshifts (thus luminosity and angular distances for objects at D ≥ 50 Mpc), object types, morphological types (T_{Type}), AGN classifications, and radio to X-ray fluxes. The object type comes directly from NED source classifications, which have shown great precision (≥ 80%) for nearby sources ($D \leq 11$ Mpc, Kuhn et al., 2022). The object types in ETHER, incorporated from NED, are as follows: 'Galaxies' cover regular galaxies over the range from elliptical to spiral galaxies, 'QSOs' denote galaxies with significant nuclear activity thus luminosity, 'Radio Sources' (RS) refer to sources detected in the radio regime, without any distinction between galaxies or QSOs. If a source lacks any NED classification, it is designated as an 'Unknown' object type. Through visual inspection using the Sloan Digital Sky Survey (SDSS), and the color-color criteria using WISE colors (see Section 3.2), we established that this NED source classification was sufficiently accurate for our needs.

Morphological types (T_{Type}) are available for a significant fraction of the sample (22.4% via NED and SIMBAD queries and from individual samples e.g., Huchra et al., 2012; Makarov et al., 2014). These are predominantly E (−6 to −4) and Sc (4–5), representing 37.3% and 23.8% of all sources with available morphology, respectively. The large fractions in these two T_{Type} bins is primarily due to the binary classification of morphological type in some ingested samples (e.g., Dobrycheva, 2013). When available, this T_{Type} is used as an input to the algorithm; when not available, the T_{Type} is estimated from the W2−W3 color (see Section 3.3).

All ETHER sources at $z \leq 0.5$ form the parent sample for this work.

2.2   WISE catalogs

In this work, we use both the AllWISE catalog (Cutri et al., 2021) and the WISE Extended Source Catalog (WXSC, Jarrett et al., 2019). The latter includes mid-infrared photometry and measured global properties of the 100 largest (in angular size) galaxies in WISE. The WISE mission, funded by NASA as a Medium-Class

Explorer mission, features a space-based infrared telescope with megapixel cameras cooled by a two-stage solid hydrogen cryostat. This telescope conducted an all-sky survey which simultaneously captured images in four broad spectral bands: W1, W2, W3, and W4, centered on 3.4, 4.6, 12, and 22 μm with an angular resolution of 6.1″, 6.4″, 6.5″and 12.0″, and achieving sensitivities of 0.08, 0.11, 1 and 6 mJy, respectively.

2.2.1   AllWISE catalog

The AllWISE catalog, which combines data from the WISE cryogenic and NEOWISE (Mainzer et al., 2011) catalogs, contains almost 750 million sources, including galaxies, stars, brown dwarfs, and asteroids, making it one of the most comprehensive IR catalogs ever created. This catalog provides photometric quality flags (`qph`) for a given detection for all sources, making it the best option to extract data for our purposes; we accepted only sources with quality A, B, C or U in the first three bands, which translates to detections with signal-to-noise ratios (S/N) in the ranges of S/N $\geq$ 10, 10 > S/N $\geq$ 3, 3 > S/N $\geq$ 2 and S/N < 2, respectively, with the last flag considered an upper limit with 95% confidence. Extension flags (`ex`) are also provided in this catalog, allowing easy differentiation between extended and point sources. This flag is directly related to the 2MASS Extended Source Catalog (XSC, Jarrett et al., 2000), ranging from 5 for completely extended sources to 0 for point sources. This flag contributes to the overall quality flag of our estimates and thus allows the selection of high-quality sub-samples (e.g., using only extended sources) from our overall sample. In this work, sources with `ex` equal to 4 or 5 are considered extended, while those with values 0 to 3 are considered point sources. Thus, in our definition, a WISE extended source is one whose position falls within 5″of the central position of a 2MASS XSC source, and a WISE point source is one that is not associated with a 2MASS XSC source, or is offset by $\geq$ 5″ from the central position of a 2MASS XSC source even if it falls within its isophotes.

2.2.2   WISE Extended Source Catalog (WXSC)

The AllWISE photometric catalogs are optimized for the characterization of point-sources[2]. For highly extended sources, source detection and extraction may not

---

[2]AllWISE Explanatory Supplement: Cautionary Notes

include all the extended components of the galaxy in a single source, thus leading to an underestimation of true brightness.

The WXSC (Jarrett et al., 2019) provides full source characterization in all four WISE bands for the 100 largest galaxies (in angular extent) in the sky. WXSC uses new mosaics with native resolution allowing for precise measurements of both the target galaxy and its local environment. These mosaics are further resampled with 1" pixels, greatly enhancing analysis accuracy. When a galaxy is present in WXSC, we use these magnitudes instead of those from AllWISE.

2.3   WISE2MBH parent sample

All sources in the ETHER sample at $z \leq 0.5$ were cross-matched with the AllWISE and WXSC catalogs with a cone search radius of $3''$, preferring WXSC matches over AllWISE to consider better photometric values. After deleting duplicates, 91.2% of the ETHER targets matched the two WISE catalogs.

Given that the AllWISE catalog has a high density of sources (on average ~ 5 sources per arcmin^2) and the ETHER sample is also relatively large ($\sim$3.8 million galaxies, with a bias towards northern galaxies), it is important to address the probability of false matches in a $3''$ radius. We generate random samples of 10^5 right ascension and declination coordinate pairs, divide them into subsamples in (l between ± 15) and outside the Galactic plane, and test for random matches and possible contamination of W1 magnitudes due to confusion. When matching these random samples to the AllWISE catalog, we find a 4% ($\sim 5\%$) chance of matching a random position source out of the plane (in the plane) of the galaxy with an AllWISE source. The distributions of W1 magnitudes for real ETHER galaxies matched to WISE are consistently brighter than the magnitudes obtained in the random matches. The W1 magnitude distributions of both AllWISE sources matched to the random position catalogs ($\mu = 17$ mag) and to the ETHER galaxies ($\mu = 14$ mag), are significantly fainter than those of Galactic AGB stars in AllWISE ($\mu = 8$ mag; Suh, 2021).

The differentiation between early-type galaxies and stars in AllWISE catalogs, in the absence of redshifts, remains a topic of ongoing discussion. Machine learning classification techniques have exhibited significant achievements in this area (e.g., Kurcz et al., 2016). In our case we do not expect to be affected by this problem

for two reasons (a) ETHER has both precise (typically sub-arcsec accuracy) coordinates and includes only known extragalactic objects (when redshifts exist these are spectroscopic); (b) the low probability of random matches as explored in the previous paragraph.

A summary of the resulting WISE2MBH parent sample is given in Table 2.3.1 where we list the total number of sources of each object type (N), and the total number of sources of the WISE2MBH parent sample and ETHER. The other columns represent a percentage of completeness. The distribution of sources in redshift by object type and `ex` can be seen in Fig. 2.3.1.

Table 2.3.1: Statistics of the WISE2MBH parent sample, composed of sources from the ETHER sample crossmatched with the AllWISE catalog.

Object type	N	z	M_{BH}	ex	W1	W2	W3
Galaxy	601658	99.80	60.39	30.95 / 69.05	99.98 / <0.01	99.49 / 0.51	69.98 / 29.97
QSO	16200	99.27	55.98	0.81 / 99.18	99.96 / <0.01	99.87 / 0.13	95.41 / 4.54
RS	9360	71.83	3.31	0.33 / 99.66	99.83 / 0.13	99.48 / 0.52	67.13 / 32.83
Unknown	1468364	98.85	59.40	5.95 / 94.05	99.81 / 0.15	99.40 / 0.60	48.91 / 51.05
Total	2095586	99.01	59.41	13.06 / 86.94	99.86 / 0.12	99.43 / 0.57	55.40 / 44.56
Total ETHER	2231221	-.-	-.-	-.- / -.-	-.- / -.-	-.- / -.-	-.- / -.-

Notes: From left to right, we list the number of sources, and the percentages of sources with a spectroscopic redshift, existing M_{BH} estimate, extension flag (ex) equal to 5-4/3-2-1-0 (completely extended/point-like) and photometric quality flags (qph) in the W1, W2, and W3 WISE bands with qph equal to A-B-C/U.
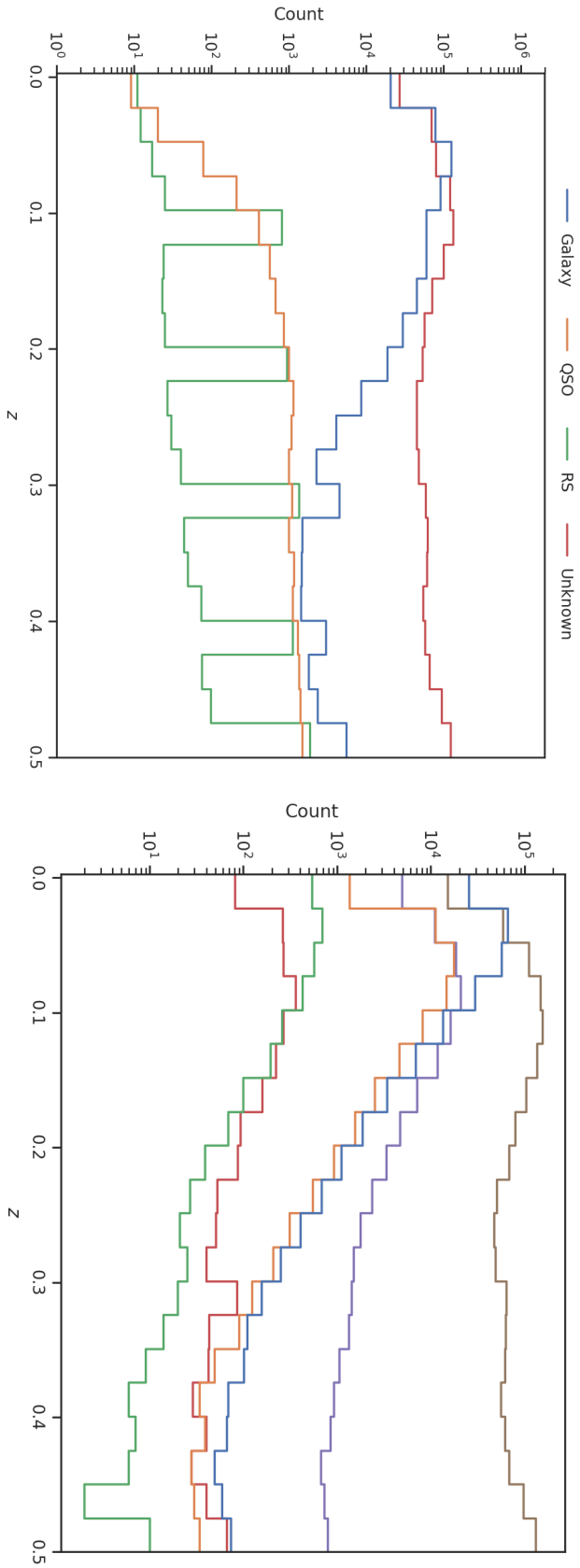
Figure 2.3.1: Redshift distribution of the sample used as input to the algorithm. Left: Separated by source extension. Galaxies and unknown type sources dominate by a few orders of magnitude over other object types, while extended (5-4) and point-like (3-0) sources do not show a clear dominance. Right: Separated by object type.

Chapter 3

Methodology

3.1   K-corrections for WISE magnitudes and colors

Jarrett et al. (2023) used spectral energy distribution (SED) templates of galaxies with different morphological types (e.g., Brown et al., 2014) to calculate K-corrections for the W1 magnitude, and the W1−W2 and W2−W3 colors, for each available T_{Type} over the range $z = 0 - 3$. These K-correction lookup tables were shown in Figs. 9 and 10 of J23 (see Fig. 3.1.1), but only for $z \leq 0.5$.

Due to the uncertain morphological type and AGN contamination of objects classified as 'RS', and given the tendency of QSOs to continue to reside in the AGN/QSO area of a WISE color-color diagram independent of redshift (e.g., Mateos et al., 2012; Stern et al., 2012), we do not apply K-corrections to the RS and QSO object types.

Of the remaining objects (i.e., galaxies or unknown) only those which reside in the 'Estimate zone' of Fig. 3.1.3 (see Sect. 3.2) are K-corrected. This selection is made to avoid a false K-correction for AGN-contaminated sources.

Our algorithm applies the J23 K-corrections for three T_{Type} ranges; ellipticals (−5 to −3), lenticulars (from −3 to 0) and spirals (from 0 to 8). The existing T_{Type} of an individual object, if available, is used to select between these three lookup tables. If no T_{Type} is available, the lookup table to be used is decided as follows. Mateos et al. (2012, see their Fig. 5. In this thesis, Fig. 3.1.2) use
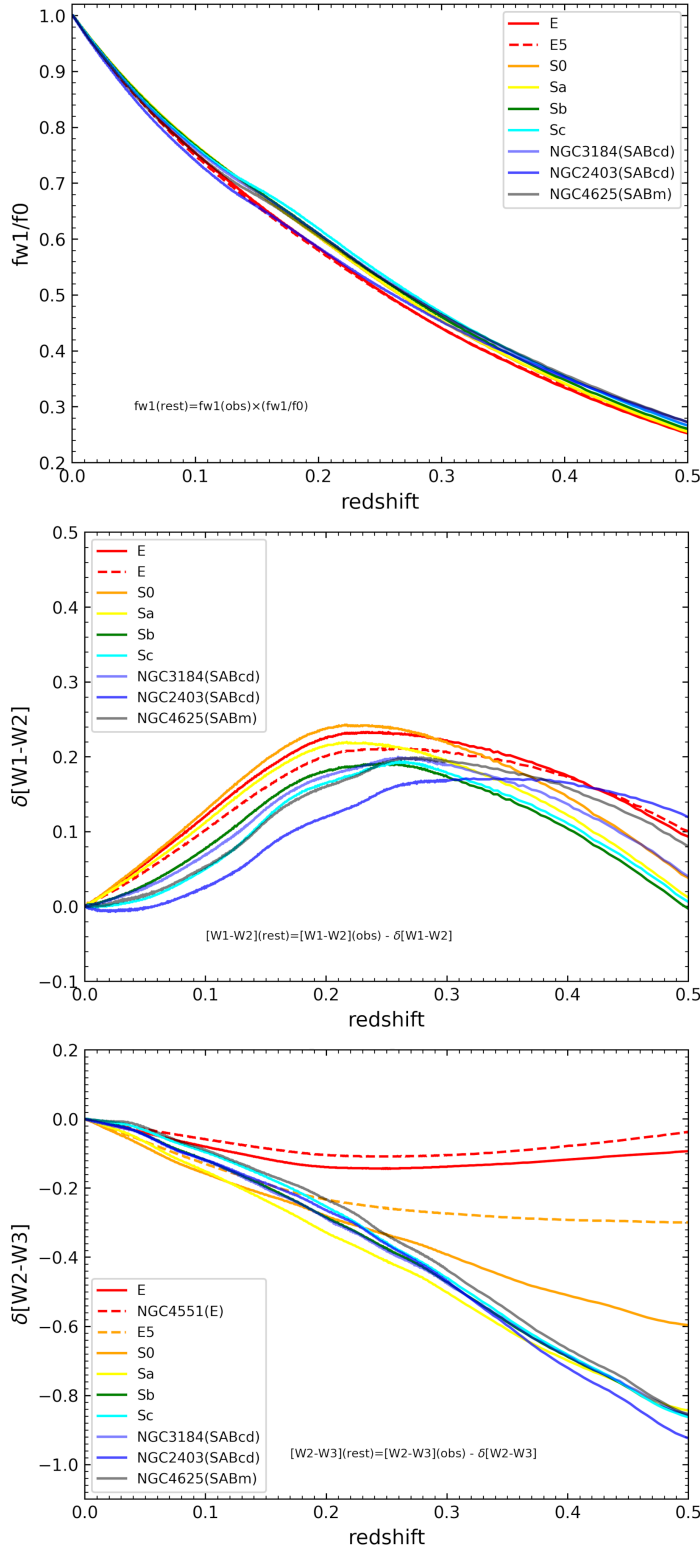
Figure 3.1.1: Rest-frame corrections for WISE W1 3.4 μm (top) W1$-$W2 (middle) and W2$-$W3 (bottom) based on SED composite templates that cover the galaxy types from early-to-late (bulge-to-disk dominated). The W1 scaling correction can be approximated by an exponential function. Extracted from Jarrett et al. (2023, Figs. 9 and 10)
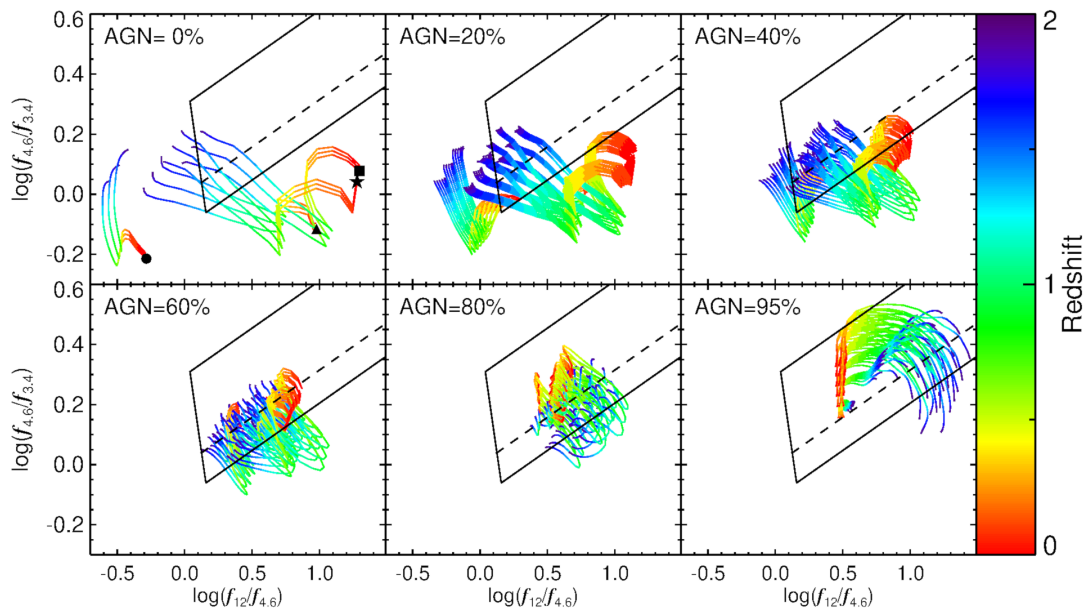
Figure 3.1.2: Predicted $z = 0 - 2$ WISE colours of AGN/galaxy composite SEDs for our three-band AGN wedge. The AGN fraction is defined between 1 and 10 μm. The star-forming templates represent the ULIRG IRAS 22491 (square, Polletta et al., 2008), the starburst M82 (star, Polletta et al., 2008), a normal star-forming spiral galaxy (triangle, Dale and Helou, 2002), and an elliptical galaxy (circle, Polletta et al., 2008). Large symbols mark each family of purely star-forming templates at $z = 0$. The AGN template is the QSO1 template of Polletta et al. (2008). Extracted from Mateos et al. (2012, Fig. 5)

galaxy templates of various morphological types, and with varying amounts of AGN contamination, to derive the redshift evolution of a galaxy's WISE colors over the redshift range 0 and 2. Although the WISE colors vary with redshift (especially for late-type galaxies), they find that, in the absence of a large AGN contamination, WISE colors can distinguish between early-type and late-type galaxies over this full redshift range.

We thus define the following cutoff in the observed W2−W3 color to distinguish between elliptical and spiral galaxies (without AGN contamination) up to $z \sim 1.5$,

$$\mathrm{W2{-}W3_{Limit}} = -2.5 \left(\log \left(\frac{F_{\mathrm{W3}}}{F_{\mathrm{W2}}} \right) - \log \left(\frac{f_{\mathrm{W3}}}{f_{\mathrm{W2}}} \right) \right) \qquad (3.1.1)$$

where F_0 and f_0 are the zero magnitude flux density and observed flux density in the respective band, respectively. We set the logarithmic ratio of observed flux densities in Eq. 3.1.1 to -0.1, since Fig. 5 of Mateos et al. (2012) shows that this

value clearly separates elliptical and spiral galaxies over their full redshift range. This translates to a cutoff value of $W2-W3_{Limit} \sim 1.58$ to distinguish elliptical and spiral galaxies (values larger than this imply a spiral galaxy). Note that this cutoff is similar to the values previously derived by Jarrett et al. (2019). The Lenticular lookup table is not used in this case, since lenticulars and spirals are not easily distinguishable in WISE color-color diagrams (see e.g., Sect. 3.3).

These K-correction look up tables have been shown to be reliable for galaxies at $z \leq 0.5$ (e.g., Jarrett et al., 2023; Karademir et al., 2023).

3.2 Distinguishing Galaxies and AGN/QSOs using WISE

If an object type is not already available (which is the case for 76% of the parent sample; Sect. 2), the algorithm uses WISE color-color criteria to distinguish galaxies from strong AGN/QSOs, and to determine whether the derived values are estimates or upper limits (due to contamination from an AGN).

The algorithm is first tested on targets with an available object type. As mentioned in Sect. 3.1, we use cutoffs in the observed $W1-W2$ and $W2-W3$ colors to identify objects that will be K-corrected. The same cutoffs are now applied to the K-corrected colors to determine if this target falls within the estimate, upper limit or rejection zones in the WISE color-color plot shown in Fig. 3.1.3. These objects then, respectively, follow the estimate, upper limit or reject paths of the algorithm shown in Fig. 1.0.2 and described in Sect. 3.5.

Objects with object type QSO and RS are likely to have significant AGN contamination in their W1 mag, which will likely increase their M_* estimates, independent of their extension in WISE. For these objects, we therefore immediately consider the WISE-derived M_* values as upperlimits. The horizontal dashed line in Fig. 3.1.3, which separates the upper limit zone from the estimate zone, is a combination of the widely used $W1-W2 = 0.8$ limit to separate AGN/QSOs from galaxies (e.g., Stern et al., 2012; Michalik and Lindegren, 2016; Guo et al., 2018), together with a wedge region between $W2-W3 \sim 2.2 - 4.4$ motivated by previously defined AGN/QSOs regionsJarrett et al. (2011); Hviding et al. (2022). We slightly modified the wedge region defined by Jarrett et al. (2011)
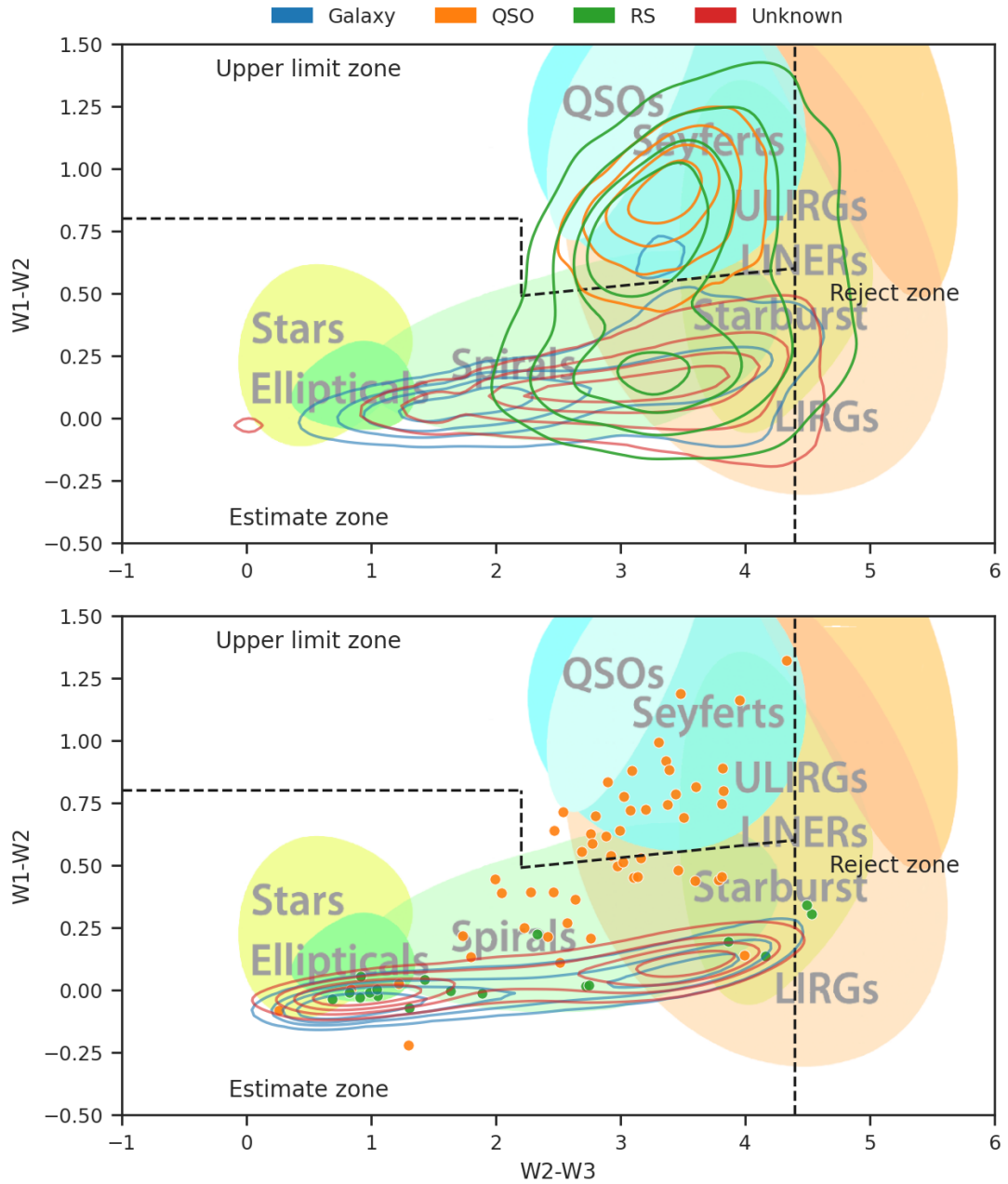
Figure 3.1.3: WISE color-color plot showing the location of our sample objects and defining the areas over which the stellar mass estimation is an upperlimit (Upper limit zone), is not estimated by the algorithm (Reject zone), or estimated by the algorithm (Estimate zone); these zones are separated by black dashed lines. Note that QSO and RS object types are considered as stellar mass upper limits independent if whether they fall in the "Upper limit" or "Estimate" zone. For clarity we plot separately the point sources (top panel) and extended sources (bottom panel; see Sect. 2). The background filled colors and labels are from Fig. 12 of Wright et al. (2010), and are shown for reference. Contours, in colors following the color legend on top of the figure, show the number density of object types in our sample. In the bottom panel, object types QSO and RS are shown as colored points (instead of contours) in the corresponding color.

by optimizing the WISE color classification of known QSOs in our sample. The wedge region we chose is defined as follows

$$2.2 < W2-W3 < 4.4 \wedge W1-W2 > (0.05[W2-W3] + 0.38). \qquad (3.2.1)$$

which now fully extends to the blue-side of the diagram thanks to the $W1-W2 = 0.8$ cutoff. With this overall cut, almost 95% of the known QSOs in our sample are classified as QSOs by this color criterion.

The vertical limit at $W2-W3 = 4.4$ in Fig. 3.1.3, which separates the Reject zone from the other two zones, is also set by us. At $W2-W3 \geq 4.4$, the WISE-derived T_{Type} (see Sect. 3.3) is 8 or larger, and the estimated B/T would be very low (Sect. 3.4). While this would be correct for, e.g., irregular galaxies, it is incorrect for, e.g., extremely dusty, hybrid-starburst-AGN galaxies (Tsai et al., 2015) or newborn AGN (Arevalo et al. in prep)[1].

The WISE color-color distributions of different object types (including unknown types) in our sample are shown in the top (WISE point sources) and bottom (WISE extended sources) panels of Fig. 3.1.3.

The top panel of Fig. 3.1.3 shows that most QSOs and RS reside at high $W1-W2$ colors, in an area populated by a variety of AGN and also ULIRGs, making it a challenge to correctly identify them using only WISE data. On the other hand, known galaxies, even if point-like for WISE, show clear overdensities in the region where elliptical and spiral galaxies are expected to reside. In our sample, the only object types that enter the reject zone are RS; these are likely RS in LINER galaxies.

For the bottom panel of Fig. 3.1.3 (WISE extended sources), all ($\sim 99\%$) known galaxies lie in the Estimate zone, at WISE colors expected of elliptical and spiral galaxies, and away from the regions of starbursts, LINERs and (U)LIRGs. Only a few QSOs and RS are present in this figure: the QSOs (orange dots) do not clump in the expected QSO area, but are instead distributed over a large range of colors, overlapping with regions of galaxies, ULIRGs, and Seyferts; RS (green dots) are predominantly situated in the galaxies area, with a few in the LINER

---

[1]P. Arevalo showed in XVII LARIM on December 2023, the evolution in $W1-W2$ color for a typical star-forming non-active galaxy to AGN-like in a time-span of years, together with spectroscopic data from SDSS and SOAR that support the idea of new AGN activity in ZTF20aaglfpy, which was also classified as a type I AGN by the ALeRCE light curve classifier.

area. This behavior for both QSOs and RS to not reside in the expected wedge region is not strange, since these extended sources are most likely weak AGNs, where the emission is not enough to change the color to be classified as a QSO, as was shown in Mateos et al. (2012), where different percentages of AGN activity were tested, showing that only strong AGNs (80% fraction) up to $z = 2$ reside in an area similar to the one defined here or in previous studies.

The bulk of sources with unknown type (76% of the parent sample; red contours in both panels) sit in the Estimate zone, mostly following the expected distribution of galaxies. The clear separations seen for known object types give us confidence that the classification of these unknown types as galaxies is reliable.

3.3   Using W2-W3 color to estimate T-Type

While T_{Type} is available for some ($\sim 20\%$) sources in the WISE2MBH parent sample, a reliable estimation of this is required for most of the sample. To obtain these T_{Type}, we exploit the fact that the W2$-$W3 color shows clearly separated regions where elliptical and spiral galaxies reside (e.g., Wright et al., 2010; Jarrett et al., 2019; Cluver et al., 2020). Although these regions partially overlap with other classifications based on star formation activity, the trend is sufficient to estimate the morphology of the galaxy, i.e., T_{Type}.

Our conversion of W2$-$W3 color to T_{Type} is trained using $\sim$18,000 galaxies from the 2MRS catalog (Huchra et al., 2012) for which manually classified T_{Type} are available. The median W2$-$W3 colors of 2MRS galaxies in each T_{Type} bin between -5 and 8 (open and filled black circles in the main panel of Fig. 3.3.1) show a clear S-shape curve. The number of galaxies in each T_{Type} bin is shown in the right histogram of Fig. 3.3.1. Given the S-shape, i.e., the lack of differentiation in the x-axis for the three to four bins at each extreme end of W2-W3 colors, a sufficiently large number of objects per bin is required for a clear result. We therefore use statistical power analysis to define the required sample size threshold; details of this analysis can be found in Appendix A2. For this power analysis, a power $P = 0.8$ and a significance threshold $\alpha = 0.05$ were assigned. The effect size (E_s) was calculated for each set of two consecutive bins in W2$-$W3 (in order of increasing T_{Type}), and the resulting median E_s (0.15) implies that the sample size per bin must be $N \gtrsim 700$. Therefore, all bins with a sample size greater than
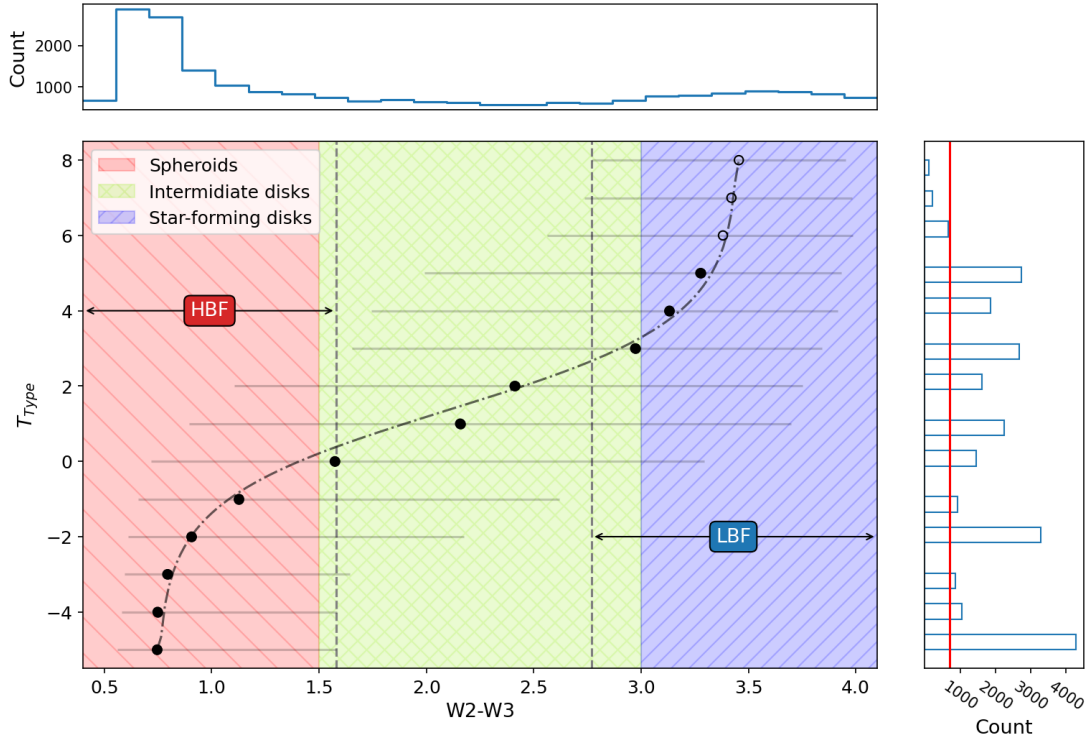
Figure 3.3.1: T_{Type} as a function of W2$-$W3 color for galaxies in the 2MRS sample. For each T_{Type} bin we plot the median value (black circle) and one sigma dispersion (horizontal bar) of the W2$-$W3 colors of galaxies in the bin. Distributions of W2$-$W3 and T_{Type} are shown in the panels at the top and right of the figure, respectively. The red line in the right panel marks the threshold number of galaxies in a bin in order for that bin's median to be used for the fit (filled black circles in the main panel). The black dot-dashed line shows the best fit logit function to the filled black circles: this is used for the W2$-$W3 to T_{Type} conversion when T_{Type} is previously unknown. The estimated T_{Type} is limited to the range -5 and 8; when a galaxy's W2-W3 color lies beyond the range of the logit function shown, the T_{Type} is clipped at these values. The colored areas distinguishing morphologies listed in the inset are from Jarrett et al. (2019). Given the similarity of the color dispersions in the three bins at each extreme end of the x-axis, we define two vertical dashed lines which delineate galaxies we refer to as high bulge fractions (HBF; bulge fractions between 0.4 and 1) and low bulge fractions (LBF; bulge fractions between 0.1 and 0.3).

this N were accepted (filled black circles in Fig. 3.3.1).

A logit function was fit to these accepted median values, providing us with our
$W2-W3$ to T_{Type} conversion. Since the logit function's domain goes from 0 to 1,
the $W2-W3$ color is shifted and normalized ($W2-W3_{\mathrm{SN}}$) before fitting:

$$W2-W3_{\mathrm{SN}} = \frac{W2-W3 - 0.75}{2.71}$$
$$T_{\mathrm{Type}} = (1.21 \pm 0.01)\,\mathrm{logit}\,(W2-W3_{\mathrm{SN}}) + (1.36 \pm 0.02) \tag{3.3.1}$$

this logit function is shown as a dashed-dotted line in Fig. 3.3.1. Despite leaving
out three late-type T_{Type} bins from the fit ($T_{\mathrm{Type}} = 6$, 7 and 8), the logit function
fits almost perfectly to all medians.

The morphological limits of Fig. 10 of Jarrett et al. (2019) are presented for
comparison as colored regions in the figure. While the overall fit is S-shaped, we
find two clearly separated regions in the graph: the high bulge fraction (HBF)
region, which is delimited by the 84th percentile values of the bins centered on
$T_{\mathrm{Type}} = -5$ to -3, and the low bulge fraction (LBF) region, which is delimited
by the 16th percentile values of the bins centered on $T_{\mathrm{Type}} = 7$ and 8. Our HBF
region limit ($W2-W3 = 1.58$; vertical dashed line in the figure) is similar to
the cutoff used by Jarrett et al. (2019) to distinguish between spheroids and
intermediate disks (the division between pink and green regions in the figure),
and also similar to the value of $W2-W3_{\mathrm{Limit}}$ which we use to classify galaxies
with unknown morphological type into elliptical and spiral galaxies in order to
select the K-correction lookup table to be used (see Eq. 3.1.1 and Sect. 3.1).

The logit function in Eq. 3.3.1 is used whenever a source does not have an
available T_{Type} or if the available T_{Type} comes from a binary classification (e.g.,
Dobrycheva, 2013). The WISE2MBH algorithm uses T_{Type} in the range -5 to
8. Available T_{Type} values outside this range are clipped to the closest limit value,
in case these really define a morphology, e.g., -9 is often used to define a QSO
(ZCAT convention), so those values are not clipped. If a measured $W2-W3$ color
is outside the range of the logit function presented here, the estimated T_{Type} is also
clipped to the closest limit value T_{Type}. This is most relevant for elliptical galaxies,
whose $W2-W3$ colors are often less than 0.7, which the algorithm converts to
$T_{\mathrm{Type}} = -5$.

This T_{Type} estimator is meant to be an auxiliary function of the algorithm, preferring external values, but also providing a way to estimate them using only WISE data. The overlap regions make the classifications at extreme T_{Types} very uncertain at the moment of distinguishing between consecutive T_{Types}, but the distinction between bulge-dominated and disk-dominated galaxies is clear.

3.4 Bulge-to-Total ratio from T-Type

The morphological type of a galaxy within the Hubble sequence has been shown to be a good proxy of B/T. This inverse behavior (recently discussed in Quilley and de Lapparent, 2022, 2023) shows that early-type galaxies tend to be almost pure bulges ($B/T \sim 1$), while very late-type galaxies and irregulars tend to have small to null bulge fractions ($B/T \sim 0.01$). This inverse behavior also supports the posited scenarios of galaxy bulge growth via mergers: late-type galaxies merge consecutively until lenticular, elliptical, and finally, the brightest cluster galaxies (BCGs) are formed (Edwards et al., 2020), leading not only to the formation of the most massive galaxies (Bluck et al., 2014), but also to the most massive SMBHs (Mezcua et al., 2018).

By nature, elliptical galaxies are expected to have quenched their star formation, leading to a decrease in their SFR and specific SFR (sSFR), despite environmental effects (e.g., Casado et al., 2015). Recently, Ge et al. (2018) showed that galaxies with lower sSFR tend to be more massive and have higher B/T (≥ 0.7) compared to galaxies with higher sSFR, and also found a trend with galaxy age where the oldest galaxies have higher B/T. Morell et al. (2020) showed similar results, showing that their passive galaxy sample (made up of 70% ellipticals and 15% lenticulars) is the one with higher B/T (~ 0.7).

Massive elliptical galaxies are the most relevant sources for future EHT observations, and while varying their estimated B/T between 0.8–1 does not considerably affect the final M_{Bulge} estimate, a misclassification of T_{Type} could result in incorrect use of a spiral-like B/T (≤ 0.2), leading to an underestimate M_{Bulge}, thus M_{BH} (Bluck et al., 2014). Despite many references pointing to a $B/T \leq 0.8$ for early-type galaxies (e.g., Ge et al., 2018; Morell et al., 2020), we will impose a limit of $B/T = 1$ for $T_{\text{Type}} = -5$ (e.g., Caramete and Biermann, 2010; Quilley and de Lapparent, 2023), with an exponential decrease with T_{Type}
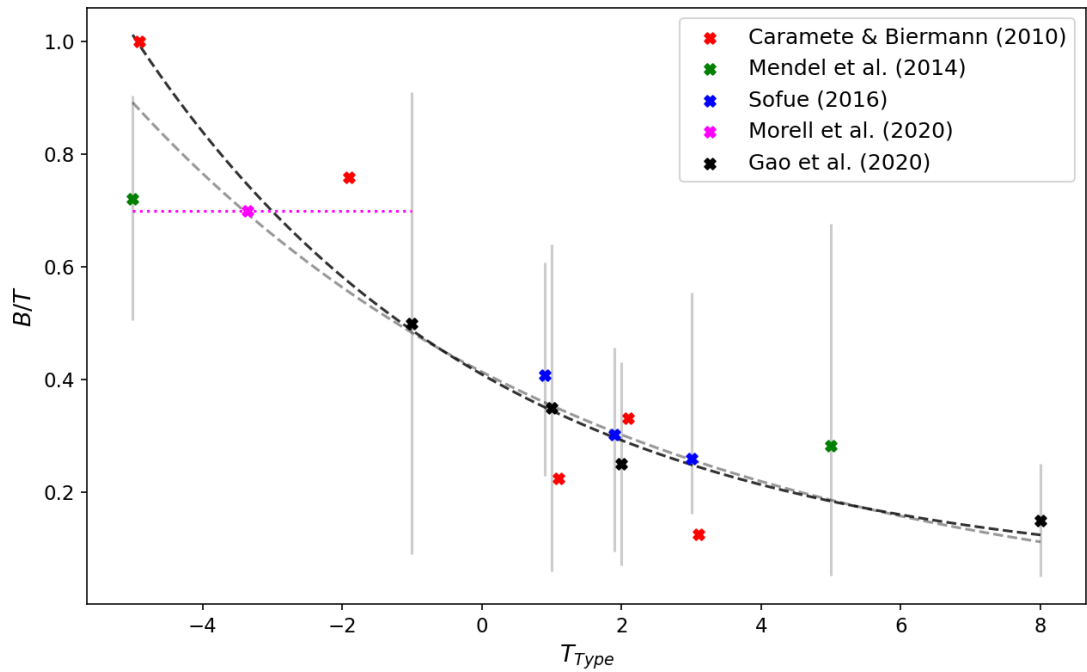
Figure 3.4.1: Distributions of the bulge-to-total (B/T) mass ratio as a function of T_{Type} for different literature samples. A decreasing exponential is fitted to the data points: the gray dashed curve is the original fit and the black dashed curve is the fit when one fixes $B/T = 1$ for $T_{\text{Type}} = -5$. For clarity, small shifts on the x-axis are used to avoid overlapping symbols and error bars. Data points and the horizontal pink dashed line are from Caramete and Biermann (2010); Mendel et al. (2014); Sofue (2016); Morell et al. (2020); Gao et al. (2020) following the colors listed in the inset.

as shown in Fig. 3.4.1. We note that Caramete and Biermann (2010) derived correction factors to convert near-IR luminosities to M_{BH} for galaxies of a variety of T_{Type} in the nearby universe ($z \leq 0.025$) with similar impositions for elliptical galaxies; these conversion factors are analogous to our B/T ratios.

We calibrate the B/T ratio as a function of T_{Type} using several samples from the literature. Mendel et al. (2014) provide total, bulge, and disk masses, for a large sample of SDSS galaxies. Their values, combined with T_{Type} from ETHER, give us distributions of B/T over a wide range of T_{Type}, although only -5 and 5 have enough statistics to be considered robust. The ETHER T_{Type} unfortunately comes primarily from the binary classification of Dobrycheva (2013), so we expect that the relationship between T_{Type} and B/T is biased, i.e., underestimated for ellipticals and overestimated for spirals. Sofue (2016) provide both bulge and disk masses for a small sample of nearby galaxies ($z \leq 0.03$) for which we obtained T_{Type} from NED. Morell et al. (2020) provide an average value of B/T for a sample of passive galaxies, which are composed of specified fractions of ellipticals, lenticulars and spirals, mostly dominated by the first two. The T_{Type} value that we used in this case is weighted by these fractions. From Gao et al. (2020) we take values of B/T only for T_{Type} equal to -1, 1 and 2 (S0, Sa and Sab) and consider T_{Type} equal to 8 (Sdm) as a limit to secure reasonable bulge masses even for very late-type galaxies.

A plot of T_{Type} as a function of B/T for all these samples is shown in Fig. 3.4.1. A direct fit to all these points is shown with the dashed gray line in the figure. When we force a value of $B/T = 1$ for $T_{\mathrm{Type}} = -5$, our final fit is functionally similar to that of Caramete and Biermann (2010, Fig. 1), but now for a significantly larger and more recent dataset and over a T_{Type} range specifically selected for our final purpose. The final fit is,

$$B/T = 0.05 + 0.36 \left(7.72^{-0.1 \cdot T_{\mathrm{Type}}} \right) \tag{3.4.1}$$

which results in a 13% increase in B/T at $T_{\mathrm{Type}} = -5$ compared to the direct fit to all datapoints, while for $T_{\mathrm{Type}} \geq -1$ the difference is negligible.

3.5 Stellar and Bulge mass from WISE photometry

The process of converting WISE photometry to stellar mass is described in C14, who take advantage of the fact that W1 is an exceptional tracer of the bulk of stellar population in galaxies and that the W1−W2 color can constrain the M/L ratio. For their (and our) calculation, the W1 absolute magnitude of the Sun is taken from Willmer (2018). J23 have presented an updated M_* estimator valid across a larger redshift range, making use of multi-color criteria and K-corrections. We use the K-corrections of the latter (see Section 3.1) for W1 and W1−W2 colors together with the stellar mass estimator of C14 to derive the total stellar mass (M_*).

To avoid excessive (and likely erroneous) M/L values estimated from W1−W2 colors, our algorithm limits the input W1−W2 values to the range −0.2 to 0.6 (corresponding to high and low M/L). Any source with a W1−W2 color outside this range is clipped to the nearest limit M/L, i.e., the distribution of W1−W2 (generated by the random normal samples of W1 and W2, see Fig. 1.0.2 and Sect. 3.7) is shifted until the median value reaches the closest limit value.

Once M_* and its errors are calculated following the process outlined above, the value is stored unless the estimated mass is $\log M_* \leq 6.5$ or $\log M_* \geq 13$. This range is more strictly constrained at the low mass end than other catalogs, and more lax at the high mass end (e.g., Dimauro et al., 2018; Durbala et al., 2020). The flexibility at the high mass end is in order to not lose extremely rare extreme SMBHs, often called ultra massive black holes (UMBHs, e.g, Runge and Walker, 2021) and SMBH upper-limits, e.g., QSO with high M/L, which produce very high M_{BH} estimates, but which are flagged as upper limits. The lower limit value is extracted directly from J23.

The WISE2MBH M_* estimates derived here are compared to two low redshift control samples from Mendel et al. (2014, $z \leq 0.4$) and Chang et al. (2015, $z \leq 0.5$) in Fig. 3.5.1 and to a group of SDSS samples (Chen et al., 2012; Maraston et al., 2013; Montero-Dorta et al., 2016), all for $z \leq 0.5$. For the samples of Mendel et al. and Chang et al., the agreement is relatively good, with a scatter of ~ 0.2 dex in both cases. There is a slight tendency for WISE2MBH M_* to be underestimated
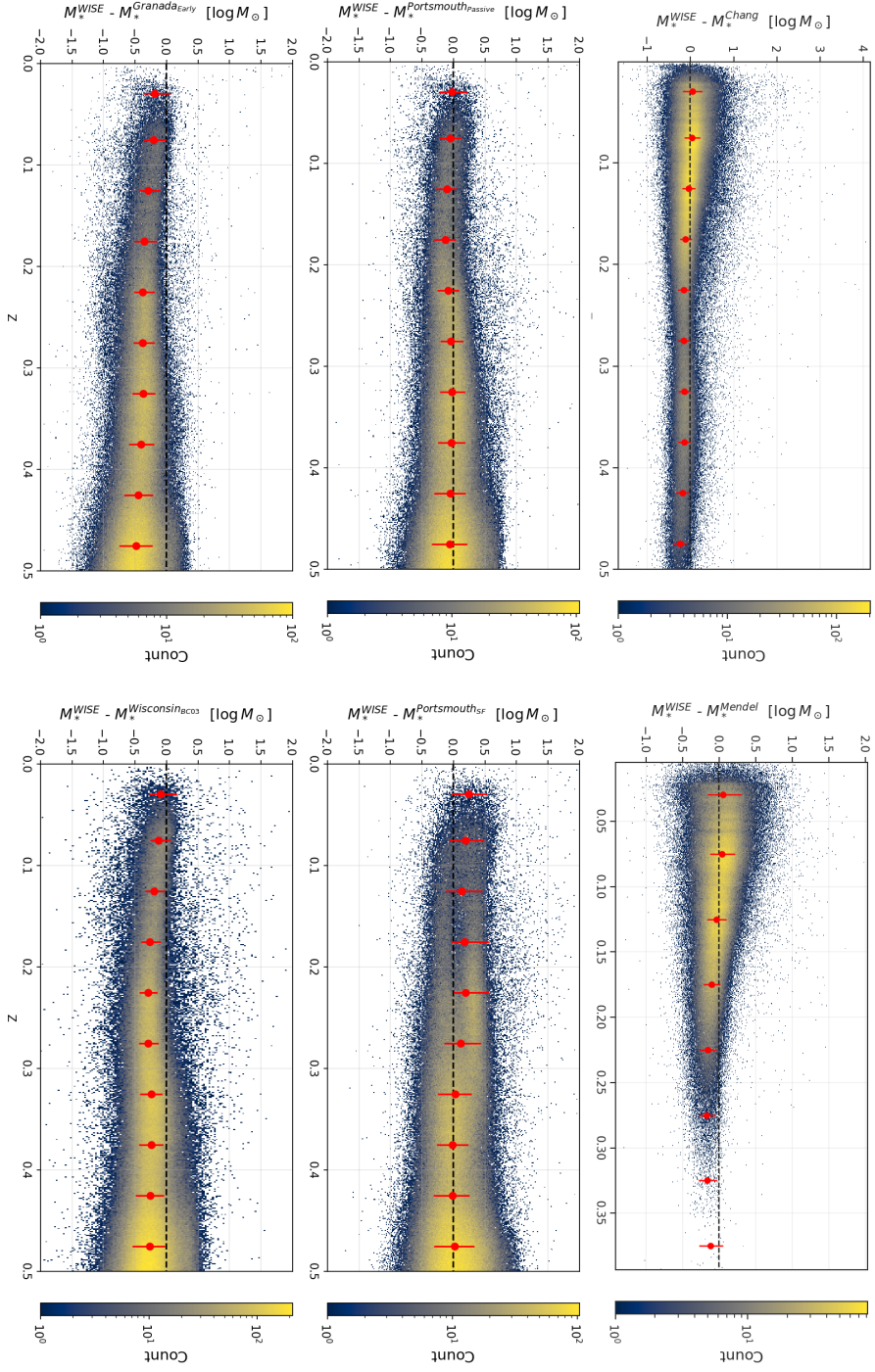
Figure 3.5.1: WISE-derived M_* compared to the low redshift ($z \lesssim 0.5$) samples of Chang et al. (2015, Top right) and Mendel et al. (2014, Top left) and updated samples from SDSS using the methods from the Portsmouth (Maraston et al., 2013, Middle), Granada (Chen et al., 2012, Bottom right) and Wisconsin (Montero-Dorta et al., 2016, Bottom left) groups. The black dashed line shows the line of equality and red dots with error bars represent the median and 1σ dispersion of the difference between masses for slices of 0.05 in redshift. Colors represent the counts in that specific region.
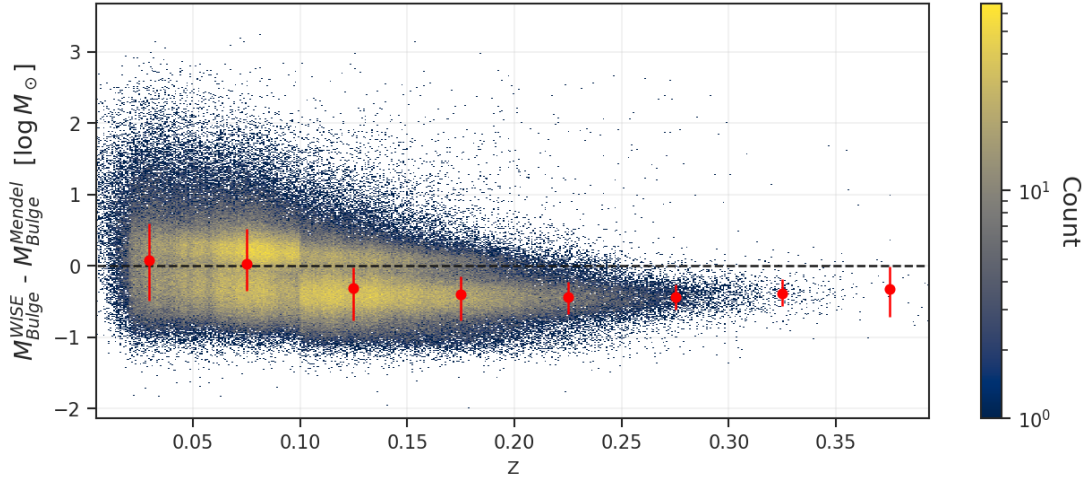
Figure 3.5.2: Same as Fig. 3.5.1, now for WISE-derived $M_{\rm Bulge}$ compared to the low redshift ($z \leq 0.4$) sample of Mendel et al. (2014).

with increasing redshift compared to some of the SDSS samples, No strong evidence was found to suggest that SDSS estimates are superior to WISE2MBH estimates, as correlations and scatter between samples did not demonstrate a preference. For a complete discussion of this, see the Appendix A3.

The $M_{\rm Bulge}$ are obtained by combining B/T with M_*. Effectively, the estimated B/T allows the estimation of both $M_{\rm Bulge}$ and $M_{\rm Disk}$. In the WISE2MBH final sample, we provide only M_* and B/T for simplicity. Figure 3.5.2 presents a comparison of WISE2MBH bulge masses with those derived by Mendel et al. (2014) in a low redshift sample: once again, the agreement is relatively good, but now shows an increased scatter. This comes from the assumption of the evolution of B/T with $T_{\rm Type}$, which do not consider other important factors for galaxy evolution such as gas availability, molecular gas content, size distribution, stellar age, and the impact of bars and bulges on it (e.g., Laurikainen et al., 2007; Fisher and Drory, 2011; Koyama et al., 2019).

3.6 Black Hole Mass from WISE photometry

The value of $M_{\rm Bulge}$ calculated in the previous section is used to derive the first estimate of $M_{\rm BH}$ using the $M_{\rm BH} - M_{\rm Bulge}$ relationship of Schutte et al. (2019).

These first $M_{\rm BH}$ estimates were compared with a control sample presented in Table 3.6.1. This consists of 152 galaxies with directly measured $M_{\rm BH}$ from different
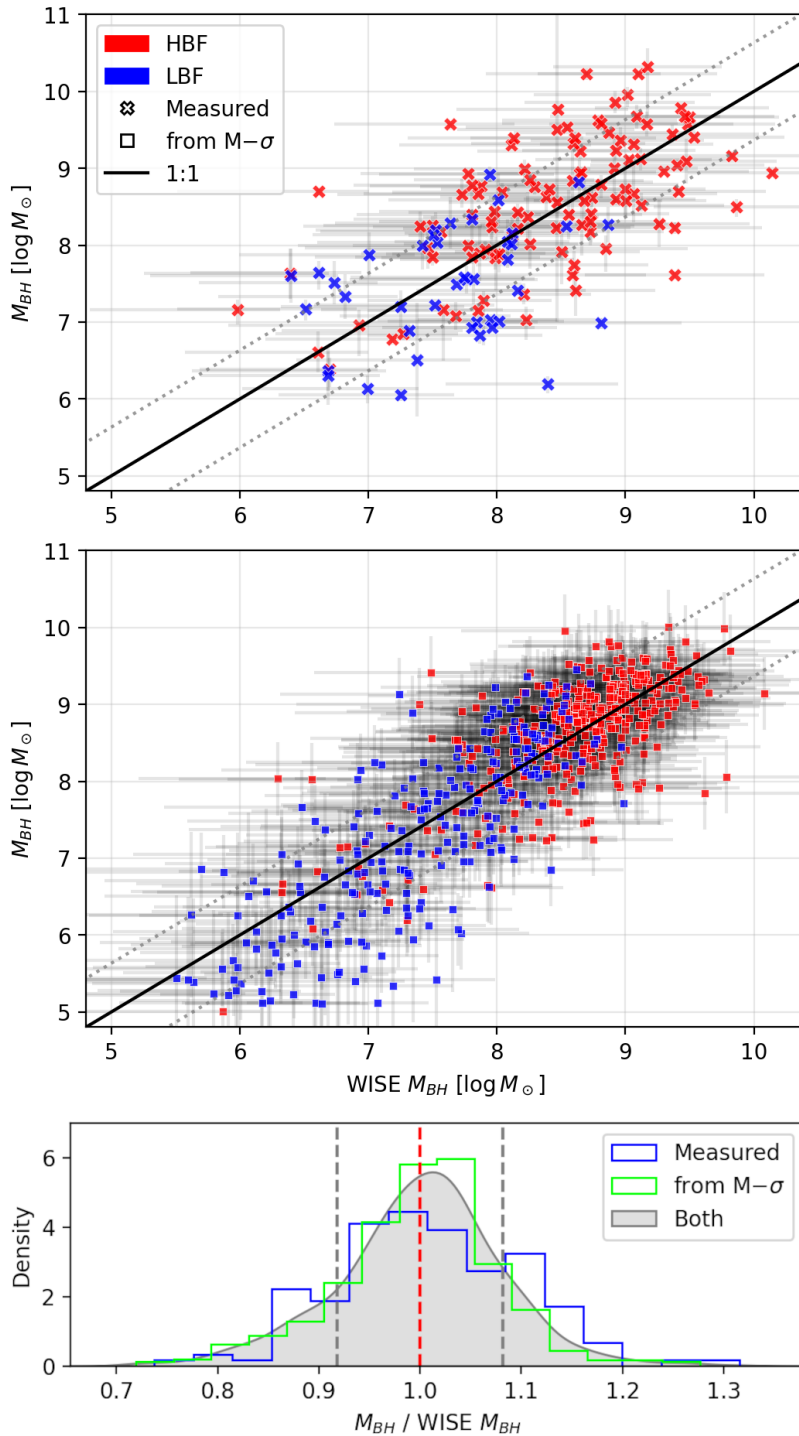
Figure 3.6.1: A comparison of measured black hole masses (Top, crosses) and highly reliable black hole mass estimates (Middle, boxes) vs. WISE-derived $M_{\rm BH}$ values in the WISE2MBH final sample. Each data point is marked with its 1σ error bars. Subsamples of HBF and LBF galaxies are distinguished by color following the inset. Gray dotted lines are the RMSE scatter bands. The bottom panel shows the distribution of the mass ratios for subsamples of measured and estimates and a KDE for the complete distribution; the mean ratio and $1\ \sigma$ dispersion (1.00 ± 0.08) of the latter are shown with red and gray dashed lines.
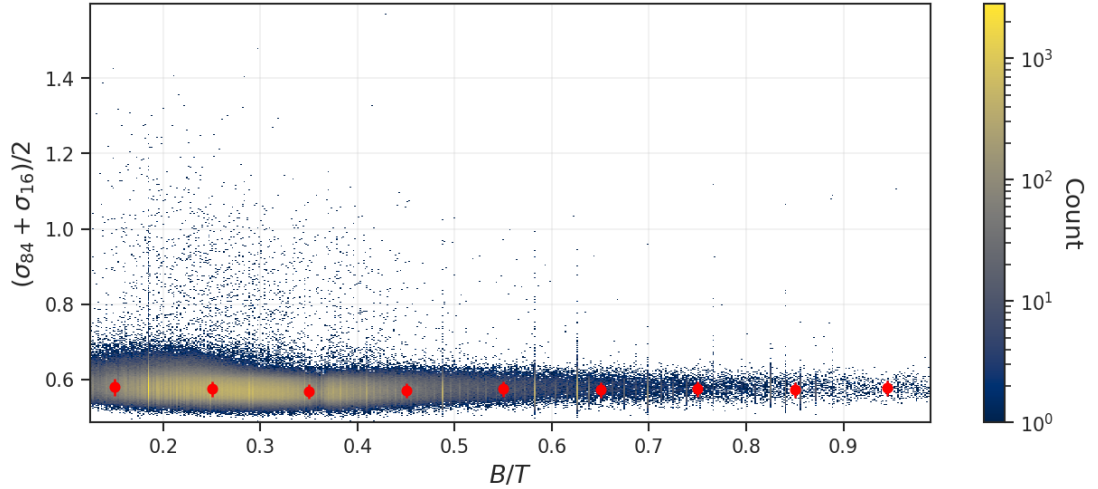
Figure 3.6.2: Mean M_{BH} errors as a function of B/T. The errors tend to be more scattered in LBF than in HBF, i.e., larger errors. This can be explained with the extension of the source. HBF sources tend to be more extended than LBF, meaning that their fluxes have better quality (i.e., lower errors).

methods (e.g., Saglia et al., 2016; van den Bosch, 2016) and 647 galaxies for which high-quality stellar velocity dispersions (σ) were available, obtained via observations with HET (van den Bosch et al., 2015). Using these σ allowed us to accurately estimate M_{BH} using the well-known M-σ relationship of Saglia et al. (2016).

This control sample was selected according to the following criteria: (a) the value of M_{BH} is flagged as a measurement or high-quality estimate from σ, (b) the M_{BH} estimate from WISE2MBH is not an upper limit, (c) the source has an `ex` flag equal to 5 and (d) the control sample source must have $\log M_{\mathrm{BH}} \leq 10.32$. While points (a) and (b) are self-explanatory, (c) is required to consider only completely extended sources, and (d) is necessary since van den Bosch et al. (2015) contains a few very large σ values. To avoid those, we consider the maximum value from van den Bosch (2016), who used the same observations from HET to measure M_{BH}, as a limit for our control sample. The control sample covers a mass range from $\log M_{\mathrm{BH}}$ of ~6 to ~10, this being almost the complete mass range for SMBH. The heterogeneity of this control sample is discussed in Sect. 5.2.

Linear regression revealed a slope of 0.9 and an intercept of 0.98. A t-test was then used to check the statistical significance of these results compared to a linear regression close to the equality line (expected slope of 1 and intercept of 0) with a

Table 3.6.1: Control sample of M_{BH} measurements and reliable M$-\sigma$ estimations.

N	M_{BH} / WISE M_{BH}	Method	Publication
16	1.06 ± 0.08	Gas dynamics	ETHER compilation[a]
46	1.01 ± 0.08	Stellar / Gas dynamics Megamaser RM	van den Bosch (2016)
13	1.03 ± 0.10	Stellar dynamics	Saglia et al. (2016)
6	0.97 ± 0.05	Stellar dynamics	Thater et al. (2019)
71	1.00 ± 0.10	Stellar / Gas dynamics Megamaser	Gültekin et al. (2019)
647	1.00 ± 0.08	M$-\sigma$	van den Bosch et al. (2015)
799	1.00 ± 0.08		

Notes: [a]From Nagar et al. (in prep) in ETHER sample. See R23 for a complete description of the compilations.

p-value of $p = 0.05$. The results showed that the slope did not differ significantly from the equality line, while the intercept was significantly different from zero, suggesting the need for a compensation factor. These findings demonstrate the presence of subtle, yet systematic, discrepancies between the WISE-derived M_{BH} estimates and the values of the control sample. To address these systematic offsets empirically, a compensation factor (C_f) is defined as follows,

$$C_f = -0.104 \log M_{\text{BH}} + 0.98 \tag{3.6.1}$$

and added to the estimate. After this empirical correction, a Spearman score of 0.78 and a root mean squared error (RMSE) of 0.63 dex (see Fig. 3.6.1) were calculated for the set of compensated estimates and control sample. Since the bulk of the control sample are HBF, the small offset of LBF shown at lower M_{BH} ranges does not affect the overall comparison, but may be interpreted as the need for a specific C_f for LBF sources or a misbehavior of previous steps for these types of galaxies, e.g., underestimation of B/T or M_*.

The $M_{\text{BH}} - M_{\text{Bulge}}$ scaling relation of Schutte et al. can be modified using the derived C_f, obtaining the following modified scaling:

$$\log M_{\text{BH}} = 1.12 \log \left(\frac{M_{\text{Bulge}}}{10^{11}} \right) + 8.84 \tag{3.6.2}$$

Finally, in case the algorithm estimates a $\log M_{\mathrm{BH}} \leq 5$, the source is dropped. While the $M_{\mathrm{BH}} - M_{\mathrm{Bulge}}$ relation of Schutte et al. (2019) can reach $\log M_{\mathrm{BH}} \leq 5$, such black holes go down to the limits of intermediate mass black holes (IMBH). IMBHs and their host populations are an active topic of research (for a review, see Greene et al., 2020), and these populations do not necessarily follow the several scaling relations used in WISE2MBH. This also means that estimates of a little more than $M_{\mathrm{BH}} = 5$ should be treated with caution.

3.7 Algorithm

The WISE2MBH algorithm was conceived with the purpose of addressing the lack of M_{BH} estimates for more than 80% of the ETHER sample (see Sect. 5.3). Nevertheless, it provides a simple and uniform tool with wide-ranging applications in studies of morphology and galaxy and black hole evolution. It is useful for both generation of large samples from existing data, and of sub-samples for future observations and monitoring with observational facilities.

This main steps of the algorithm are summarized in Fig. 1.0.2. In summary, the process is as follows:

- W1, W2 and W3 magnitudes and a spectroscopic redshift are used to calculate the K-corrected W1 absolute magnitude, W1−W2 and W2−W3 colors with the use of lookup tables from J23 (see Sect. 3.1).

- The K-corrected W1 absolute magnitude and the W1−W2 color are used to estimate M_* of the source with the process described in C14. For that calculation, the W1 absolute magnitude of the Sun is taken from Willmer (2018) (see Sect. 3.5).

- The source is placed into the estimate or upper limit zone, making use of several inputs (see Sect. 3.2).

    - If a source is placed in the estimate zone and its T_{Type} is available, it continues in the algorithm.

    - If a source is placed in the estimate zone and no T_{Type} is available, the latter is estimated from the W2−W3 color (see Sect. 3.3).

    - If a source is placed in the upper limit zone, its T_{Type} is not considered

      if available, nor calculated if not available.

- The T_{Type} of the source is used to estimate B/T; for sources in the upper limit zone B/T is set to 1 (see Sect. 3.4).

- M_{Bulge} is estimated using the previously derived M_* and B/T (see Sect. 3.5).

- A first M_{BH} estimate is obtained using the $M_{\mathrm{BH}} - M_{\mathrm{Bulge}}$ relation of Schutte et al. (2019).

- The final estimate of M_{BH} is obtained after adding C_f to the first estimate. Sources with M_{BH} in the range of IMBH are dropped.

Not every source enters the algorithm. There are two main reasons for a source to be rejected during the algorithms pre-processing: (a) the source does not have a spectroscopic z available, or (b) the quality of the WISE magnitudes are not considered 'usable', i.e., `qph` from the AllWISE catalog is not equal to `A, B, C` or `U`, for the W1, W2 and W3 bands. A source can be dropped during an intermediate step of the algorithm if M_* or M_{BH} are considered outliers (described in Sects. 3.5 and 3.6).

The algorithm uses a Monte Carlo approach to estimate errors. It generates random normal samples (using arrays of size 10^4) for the W1, W2, and W3 magnitudes and respective mean photometric errors for each source. These distributions are propagated through the algorithm, where errors in the scaling relations used, if available, are considered, thus delivering a final M_{BH} (or other estimated quantity) with asymmetric error bands for each source that was not rejected. The C_f is applied to the final distribution of values and not only to the nominal value. The nominal, low, and high values reported are the median and 1σ percentile values of the final distribution, respectively. Two examples of the final error distributions can be seen in Fig. A1.1.

Chapter 4

Results and Analysis

4.1   WISE2MBH final sample

When used with the WISE2MBH parent sample, the algorithm generates $\sim$2 million M_{BH} estimates and upper limits, rejecting only 3.9% of the parent sample. A summary of the statistics in the final sample is shown in Table 4.1.1.

Percentages listed represent the percentage with respect to the total value of a given object type. New WISE2MBH estimations are those for which no previous measurement / estimate of M_{BH} existed in the ETHER sample. Almost 80% of the final sample are first-time M_{BH} estimates or upper limits, most of which come from galaxies and unknown object-type sources that reside in the estimate zone of Fig. 3.1.3.

The table of our WISE2MBH final sample provides the source name, RA and DEC in degrees from the AllWISE catalog, spectroscopic redshift, object type, T_{Type} used (either from ETHER or calculated by the algorithm), plus the estimates of M_*, B/T, median plus 1σ values of M_{BH} as estimated by the algorithm and a quality flag for each source. An excerpt of the table is shown in Table 4.1.2.

The 7-digit quality flag that we provide stores important information for selection of subsamples. The first four digits of this flag sequentially report the photometric quality of the measurements in the W1, W2, and W3 bands, as well as the extension flag of the source of AllWISE. The fifth digit serves as a binary indicator for the upper limit condition, where 0 denotes an estimate and 1 an upper limit.

Table 4.1.1: Statistics of the WISE2MBH final sample.

	All M_{BH}		Galaxy		QSO		RS		Unknown	
	Total	New (%)	Total	New (%)	Total	New (%)	Total	New (%)	Total	New (%)
Any	2013511	1580707 (78.51)	586008	435904 (74.39)	15802	7374 (46.66)	6582	6444 (97.90)	1405119	1130985 (80.49)
Est.	1904108	1495247	555919	411202	—	—	—	—	1348189	1084045
Est. (%)	94.57	74.26	94.87	70.17	—	—	—	—	95.95	77.15
Uplim.	109403	85460	30089	24702	15802	7374	6582	6444	56930	46940
Uplim. (%)	5.43	4.24	5.13	4.22	100	46.66	100	97.90	4.05	3.34
Rejected	82075		15651		398		2778		63248	

Table 4.1.2: Excerpt of the WISE2MBH final sample.

Name (WISEA)	RA (°)	DEC (°)	z	Object type	T_{Type}	M_* (log $M_\odot$)	B/T	$_{50}M_{\text{BH}}$ (log $M_\odot$)	$_{16}M_{\text{BH}}$ (log $M_\odot$)	$_{84}M_{\text{BH}}$ (log $M_\odot$)	Quality
J005254.81-260228.5	13.228403	-26.041252	0.075047	Galaxy	8.00	10.33	0.13	7.13	6.49	7.76	AAA0001
J085853.20+381944.2	134.721705	38.328948	0.089774	Unknown	-5.00	10.40	1.00	8.19	7.58	8.83	AAA0000
J090734.40+502953.9	136.893367	50.498308	0.149000	QSO	-.-	9.96	1.00	7.70	7.14	8.34	AAB0122
J143516.80-482147.8	218.820003	-48.363285	0.164000	RadioSource	-.-	10.86	1.00	8.74	8.14	9.36	AAB0122
J090536.54+612254.9	136.402256	61.381936	0.178334	Unknown	1.49	11.11	0.32	8.44	7.81	9.06	AAU0001
J072846.20+404954.0	112.192538	40.831674	0.217425	Unknown	1.99	11.10	0.29	8.42	7.82	9.04	AAU0001
J231318.65+094133.4	348.327736	9.692628	0.328817	Unknown	2.58	11.18	0.27	8.39	7.72	9.07	AAU0001
J120245.58+071133.3	180.689952	7.192605	0.400000	Galaxy	-.-	10.86	1.00	8.74	8.06	9.32	AAA0122
J120939.83+344601.5	182.415971	34.767088	0.434100	QSO	-.-	11.07	1.00	9.00	8.34	9.64	AAA0122
J230846.43+173546.2	347.193464	17.596178	0.470583	Unknown	4.81	11.12	0.19	8.19	7.59	8.82	AAU0001

Note: Some values are rounded for table presentation. The full version of this table will be available online via CDS.

The sixth digit characterizes the quality of K-correction; a value of 0 denotes an optimal correction, 1 is a suboptimal correction, and 2 indicates that K-correction was not applied. Lastly, the seventh digit denotes the origin of the T_{Type} estimate. A value of 0 implies a source with a known T_{Type}, 1 indicates an estimated T_{Type}, and 2 indicates direct rejection due to an upper limit condition. In particular, it is important to clarify that the seventh digit does not inherently rank the quality of the T_{Type} estimate as superior or inferior, as the available T_{Type} values can come from binary classifications, as described in Dobrycheva (2013), or consider all morphological categories, as in the case of 2MRS. This is discussed in Sect. 5.2.

The highest quality sources (HQS) are classified as `AAA500` in the first six digits, while the lowest quality sources (LQS) have the fourth and fifth digits equal to `01`. Examples of HQS and LQS sources can be seen in Fig. A1.2. These sources illustrate the wide range of sources which the algorithm deals with, with HQS being mostly nearby galaxies large enough to have top quality in W1, W2, W3 and also being considered completely extended, while LQS are mostly QSO and compact very late-type galaxies. While HQS is not a strict proxy of the best M_{BH} estimates, we recommend using this sub-sample (118367 HQS, more than half of them (82812) also classified as galaxies) when a highest reliability sample is required. Most QSO and RS are classified as LQS (all of their M_{BH} are upper limits), due to the resolution limits of WISE and 2MASS, and/or AGN contamination (see Sect. 5.1).

The errors in the estimates tend to be smaller in HBF sources than in LBF sources, since the extension of the sources allows for better quality in the WISE magnitudes. In Fig. 3.6.2 it is possible to see that behavior for a few tens to hundreds of sources at LBF.

Final distributions of M_* and M_{BH} for each object type can be seen in Fig. 4.1.1. It is clear that QSO and RS tend to have more massive M_* and M_{BH}, this due to the upper limit classification of them, thus the use of $B/T = 1$. Galaxies are mostly estimates; the B/T ratio is used here when estimating M_{Bulge} and M_{BH}. More than 80% of sources with unknown type are estimates, and show almost the same distribution as in galaxies by very different from QSO and RS.
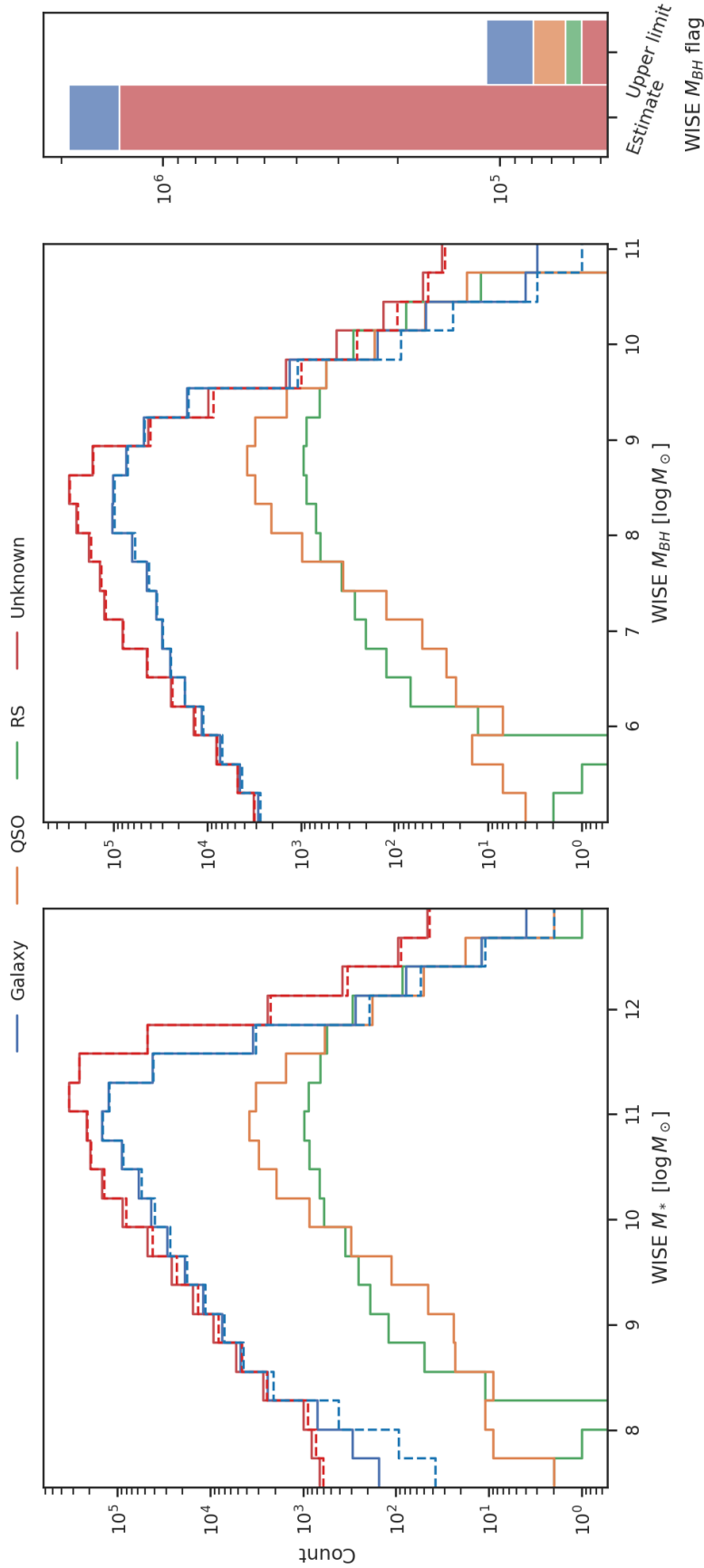
Figure 4.1.1: Distribution of M_* (left panel) and M_{BH} (middle panel) for the WISE2MBH final sample. For Galaxies and Unknown, two distributions are shown; the dashed line for estimates and upper limits. The distributions change slightly from one panel to the other, due to the use of B/T to obtain M_{Bulge}. Galaxies tend to be relatively less massive, both in M_* and M_{BH} due to contamination in sources with other types, increasing flux in the W1 band, thus leading to more massive estimates. Galaxies and unknown types are also affected by their B/T, while other object types are not (excluding a low percentage of unknown type sources). The right panel shows a stacked histogram illustrating the number of M_{BH} estimates and upper limits for each object type.
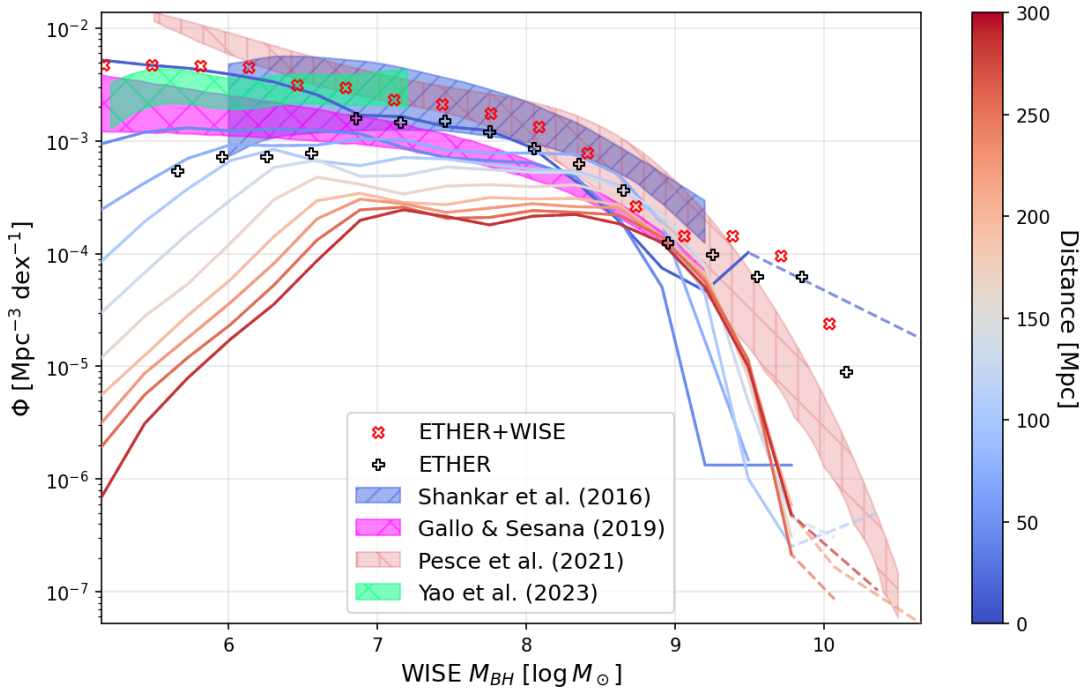
Figure 4.2.1: Black hole mass function (BHMF) in the WISE2MBH final sample for shells of width 30 Mpc ending at distances of 30 to 300 Mpc, following the color bar at right. ETHER+WISE and ETHER points represent the BHMF present in ETHER with and without considering WISE M_{BH} estimates. For reference we show four BHMFs independently derived by Shankar et al. (2016); Gallo and Sesana (2019); Pesce et al. (2021); Yao et al. (2023).

4.2 Local black hole mass function

The local black hole mass functions (BHMFs) of the WISE2MBH final sample can be seen in Fig. 4.2.1 for shells of increasing distance out to 300 Mpc. These WISE2MBH final sample BHMFs are compared to the local BHMF in R23, and other BHMFs from independent methods: Shankar et al. (2016, compensated M_{BH}-σ), Gallo and Sesana (2019, X-ray), Pesce et al. (2021, M_{BH}-M_*) and Yao et al. (2023, TDE). The WISE2MBH final sample BHMF was derived using only estimates from WISE. At $\log M_{\mathrm{BH}} > 10$, the WISE2MBH final sample has only a few (elliptical) galaxies, so that the derived BHMFs shows large fluctuations given the small number statistics. For this reason, the BHMFs at $\log M_{\mathrm{BH}} \gtrsim 10$ are shown as dashed lines.

The symbols in the figure show two cases of the BHMF for BHs at $D \leq 30$ Mpc: (a) using only estimates present in ETHER before the WISE2MBH algorithm (black symbols), and (b) using ETHER estimates, and in the absence of these, using estimates from WISE2MBH (red symbols). The difference between these two cases, and the WISE2MBH BHMF at $D \leq 30$ Mpc (darkest blue line) is clear. At low masses ($\log M_{\mathrm{BH}} \leq 7$) the ETHER-only BHMF is significantly lower than the other two. The ETHER+WISE (red symbols) and WISE2MBH BHMF agree well between each other and sit on or between previously derived literature expectations. At the high mass end the WISE2MBH BHMFs in all distance shells drop significantly below the ETHER and ETHER+WISE BHMFs and also the literature expectations. That is, pure WISE-based estimations do not find the few massive known black holes in the local universe. The increasing incompleteness of the WISE2MBH BHMFs with distance, especially at lower masses is due to the distribution of z in the sample.

The lack of SMBH populations in the lower and higher ranges could be interpreted as an indication of some physical processes that can limit the growth of SMBH beyond a certain mass and below a certain threshold. Feedback from SMBH or their host galaxies may inhibit the formation (growth) of low-mass black holes (SMBH seeds) or limit the growth of high-mass ones (for a review, see Inayoshi et al., 2020). Alternatively, the drop-off in the mass function could be an artifact of observational biases or limitations in the current data sets.

The combination of less massive M_* estimates and low B/T for spiral galaxies in the

sample can lead to differences at the low mass end when comparing WISE2MBH BHMFs to other BHMFs in the literature. In any case the ETHER-only BHMF is lower than literature expectations due to the construction of the sample: galaxies with an estimated black hole mass of $\log M_{BH} \leq 5.5$ were eliminated from the sample, but note that galaxies without black hole masses remained in the sample and for these WISE2MBH could later add a mass estimate. The ETHER+WISE BHMF is in good agreement with other BHMF that obtain similar densities.

The BHMFs from Gallo and Sesana (2019) and Yao et al. (2023) are mostly focused in lower mass ranges. The former used the stellar mass function derived from Galaxy And Mass Assembly (GAMA) together X-ray imaging from the *Chandra* Observatory, to constrain the BHMF down to low-mass regimes ($\log M_{BH} \geq 4$). The latter was derived by studying tidal disruption events (TDE), which are less frequent in SMBH with higher masses ($\log M_{BH} \geq 7$); they argue that their BHMF over $\log M_{BH}$ 5 to 7 could be considered as an upper limit. With that information, a limit was established and our BHMF is in good agreement with that.

The BHMF of Shankar et al. (2016) is the most widely used for comparisons, due to the compensated phenomenology used to derive it, as compared to the BHMF previously derived in Shankar et al. (2009). The Shankar et al. (2016) BHMF corrects the low-mass range, now showing a clear downward trend, but it is still limited in M_{BH} range. Pesce et al. (2021) used the Shankar et al. BHMF to build an updated BHMF which extrapolates to higher mass ranges, but does not update the low-mass end BHMF. The WISE2MBH BHMFs are lower at both the high and low mass end as compared to Shankar et al. (2016) and Pesce et al. (2021).

Chapter 5

Discussion

5.1 Assumptions and limitations

The algorithm makes several assumptions and approximations, potentially introducing biases, particularly for certain types of galaxies. As highlighted by Jarrett et al. (2019) and Cluver et al. (2020), despite the reduced sensitivity of the W3 band compared to W1 and W2, leading to fewer detections (as noted by Jarrett et al., 2013), the color W2−W3 has been shown to be an effective indicator of morphology. Therefore, we choose to use this color to estimate the morphology. The galaxy-averaged W1−W2 color (rather than the colors of the individual components, e.g., bulge and disk) is assumed to correctly trace the averaged M/L ratio as C14 and J23 suggest, and is effectively used for this purpose.

Our estimations of M_* come from the method of C14, which presents a different dependence of M/L on W1−W2 compared to J23, which was the method for which the K-corrections were developed. Despite this, our most important goal with respect to the ETHER sample is not M_* estimates, but rather M_{BH} estimates. The latter showed better agreement with measured M_{BH} values in the literature when using the method of C14.

We use the empirical relationship of (Schutte et al., 2019) to convert the WISE-based bulge masses to a SMBH mass. For this conversion, a comparison of WISE2MBH M_{BH} to the control sample of SMBH measurements and high quality estimates shows a slight offset from equality. The best fit compensation factor (C_f) is positive for an initial M_{BH} estimate with $\log M_{\mathrm{BH}} < 9.42$. When the first

estimate of $\log M_{\mathrm{BH}}$ is much lower than this value, the compensation factor can lead to extreme compensations. For example, when the first M_{BH} estimate is $\log M_{\mathrm{BH}} = 4.6$, thus a $C_f = 0.5$, then a final M_{BH} estimate of $\log M_{\mathrm{BH}} = 5.1$ is stored. In this example, if C_f was not applied, the source would have been dropped from the final sample.

We are unable to explain the need and functional form of this C_f. That is, it is purely empirical. It could reflect systematics in WISE2MBH or in the control sample. At this point, it is easiest to consider C_f as a posterior modification of the relationship of Schutte et al. that is used to convert M_{Bulge} to M_{BH} in WISE2MBH.

In Fig. 5.1.1, it is clear that the modified scaling of Schutte et al. is almost perfectly aligned with the relation of Kormendy and Ho (2013), which presents a strong compensation for the lower mass ranges, as stated above. This shows that our final estimates effectively show a population of SMBH with grater masses than the ones predicted from Schutte et al., but considering that our estimates are highly biased by detection by WISE, dwarf galaxies, the major difference between the scalings discussed here, can be dropped by the algorithm in various steps, including the notorious drop at $\log M_{\mathrm{BH}} = 5$, which can obviously lead to the use of only high-mass SMBH.

The compensation factor obviously biases the final WISE-derived M_{BH} estimates to predict a population of SMBH mostly similar to the few local sources that have measurements or reliable estimates of M_{BH}. Given that we use this same C_f for all redshifts in WISE2MBH, this can lead to systematic errors at higher redshifts. This underlines the need for more and better direct measurements of M_{BH} over a range of redshifts, plus a review of systematics in previous measurements (e.g., Liepold et al., 2023).

The algorithm is limited by the relatively low angular resolution of WISE ($\geq 6.1''$), i.e., its limited capacity to constrain the extension or morphology of compact sources. This factor, combined with a certain degree of AGN contamination in some cases, exacerbates the classification of some targets as upper limits (rather than estimates) using the color-color criteria described in Sect. 3.1.3, causing us to use unnecessarily large values of M_{Bulge} (due to fixing $B/T = 1$) and thus providing overestimated M_{BH} values as an upperlimit.
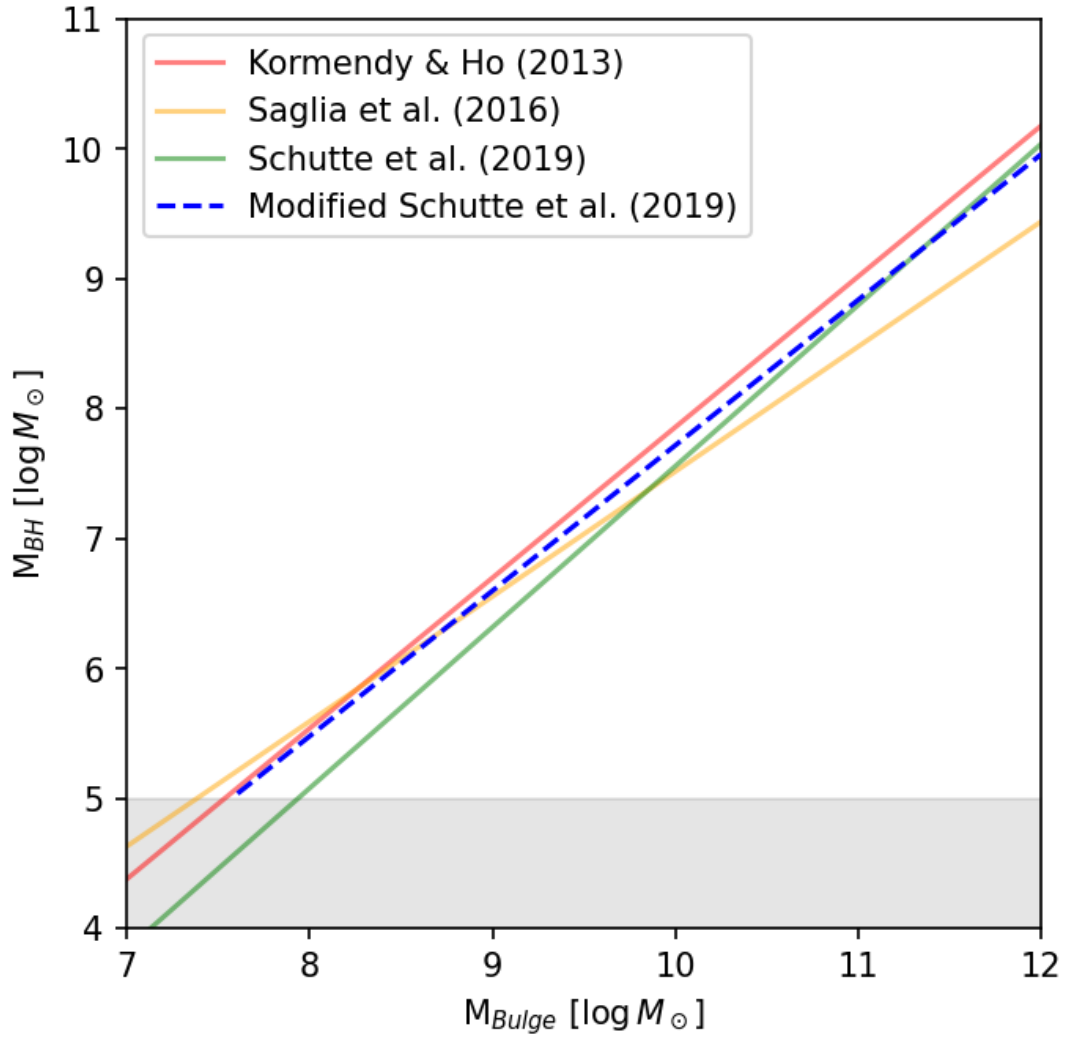
Figure 5.1.1: Comparison of different $M_{\mathrm{BH}} - M_{\mathrm{Bulge}}$ scaling relations from the literature, including Kormendy and Ho (2013); Saglia et al. (2016); Schutte et al. (2019) and the modified scaling presented in this work. Grey area represents the limit of the WISE2MBH algorithm for $M_{\mathrm{BH}} < 5$, where it drops all estimates.
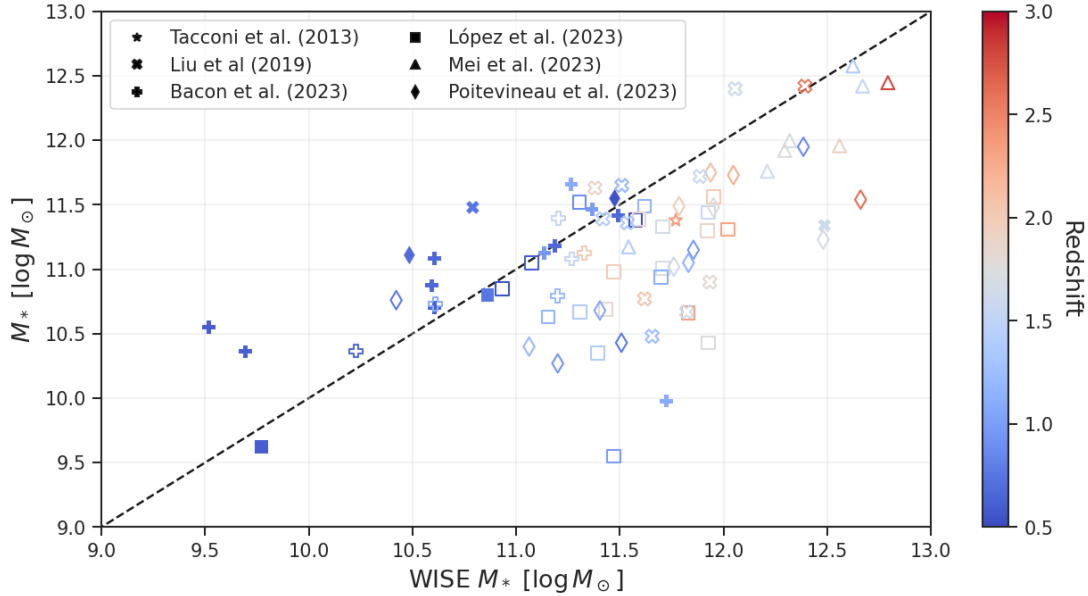
Figure 5.1.2: WISE-derived M_* compared to the high redshift ($z \geq 0.5$) samples of Tacconi et al. (2013); Liu et al. (2019); Bacon et al. (2023); López et al. (2023); Mei et al. (2023); Poitevineau et al. (2023), with colors specified in the inset. The black dashed line is the line of equality. Datapoints are colored by redshift following the color bar on the right (blue is $z = 0.5$ and red is $z \sim 3$). Filled and unfilled markers are used for estimates and upper limits of WISE-derived M_*, respectively; all literature values are estimates.

5.1.1   Applicability at higher redshifts

The WISE2MBH algorithm is applicable to samples between redshifts of 0.5 and 3, as it utilizes K-correction lookup tables from J23. However, the results are highly uncertain due to the scaling being derived and calibrated for lower redshift samples ($z > 0.5$).

Specifically, the K-corrections, as presented in J23, have been made available for redshifts up to $z = 3$, but have been shown to be reliable for $z \leq 0.5$. The zone selection and object criteria are detailed in Sect. 3.2 have been applied systematically to every source within the WISE2MBH parent sample. Object selection and upper limit or rejection criteria are based on K-corrected fluxes and are thus more reliable at $z \leq 0.5$. The T_{Type} estimator, an essential component of the algorithm, was developed using the 2MRS sample, whose sources are $z \leq 0.15$. Lastly, the method used to estimate M_*, as explained in C14, has been calibrated for $z \leq 0.12$.

Figure 5.1.2 compares WISE2MBH M_* with the literature values of M_* for galaxies at $z \geq 0.5$ from a control sample from multiple catalogs (Tacconi et al., 2013; Liu et al., 2019; Bacon et al., 2023; López et al., 2023; Mei et al., 2023; Poitevineau et al., 2023). In this figure, the filled markers show sources with WISE M_* estimates and the unfilled markers show sources with WISE M_* upper limits. All literature values are M_* estimates.

In the context of these comparisons between estimates and upper limits against the control sample, the following observations hold:

- WISE estimates, having undergone prior K-correction, predominantly show a slight underestimation in their M_* values.

- WISE upper limits, which did not undergo K-correction, typically show an overestimation in their WISE2MBH M_* values. This tendency is consistent with the possible AGN contamination of these sources and the absence of K-correction. Since these are explicitly marked as upper limits in our algorithm, this does not lead to errors.

The WISE2MBH algorithm has been shown to be precise in recognizing sources that are contaminated as upper limits, due to the insignificant color-color evolution across redshift of these types of source (e.g., Mateos et al., 2012), but do not show a great accuracy in estimating M_* at redshift ranges higher than $z = 0.5$.

5.2 Building on the algorithm and heterogeneity

The WISE2MBH algorithm can be considered as an auxiliary tool for obtaining M_{BH} estimates from a homogeneous dataset. This dataset provides consistent estimates of M_{BH} using WISE data for most sources and a consistent set of relations, following accepted ideas and scaling relations applicable to the majority of extragalactic sources. Although the WISE2MBH final sample is heterogeneous in its composition (i.e. different extragalactic objects), users can define subsamples to recover homogeneity.

The use of a single, well-calibrated dataset from observations with the same instrument and method can ensure consistency and comparability of results, but may limit their generalizability and bias the final conclusions. The process described in this work does not necessarily rely solely on WISE data. WISE is

used to obtain physical properties of extragalactic sources in the ETHER sample, but external data, such as source classification and morphological types, are also employed in some cases.

Independently derived physical properties, such as M_* or M_{Bulge} can be input to an intermediate stage of WISE2MBH in order to obtain M_{BH} estimates. This approach injects heterogeneity into the algorithm and its results.

Despite the use of a homogeneous parent sample, both M_{BH} (low-z) and M_* (low- and high-z) were compared with heterogeneous control samples, the former being more important to discuss. The M_{BH} control sample is described in Table 3.6.1. The primary methods used to measure M_{BH} in the control sample are stellar dynamics, gas dynamics, and reverberation mapping (RM); all known for their reliability and precision in measuring M_{BH}. Poor quality σ, single-epoch RM, and other methods used to obtain M_{BH} in R23 were excluded. Despite the heterogeneity of the control sample, the ratio between the measured M_{BH} and the WISE-derived M_{BH} estimate was calculated in every case, and no prominent differences or scatter was found.

Authors who wish to work with a completely homogeneous subsample of the WISE2MBH parent sample which is based only on WISE data and spectroscopic redshift, could define the subsample as follows: (a) only sources with object type galaxy or unknown, and (b) only sources with a quality flag ending in 2. These constraints ensure that authors work with estimates that only used WISE data for the classification of upper limits and omit estimates that made use of previously known T_{Type}.

5.3 Relevance for the EHT and ngEHT

The EHT (and future ngEHT) is the best facility for the imaging of the innermost environments of black holes in terms of sensitivity and resolution ($\sim$10 mJy and $\sim$15 μas, Johnson et al., 2023; Doeleman et al., 2019; Pesce et al., 2022) for the next decade, opening the possibility of imaging (and making movies of) tens to hundreds of SMBH in the nearby Universe. Relevant science goals include testing general relativity, the role of magnetic fields in black hole accretion and jet formation. Recently, Pesce et al. (2021) have demonstrated that with current EHT facilities (at 230GHz), we can expect to resolve $\sim$5 new SMBH shadows,

while with ngEHT observing at 345GHz, this number can be increased by factor $\sim$3. The challenge is to identify these very rare sources.

In the context of scientific exploitation of the EHT, R23 have developed the ETHER sample and database. Combining $\gtrsim$3M sources in a parent sample of galaxies and AGN, comprehensive radio to X-ray observed spectral energy densities (SEDs), and jet and accretion flow SED modelling to predict the expected EHT flux, ETHER can provide target samples for the EHT for any given science goal. WISE2MBH was originally developed to fill large gaps in the ETHER sample: delivering both black hole mass estimates and upper limits, and galaxy morphologies. Its accuracy and ease of use, combined with its relevance to galaxy evolution studies, especially at high redshift, motivate its publication as a separate entity from ETHER.

This algorithm does not necessarily intend to replace previous estimates of M_{BH} in the literature (except for values based on poor quality σ or relatively unreliable 'fundamental planes'), but rather to increase the completeness of the ETHER sample. As more precise estimations or measurements become available (e.g., from SDSS Black Hole Mapper, Kollmeier et al., 2017, Sect. 2.2), WISE M_{BH} estimates can be replaced in ETHER.

In R23, the authors detail a methodology that requires M_{BH} estimates (or upper limits) and X-ray flux data, primarily from the *Chandra* Source Catalog (CSC) to predict the EHT-observable flux of an SMBH. With the imminent release of eROSITA DR1 in 2023[1] will provide an estimated ~ 1 million new hard X-ray flux measurements. Integrating eROSITA, WISE2MBH and ETHER, will allow SED fitting, thus radio flux estimates, for almost all sources in eROSITA. This is a critical step for target selection for the ngEHT.

---

[1] Future eROSITA data releases, including eRASS, will be published at: https://erosita.mpe.mpg.de/erass/

Chapter 6

Conclusion

This work presents a simple and new algorithm to obtain stellar masses (M_*) of galaxies, its morphological types (T_{Type}), bulge-to-total ratios (B/T) and black hole masses (M_{BH}) estimates and upper limits, the WISE2MBH algorithm, publicly available at GitHub[1]. This algorithm, which only requires WISE catalog data, classifies sources as galaxies or QSOs, and estimates multiple physical quantities such as M_* and M_{BH}. The algorithm uses previously derived scaling relations and our own derived relations to obtain a final M_{BH} estimate or upper limit. Using a parent sample of $\sim$2.1 million sources from the ETHER sample post-cross-match to AllWISE and the WISE extended source catalog (WXSC), a final sample of $\sim$2 million M_{BH} estimates and $\sim$109 thousand upper limits were calculated, and from the estimates, $\sim$80% are first-time estimates of known galaxies or unclassified sources. QSOs and radio sources (RS), as classified by NED, are also part of the sample, but due to the nature of the emission and the quality or extension of these sources in WISE, all of their final values of M_{BH} are marked as upper limits. The final sample table will be available online via CDS.

The detailed morphological classifications (T_{Type}) of galaxies in the 2MASS redshift survey (2MRS) were used to derive a relation between T_{Type} and the WISE W2$-$W3 color, with the objective of estimating T_{Type} for sources that do not have one previously assigned in the literature. All available and estimated T_{Type} are used to obtain B/T using an exponential relation described in Sect. 3.4 that is consistent with previous studies. The obtained B/T are used to calculate M_{Bulge} from a

---

[1]A general use version of the algorithm will be published at the following GitHub repository: https://github.com/joacoh/wise2mbh

WISE derived M_*. Finally literature $M_{\mathrm{BH}} - M_{\mathrm{Bulge}}$ scaling relations are used to estimate M_{BH}. All uncertainties are propagated through the algorithm using a Monte Carlo approach, delivering the 1σ (upper and lower) errors of the final distributions as low and high values, respectively.

The M_{BH} estimates were compared to a control sample of M_{BH} measurements and reliable estimates, showing a significant difference in the linear regression analysis with respect to the equality line, i.e., an offset that causes some values to be overestimated and others underestimated. To compensate for this offset, we implement a compensation factor (C_f) derived with the use of the control sample. After compensation, the comparison achieves a Spearman score of ~ 0.78 and a RMSE of ~ 0.63.

The mean uncertainty was calculated for the M_{BH} estimates, considering a simple mean between low and high errors and then taking the mean value of the distribution of means, obtaining a value of ~ 0.5, showing more scatter in low bulge fraction (LBF) sources, compared to high bulge fraction (HBF) sources (see Fig. 3.6.2).

The black hole mass function (BHMF) of the WISE2MBH final sample is in good agreement with other previously and independently derived BHMFs. The ETHER sample has few low mass estimates ($\log M_{\mathrm{BH}} \leq 6$), while the WISE2MBH final sample can provide this population of sources, and the overall combination of both samples generates the most complete BHMF.

When using the WISE2MBH algorithm or the final sample described in this work, it is important to take into account the assumptions and associated limitations. The algorithm provided on GitHub can be easily modified to change the scaling relations used or incorporate new ones, tailored to the user's requirements.

Regarding the final sample, we recommend not considering all M_* or M_{BH} estimates if the main goal is to study few sources and restrict the sources of this sample to only high quality sources (HQS). In case of population studies, almost the complete final sample can be used, depending on the distance scale, quality flag, and the needs of the user.

The final sample was generated in a homogeneous manner, i.e. all estimates come from relations that make use of WISE cataloged data to derive physical quantities, except for the use of T_{Type} from the literature in some cases. This gives confidence

that the derived values are consistent from one to another and no externally derived physical parameters were used to obtain the final M_{BH}.

The WISE2MBH final sample is already incorporated into the ETHER sample, providing almost 3 million new M_{BH} estimates and upper limits that, and it will be used iteratively to provide up-to-date values in case new sources are ingested into the ETHER sample. These estimates are crucial for the selection of samples of interest for the Event Horizon Telescope (EHT) and the next-generation EHT (ngEHT), and are used on each update of the sample. Its high percentage of success in estimating a new M_{BH}, combined with spectral fitting of accretion and jet models to hard X-ray data from Chandra, and eROSITA in the near future, allows one to predict radio fluxes from the accretion inflow and jets, and thus obtain a first selection of sources detectable with the EHT or ngEHT.

Acknowledgements

A1   Diversity of objects in the WISE2MBH final sample

As stated in Secs. 3.2, 3.3 and 4.1, the object type is an input. The algorithm estimates multiple parameters or classifications for the objects, e.g., high and low bulge fractions (HBF and LBF) and high and low quality sources (HQS and LQS). Examples comparing an LBF and a HBF objects can be found in Fig. A1.1. Figure A1.2 contrasts two examples of HQS sources (top row) with two examples of LQS sources (bottom row).

A2   Comparison for various samples in W2-W3 color to T-Type conversion

Our conversion of $W2-W3$ color to T_{Type} was calibrated with galaxies in the 2MRS sample (Sect. 3.3). To explore the reliability and errors of this conversion, we used the same method of Sect. 3.3, but for other samples present in Hyperleda (Makarov et al., 2014).

Hyperleda includes the Huchra et al. (2012, 2MRS), Willett et al. (2013, GZ2), and Dobrycheva (2013) samples, which collectively represent more than 70% of the available values for T_{Type} in Hyperleda (25k, 310k, and 350k values, respectively). Each sample was tested following the same approach described in Sect. 3.3 for 2MRS, with results shown in Fig. A2.1.

The GZ2 sample exhibits a clear bimodality in T (bottom row of Fig. A2.1). The authors provide detailed classifications for spiral galaxies, allowing clear differentiation from Sa to almost Sd classifications (1 to 6 in T_{Type}). However, in the morphological range from lenticular to elliptical, the level of detail is completely lost: all except 530 (i.e. 98%) of these sources are classified as $T_{\text{Type}} = -5$.

Dobrycheva classified their sample galaxies into two bins: T_{Type} equal -5 and 5 (i.e. ellipticals and spirals; bottom row of Fig. A2.1). Although this binary classification has demonstrated efficacy for machine learning training and subsequent classification of different samples (e.g., Vavilova et al., 2021, 2022), it does not provide the level of detail required for our $W2-W3$ color to T_{Type} calibration. Nevertheless, we use this sample here only for comparison purposes.
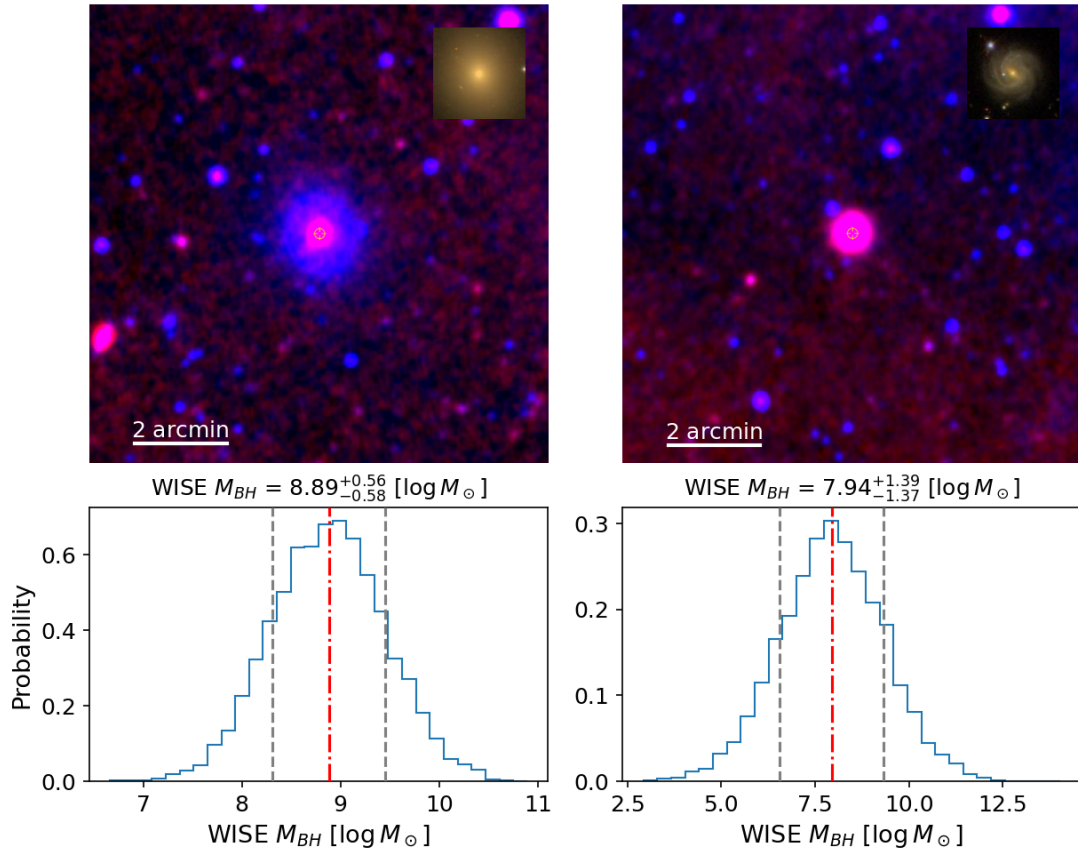
Figure A1.1: Top: WISE two-color images with FOV of 10' of NGC 7626 (left; a HBF galaxy) and NGC 7773 (right; an LBF galaxy): blue represents the W2 band and red the W3 band. The W2−W3 color clearly distinguishes between the HBF and LBF galaxies. In each panel, the SDSS DR16 image of the galaxy is shown as an insert in the upper right corner for reference. Bottom: The corresponding WISE-derived M_{BH} probability distribution provided by our algorithm for each source in the top row. The red vertical line denotes our final (median) M_{BH} value and the dashed vertical lines represent the 1σ of the distribution; the reported values for the lower and upper values of M_{BH}. The HBF galaxy has smaller M_{BH} uncertainties as compared to the LBF galaxy; a trend seen in general for LBF galaxies, e.g., Fig. 3.6.2.
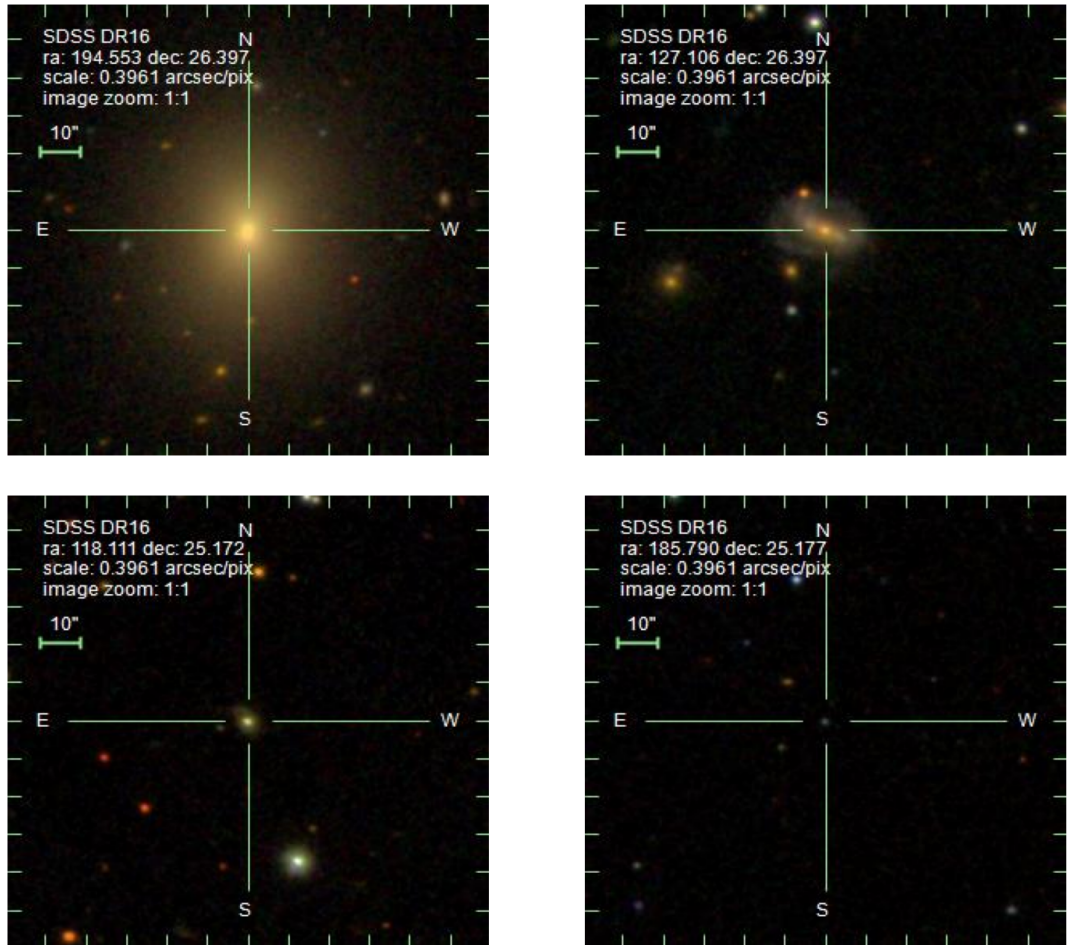
Figure A1.2: SDSS DR16 images of HQS (top) and LQS (bottom) examples. From left to right, at the top are NGC 4849 (HBF) and SDSS J082825.42+262350.4 (LBF). At bottom are SDSS J075226.52+251020.1 and SDSS J122309.61+251036.7, both are have final M_{BH} upper limits.

In contrast, the 2MRS sample shows a relatively smooth and well populated distribution of T_{Type} values (bottom row of Fig. A2.1).

The distributions (median values and 1σ intervals) of W2$-$W3 for each T_{Type} in 2MRS and GZ2 are presented in the top panel of Fig. A2.1. For Dobrycheva, only the medians are shown for comparison. The GZ2 fit shows a similar trend to 2MRS in the range of T_{Type} 0 to 5, covering the same range but with smaller error bars. At the upper end, the fits differ by approximately 0.2 in W2$-$W3, which has a negligible impact on the final M_{Bulge} estimates when comparing the GZ2 fit to 2MRS fit. At the lower end, there is a difference of almost 0.4 in W2$-$W3, leading to significant variations in the estimated B/T. For a source with a W2$-$W3 color of 1, the 2MRS fit gives a $B/T \sim 0.5$ estimate, while the GZ2 fit results in a $B/T \sim 1$, corresponding to a difference of 0.3 dex in the M_{Bulge} estimates, which are the first estimates affected by the B/T value. These systematic changes in fit have significant implications for the final estimates and the overall statistics of the sample. Due to the lack of detail and biased representation, the GZ2 sample and its fit were discarded from our analysis. For the Dobrycheva sample, elliptical galaxies exhibit distinct shifts compared to both 2MRS and GZ2, primarily due to the binarity of the classification used.

Therefore, it is crucial to use a sample that is large enough to accurately discriminate between T_{Type} and then to rely on the trend shown by that specific sample. We defined this 'large enough' sample size to be N, and determined it to be approximately $N \sim 700$ per bin by statistical power analysis, which is a widely used statistical tool for sample size determination in meta-analyses (e.g., Borenstein et al., 2009; Grundler et al., 2022). In statistical power analysis, the three parameters to be set are statistical power, significance threshold, and effect size. The statistical power (P) is often defined as the probability that a study can correctly detect a real effect (i.e., probability of avoiding a Type II error). The significance threshold (α) is defined as the highest level of acceptable risk in terms of incorrectly rejecting a null hypothesis that is actually true (i.e., Type I error probability). Effect size (E_s) is a standardized technique available to measure the expected strength of the results in a study, regardless of the sample size. This E_s can only be calculated for two samples, so in multisample scenarios this has to be calculated for each pair of samples in a predefined order, e.g., if the samples represent an evolution from 0 to 10 in a quantity, the pairs to calculate E_s must
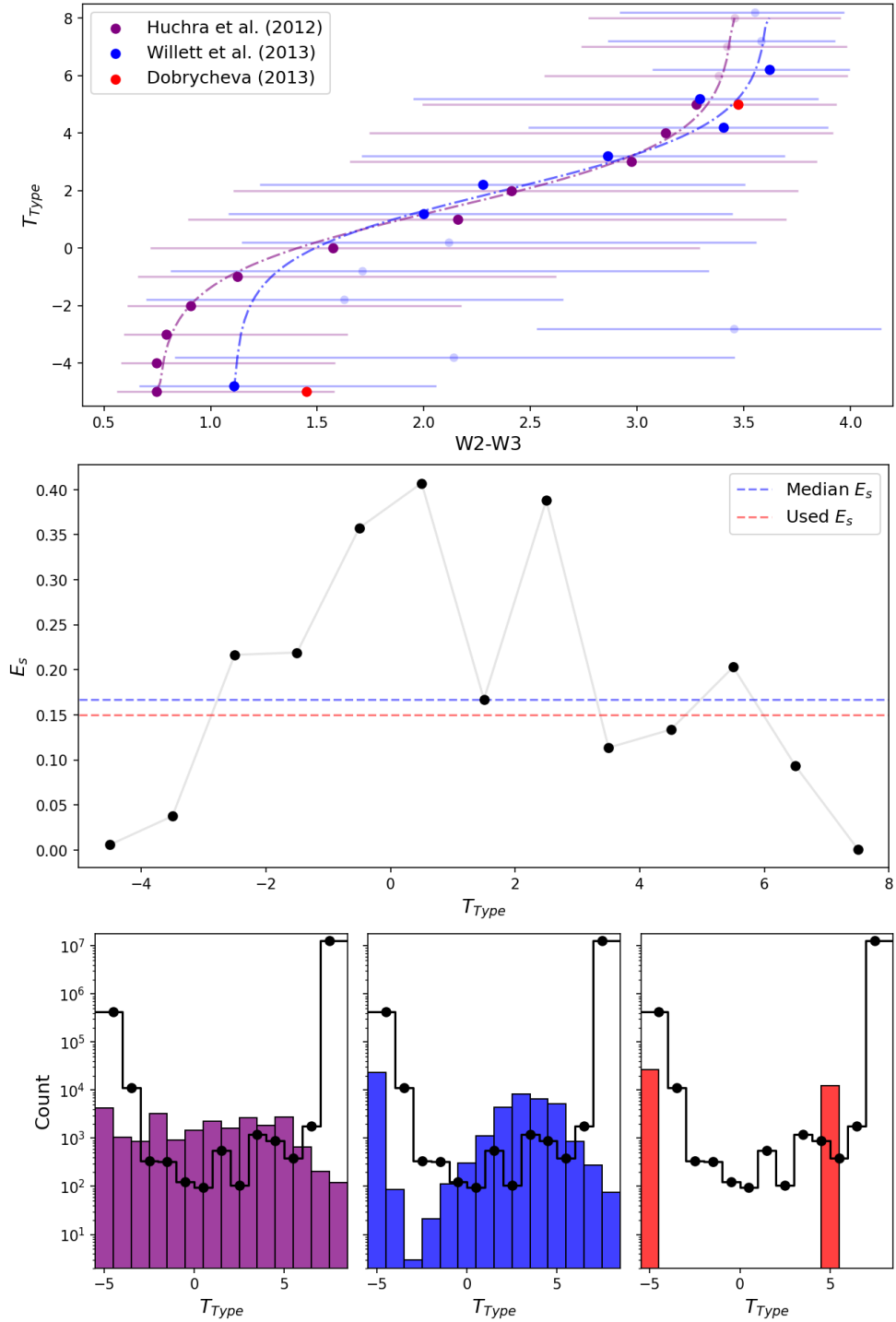
Figure A2.1: Top: As in Fig. 3.3.1 but for all samples described in Appendix A2. Blue dots are slightly shifted in the Y-axis to distinguish between error bars. Colors follow the legend in the top left of the panel. Middle: Effect size (E_s) for every consecutive distribution of W2$-$W3 color, following the order of T_{Type}. The position on the X-axis is the middle value between consecutive T_{Type}. Bottom: T_{Type} distributions of the three samples shown in the top panel are shown in colored histograms of the corresponding color. Black connected dots denote the sample sizes (N) required to establish a distinction between consecutive T_{Type} bins, as derived from the medians of the 2MRS W2$-$W3 distributions in each T_{Type} bin.

be $0-1$, $1-2$, and so on.

For this analysis, we used the median values of the W2−W3 distribution for each T_{Type} value in 2MRS, with parameters; $P = 0.8$, $\alpha = 0.05$ and $E_s = 0.15$. However, the value of E_s varies for each pair or consecutive distribution of W2−W3 following the order of T_{Type}, as shown in the middle plot of Fig. A2.1. The median value of E_s was approximately 0.17, which corresponds to $N \sim 550$. To ensure stricter statistical power, we reduced E_s to 0.15. For the lower and upper ends of T_{Type}, E_s can go as low as 0.001, requiring a sample size of $N \geq 10^7$ to confidently claim that the consecutive distributions are, in fact, two distinct populations and not two samples from the same parent sample. However, the chosen value of E_s is sufficiently strict to clearly discriminate between each distribution of W2−W3 for T_{Type} ranging from -3 to 6.

In the bottom plots of Fig. A2.1 we can see that the required N (black dots) is surpassed in most cases by the three samples (colored histograms), but notoriously larger samples are needed for the most extreme values of T_{Type}. It is clear that the results obtained from the 2MRS statistical power analysis are not directly applicable to limit the use of other samples, but similar median values are expected for the whole population of galaxies and the different T_{Type} between samples, thus needing similar N, independent of the sample used.

We decided to use 2MRS over the other samples tested due to the completeness in the lenticular-spiral regime and because both 2MRS and GZ2 samples showed similar behaviors in the late-type regime, despite that 2MRS is almost 10 times smaller in overall sample size.

A3   Correlations and scatter between WISE2MBH and SDSS samples of stellar mass

As our initial proxy to obtain the final M_{BH} using scaling relations, the estimated M_* from WISE must be accurate compared to estimates obtained with different methods applied to big samples. The C14 method combined with K-corrections from J23 has shown to be more precise when estimating M_{BH}, thus it is recommended to use both approaches together instead of separately. However,

only taking into account the final estimate as a validator of the algorithm can
lead to a bias of the initial estimates, such as M_*.

To test for any bias, we consider three different value added catalogs of M_*
available in SDSS, these being the ones using the methods of; Maraston et al.
(2013) who used SED fitting with passive and star-forming templates with the
Kroupa initial mass function (IMF, Kroupa, 2001), Chen et al. (2012) who used
the principal component analysis (PCA) method in the optical rest-frame spectral
region ($3700-5500$ Å) with two different single stellar population models from
Bruzual and Charlot (2003, BC03) and Maraston and Strömbäck (2011, M11),
and finally Montero-Dorta et al. (2016) who used the flexible stellar population
synthesis (FSPS) method for early and wide formation times.

The correlation and scatter matrices considering all catalogs mentioned above and
WISE2MBH for three different redshift bins are presented in Fig. A3.1.

For correlations, Spearman scores range from $\sim 0.6 - 0.9$ for almost every method
considered in the lowest redshift bin ($z < 0.1$). When looking at a larger bin
($z < 0.3$), all correlation scores decreased, particularly for methods that take into
account completely different scenarios, such as Port_SF and Gra_Early. At the
time of considering the entire redshift range ($z < 0.5$), the scores decreased once
again, now down to 0.34 for the case of WISE2MBH and Gra_Wide. Although
it is true that WISE2MBH showed the worst correlations, the worst scores were
specifically with Gra_Wide and Port_SF, two of the samples that showed the
worst scores in all redshift bins tested (0.62 and 0.47 for bins of $z < 0.1$ and
$z < 0.3$), even compared to other SDSS samples. For the case of WISE2MBH
and Gra_Early, despite having a low score in the entire redshift range, it gets
considerably worse with it, staring at 0.76 and delving into 0.44. In Fig. 3.5.1 it
is clear that there is a systematic shift with redshift that causes the low score. It
is the only sample that shows this behavior.

The results of WISE2MBH have been shown to be the most accurate in terms of
scatter, with the lowest RMSE across all the methods and redshift bins. Compared
to Port_Passive, the RMSE is 0.24 for $z < 0.1$ and even lower to 0.22 when
considering the entire redshift range. When compared to Gra_Early, the RMSE
worsened with redshift, similar to the correlation, which demonstrated a clear
difference between the two models.
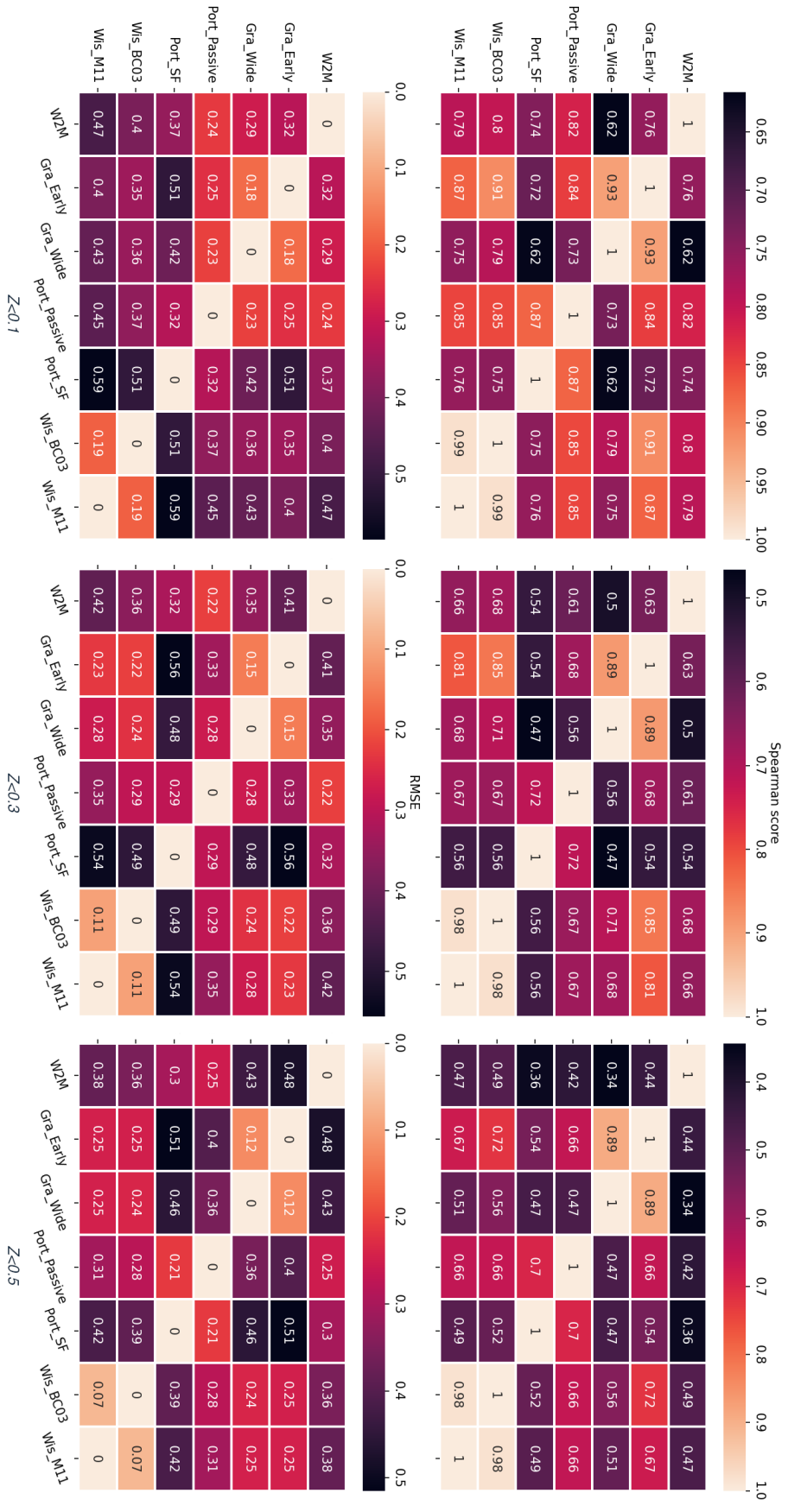
Figure A3.1: Correlation (top) and scatter (bottom) matrices for comparing WISE2MBH M_* estimates with the samples from Montero-Dorta et al. (2016, `Gra_Early` and `Gra_Wide`), Maraston and Strömbäck (2011, `Port_Passive` and `Port_SF`) and Chen et al. (2012, `Wis_BC03` and `Wis_M11`) for three redshift ranges of $z < 0.1$ (left), $z < 0.3$ (middle) and $z < 0.5$ (right). Colorbars at tops of each matrix show the limit values for each case. For the case of scatter, the colorbar is inverted for understanding reasons.

Bibliography

Abraham, R. G., Valdes, F., Yee, H. K. C., and van den Bergh, S. (1994). The Morphologies of Distant Galaxies. I. an Automated Classification System. *ApJ*, 432:75.

Abraham, R. G. and van den Bergh, S. (2001). The Morphological Evolution of Galaxies. *Science*, 293(5533):1273–1278.

Abraham, R. G., van den Bergh, S., Glazebrook, K., Ellis, R. S., Santiago, B. X., Surma, P., and Griffiths, R. E. (1996). The Morphologies of Distant Galaxies. II. Classifications from the Hubble Space Telescope Medium Deep Survey. *ApJS*, 107:1.

Assef, R. J., Stern, D., Noirot, G., Jun, H. D., Cutri, R. M., and Eisenhardt, P. R. M. (2018). The WISE AGN Catalog. *ApJS*, 234(2):23.

Astropy Collaboration, Price-Whelan, A. M., Lim, P. L., Earl, N., Starkman, N., Bradley, L., Shupe, D. L., Patil, A. A., Corrales, L., Brasseur, C. E., Nöthe, M., Donath, A., Tollerud, E., Morris, B. M., Ginsburg, A., Vaher, E., Weaver, B. A., Tocknell, J., Jamieson, W., van Kerkwijk, M. H., Robitaille, T. P., Merry, B., Bachetti, M., Günther, H. M., Aldcroft, T. L., Alvarado-Montes, J. A., Archibald, A. M., Bódi, A., Bapat, S., Barentsen, G., Bazán, J., Biswas, M., Boquien, M., Burke, D. J., Cara, D., Cara, M., Conroy, K. E., Conseil, S., Craig, M. W., Cross, R. M., Cruz, K. L., D'Eugenio, F., Dencheva, N., Devillepoix, H. A. R., Dietrich, J. P., Eigenbrot, A. D., Erben, T., Ferreira, L., Foreman-Mackey, D., Fox, R., Freij, N., Garg, S., Geda, R., Glattly, L., Gondhalekar, Y., Gordon, K. D., Grant, D., Greenfield, P., Groener, A. M., Guest, S., Gurovich, S., Handberg, R., Hart, A., Hatfield-Dodds, Z., Homeier, D., Hosseinzadeh, G., Jenness, T., Jones, C. K., Joseph, P., Kalmbach, J. B., Karamehmetoglu, E., Kałuszyński, M., Kelley, M. S. P., Kern, N., Kerzendorf, W. E., Koch, E. W., Kulumani, S., Lee, A., Ly, C., Ma, Z., MacBride, C., Maljaars, J. M., Muna, D., Murphy, N. A., Norman, H., O'Steen, R., Oman, K. A., Pacifici, C., Pascual, S., Pascual-Granado, J., Patil, R. R., Perren, G. I., Pickering, T. E., Rastogi, T., Roulston, B. R., Ryan, D. F., Rykoff, E. S., Sabater, J., Sakurikar, P., Salgado, J., Sanghi, A., Saunders, N., Savchenko, V., Schwardt, L., Seifert-Eckert, M., Shih, A. Y., Jain, A. S., Shukla, G., Sick, J., Simpson, C., Singanamalla, S., Singer, L. P., Singhal, J., Sinha, M., Sipőcz, B. M., Spitler, L. R., Stansby, D., Streicher, O., Šumak, J., Swinbank, J. D.,

Taranu, D. S., Tewary, N., Tremblay, G. R., Val-Borro, M. d., Van Kooten, S. J., Vasović, Z., Verma, S., de Miranda Cardoso, J. V., Williams, P. K. G., Wilson, T. J., Winkel, B., Wood-Vasey, W. M., Xue, R., Yoachim, P., Zhang, C., Zonca, A., and Astropy Project Contributors (2022). The Astropy Project: Sustaining and Growing a Community-oriented Open-source Project and the Latest Major Release (v5.0) of the Core Package. *ApJ*, 935(2):167.

Bacon, R., Brinchmann, J., Conseil, S., Maseda, M., Nanayakkara, T., Wendt, M., Bacher, R., Mary, D., Weilbacher, P. M., Krajnović, D., Boogaard, L., Bouché, N., Contini, T., Epinat, B., Feltre, A., Guo, Y., Herenz, C., Kollatschny, W., Kusakabe, H., Leclercq, F., Michel-Dansac, L., Pello, R., Richard, J., Roth, M., Salvignol, G., Schaye, J., Steinmetz, M., Tresse, L., Urrutia, T., Verhamme, A., Vitte, E., Wisotzki, L., and Zoutendijk, S. L. (2023). The MUSE Hubble Ultra Deep Field surveys: Data release II. *A&A*, 670:A4.

Bluck, A. F. L., Mendel, J. T., Ellison, S. L., Moreno, J., Simard, L., Patton, D. R., and Starkenburg, E. (2014). Bulge mass is king: the dominant role of the bulge in determining the fraction of passive galaxies in the Sloan Digital Sky Survey. *MNRAS*, 441(1):599–629.

Borenstein, M., Hedges, L. V., Higgins, J. P. T., and Rothstein, H. R. (2009). *Introduction to Meta-Analysis.* John Wiley & Sons.

Broderick, A. E., Narayan, R., Kormendy, J., Perlman, E. S., Rieke, M. J., and Doeleman, S. S. (2015). The Event Horizon of M87. *ApJ*, 805(2):179.

Brown, M. J. I., Moustakas, J., Smith, J. D. T., da Cunha, E., Jarrett, T. H., Imanishi, M., Armus, L., Brandl, B. R., and Peek, J. E. G. (2014). An Atlas of Galaxy Spectral Energy Distributions from the Ultraviolet to the Mid-infrared. *ApJS*, 212(2):18.

Bruzual, G. and Charlot, S. (2003). Stellar population synthesis at the resolution of 2003. *MNRAS*, 344(4):1000–1028.

Caramete, L. I. and Biermann, P. L. (2010). The mass function of nearby black hole candidates. *A&A*, 521:A55.

Casado, J., Ascasibar, Y., Gavilán, M., Terlevich, R., Terlevich, E., Hoyos, C., and Díaz, A. I. (2015). Nature or nurture? Clues from the distribution of specific star formation rates in SDSS galaxies. *MNRAS*, 451(1):888–903.

Chang, Y.-Y., van der Wel, A., da Cunha, E., and Rix, H.-W. (2015). Stellar Masses and Star Formation Rates for 1M Galaxies from SDSS+WISE. *ApJS*, 219(1):8.

Chen, Y.-M., Kauffmann, G., Tremonti, C. A., White, S., Heckman, T. M., Kovač, K., Bundy, K., Chisholm, J., Maraston, C., Schneider, D. P., Bolton, A. S., Weaver, B. A., and Brinkmann, J. (2012). Evolution of the most massive galaxies to z= 0.6 - I. A new method for physical parameter estimation. *MNRAS*, 421(1):314–332.

Cluver, M. E., Jarrett, T. H., Dale, D. A., Smith, J. D. T., August, T., and Brown, M. J. I. (2017). Calibrating Star Formation in WISE Using Total Infrared Luminosity. *ApJ*, 850(1):68.

Cluver, M. E., Jarrett, T. H., Hopkins, A. M., Driver, S. P., Liske, J., Gunawardhana, M. L. P., Taylor, E. N., Robotham, A. S. G., Alpaslan, M., Baldry, I., Brown, M. J. I., Peacock, J. A., Popescu, C. C., Tuffs, R. J., Bauer, A. E., Bland-Hawthorn, J., Colless, M., Holwerda, B. W., Lara-López, M. A., Leschinski, K., López-Sánchez, A. R., Norberg, P., Owers, M. S., Wang, L., and Wilkins, S. M. (2014). Galaxy and Mass Assembly (GAMA): Mid-infrared Properties and Empirical Relations from WISE. *ApJ*, 782(2):90.

Cluver, M. E., Jarrett, T. H., Taylor, E. N., Hopkins, A. M., Brough, S., Casura, S., Holwerda, B. W., Liske, J., Pimbblet, K. A., and Wright, A. H. (2020). Galaxy and Mass Assembly (GAMA): Demonstrating the Power of WISE in the Study of Galaxy Groups to z < 0.1. *ApJ*, 898(1):20.

Croton, D. (2006). Evolution in the black hole mass-bulge mass relation: a theoretical perspective. *MNRAS*, 369:1808–1812.

Cutri, R. M., Wright, E. L., Conrow, T., Fowler, J. W., Eisenhardt, P. R. M., Grillmair, C., Kirkpatrick, J. D., Masci, F., McCallon, H. L., Wheelock, S. L., Fajardo-Acosta, S., Yan, L., Benford, D., Harbut, M., Jarrett, T., Lake, S., Leisawitz, D., Ressler, M. E., Stanford, S. A., Tsai, C. W., Liu, F., Helou, G., Mainzer, A., Gettngs, D., Gonzalez, A., Hoffman, D., Marsh, K. A., Padgett, D., Skrutskie, M. F., Beck, R., Papin, M., and Wittman, M. (2021). VizieR Online Data Catalog: AllWISE Data Release (Cutri+ 2013). *VizieR Online Data Catalog*, page II/328.

Dale, D. A. and Helou, G. (2002). The Infrared Spectral Energy Distribution of Normal Star-forming Galaxies: Calibration at Far-Infrared and Submillimeter Wavelengths. *ApJ*, 576(1):159–168.

Dimauro, P., Daddi, E., Shankar, F., Cattaneo, A., Huertas-Company, M., Bernardi, M., Caro, F., Dupke, R. A., Häußler, B., Evelyn, J., Cortesi, A., Mei, S., and Peletier, R. F. (2022). Coincidence between morphology and star formation activity through cosmic time: the impact of the bulge growth. *MNRAS*, 513:256–281.

Dimauro, P., Huertas-Company, M., Daddi, E., Pérez-González, P. G., Bernardi, M., Barro, G., Buitrago, F., Caro, F., Cattaneo, A., Dominguez-Sánchez, H., Faber, S. M., Häußler, B., Kocevski, D. D., Koekemoer, A. M., Koo, D. C., Lee, C. T., Mei, S., Margalef-Bentabol, B., Primack, J., Rodriguez-Puebla, A., Salvato, M., Shankar, F., and Tuccillo, D. (2018). A catalog of polychromatic bulge-disc decompositions of ∼17.600 galaxies in CANDELS. *MNRAS*, 478(4):5410–5426.

Dobrycheva, D. V. (2013). The New Galaxy Sample from SDSS DR9 at 0.003 ≤ z ≤ 0.1. *Odessa Astronomical Publications*, 26:187.

Doeleman, S., Blackburn, L., Doeleman, S., Dexter, J., Gomez, J. L., Johnson, M. D., Palumbo, D. C., Weintroub, J., Farah, J. R., Fish, V., Loinard, L., Lonsdale, C., Narayanan, G., Patel, N. A., Pesce, D. W., Raymond, A., Tilanus, R., Wielgus, M., Akiyama, K., Bower, G., Broderick, A., Deane, R., Fromm, C. M., Gammie, C., Gold, R., Janssen, M., Kawashima, T., Krichbaum, T., Marrone, D. P., Matthews, L. D., Mizuno, Y., Rezzolla, L., Roelofs, F., Ros, E., Savolainen, T. K., Yuan, F., Zhao, G., Blackburn, L., Doeleman, S., Dexter, J., Gomez, J. L., Johnson, M. D., Palumbo, D. C., Weintroub, J., Farah, J. R., Fish, V., Loinard, L., Lonsdale, C., Narayanan, G., Patel, N. A., Pesce, D. W., Raymond, A., Tilanus, R., Wielgus, M., Akiyama, K., Bower, G., Broderick, A., Deane, R., Fromm, C. M., Gammie, C., Gold, R., Janssen, M., Kawashima, T., Krichbaum, T., Marrone, D. P., Matthews, L. D., Mizuno, Y., Rezzolla, L., Roelofs, F., Ros, E., Savolainen, T. K., Yuan, F., and Zhao, G. (2019). Studying Black Holes on Horizon Scales with VLBI Ground Arrays. *Bulletin of the AAS*, 51(7). https://baas.aas.org/pub/2020n7i256.

Doeleman, S. S., Barrett, J., Blackburn, L., Bouman, K. L., Broderick, A. E., Chaves, R., Fish, V. L., Fitzpatrick, G., Freeman, M., Fuentes, A., Gómez, J. L., Haworth, K., Houston, J., Issaoun, S., Johnson, M. D., Kettenis, M., Loinard, L., Nagar, N., Narayanan, G., Oppenheimer, A., Palumbo, D. C. M., Patel, N., Pesce, D. W., Raymond, A. W., Roelofs, F., Srinivasan, R., Tiede, P., Weintroub, J., and Wielgus, M. (2023). Reference Array and Design Consideration for the Next-Generation Event Horizon Telescope. *Galaxies*, 11(5):107.

Dunlop, J. S., McLure, R. J., Kukula, M. J., Baum, S. A., O'Dea, C. P., and Hughes, D. H. (2003). Quasars, their host galaxies and their central black holes. *MNRAS*, 340(4):1095–1135.

Durbala, A., Finn, R. A., Crone Odekon, M., Haynes, M. P., Koopmann, R. A., and O'Donoghue, A. A. (2020). The ALFALFA-SDSS Galaxy Catalog. *AJ*, 160(6):271.

Edwards, L. O. V., Salinas, M., Stanley, S., Holguin West, P. E., Trierweiler, I., Alpert, H., Coelho, P., Koppaka, S., Tremblay, G. R., Martel, H., and Li, Y. (2020). Clocking the formation of today's largest galaxies: wide field integral spectroscopy of brightest cluster galaxies and their surroundings. *MNRAS*, 491(2):2617–2638.

Evans, I. N., Primini, F. A., Glotfelty, K. J., Anderson, C. S., Bonaventura, N. R., Chen, J. C., Davis, J. E., Doe, S. M., Evans, J. D., Fabbiano, G., Galle, E. C., Gibbs, Danny G., I., Grier, J. D., Hain, R. M., Hall, D. M., Harbo, P. N., He, X. H., Houck, J. C., Karovska, M., Kashyap, V. L., Lauer, J., McCollough, M. L., McDowell, J. C., Miller, J. B., Mitschang, A. W., Morgan, D. L., Mossman, A. E., Nichols, J. S., Nowak, M. A., Plummer, D. A., Refsdal, B. L., Rots, A. H., Siemiginowska, A., Sundheim, B. A., Tibbetts, M. S., Van Stone, D. W., Winkelman, S. L., and Zografou, P. (2010). The Chandra Source Catalog. *ApJS*, 189(1):37–82.

Event Horizon Telescope Collaboration, Akiyama, K., Alberdi, A., Alef, W., Algaba, J. C., Anantua, R., Asada, K., Azulay, R., Bach, U., Baczko, A.-K., Ball, D., Baloković, M., Barrett, J., Bauböck, M., Benson, B. A., Bintley, D., Blackburn, L., Blundell, R., Bouman, K. L., Bower, G. C., Boyce, H., Bremer, M., Brinkerink, C. D., Brissenden, R., Britzen, S., Broderick, A. E., Broguiere, D., Bronzwaer, T., Bustamante, S., Byun, D.-Y., Carlstrom, J. E., Ceccobello, C., Chael, A., Chan, C.-k., Chatterjee, K., Chatterjee, S., Chen, M.-T., Chen, Y., Cheng, X., Cho, I., Christian, P., Conroy, N. S., Conway, J. E., Cordes, J. M., Crawford, T. M., Crew, G. B., Cruz-Osorio, A., Cui, Y., Davelaar, J., Laurentis, M. D., Deane, R., Dempsey, J., Desvignes, G., Dexter, J., Dhruv, V., Doeleman, S. S., Dougal, S., Dzib, S. A., Eatough, R. P., Emami, R., Falcke, H., Farah, J., Fish, V. L., Fomalont, E., Ford, H. A., Fraga-Encinas, R., Freeman, W. T., Friberg, P., Fromm, C. M., Fuentes, A., Galison, P., Gammie, C. F., García, R., Gentaz, O., Georgiev, B., Goddi, C., Gold, R., Gómez-Ruiz, A. I., Gómez, J. L., Gu, M., Gurwell, M., Hada, K., Haggard, D., Haworth, K., Hecht, M. H., Hesper, R., Heumann, D., Ho, L. C., Ho, P., Honma, M., Huang, C.-W. L., Huang, L., Hughes, D. H., Ikeda, S., Impellizzeri, C. M. V., Inoue, M., Issaoun, S., James, D. J., Jannuzi, B. T., Janssen, M., Jeter, B., Jiang, W., Jiménez-Rosales, A., Johnson, M. D., Jorstad, S., Joshi, A. V., Jung, T., Karami, M., Karuppusamy, R., Kawashima, T., Keating, G. K., Kettenis, M., Kim, D.-J., Kim, J.-Y., Kim, J., Kim, J., Kino, M., Koay, J. Y., Kocherlakota, P., Kofuji, Y., Koch, P. M., Koyama, S., Kramer, C., Kramer, M., Krichbaum, T. P., Kuo, C.-Y., Bella, N. L., Lauer, T. R., Lee, D., Lee, S.-S., Leung, P. K., Levis, A., Li, Z., Lico, R., Lindahl, G., Lindqvist, M., Lisakov, M., Liu, J., Liu, K., Liuzzo, E., Lo, W.-P., Lobanov, A. P., Loinard, L., Lonsdale, C. J., Lu, R.-S., Mao, J., Marchili, N., Markoff, S., Marrone, D. P., Marscher, A. P., Martí-Vidal, I., Matsushita, S., Matthews, L. D., Medeiros, L., Menten, K. M., Michalik, D., Mizuno, I., Mizuno, Y., Moran, J. M., Moriyama, K., Moscibrodzka, M., Müller, C., Mus, A., Musoke, G., Myserlis, I., Nadolski, A., Nagai, H., Nagar, N. M., Nakamura, M., Narayan, R., Narayanan, G., Natarajan, I., Nathanail, A., Fuentes, S. N., Neilsen, J., Neri, R., Ni, C., Noutsos, A., Nowak, M. A., Oh, J., Okino, H., Olivares, H., Ortiz-León, G. N., Oyama, T., Özel, F., Palumbo, D. C. M., Paraschos, G. F., Park, J., Parsons, H., Patel, N., Pen, U.-L., Pesce, D. W., Piétu, V., Plambeck, R., PopStefanija, A., Porth, O., Pötzl, F. M., Prather, B., Preciado-López, J. A., Psaltis, D., Pu, H.-Y., Ramakrishnan, V., Rao, R., Rawlings, M. G., Raymond, A. W., Rezzolla, L., Ricarte, A., Ripperda, B., Roelofs, F., Rogers, A., Ros, E., Romero-Cañizales, C., Roshanineshat, A., Rottmann, H., Roy, A. L., Ruiz, I., Ruszczyk, C., Rygl, K. L. J., Sánchez, S., Sánchez-Argüelles, D., Sánchez-Portal, M., Sasada, M., Satapathy, K., Savolainen, T., Schloerb, F. P., Schonfeld, J., Schuster, K.-F., Shao, L., Shen, Z., Small, D., Sohn, B. W., SooHoo, J., Souccar, K., Sun, H., Tazaki, F., Tetarenko, A. J., Tiede, P., Tilanus, R. P. J., Titus, M., Torne, P., Traianou, E., Trent, T., Trippe, S., Turk, M., van Bemmel, I., van Langevelde, H. J., van Rossum, D. R., Vos, J., Wagner, J., Ward-Thompson, D., Wardle, J., Weintroub, J., Wex, N., Wharton,

R., Wielgus, M., Wiik, K., Witzel, G., Wondrak, M. F., Wong, G. N., Wu, Q., Yamaguchi, P., Yoon, D., Young, A., Young, K., Younsi, Z., Yuan, F., Yuan, Y.-F., Zensus, J. A., Zhang, S., Zhao, G.-Y., Zhao, S.-S., Agurto, C., Allardi, A., Amestica, R., Araneda, J. P., Arriagada, O., Berghuis, J. L., Bertarini, A., Berthold, R., Blanchard, J., Brown, K., Cárdenas, M., Cantzler, M., Caro, P., Castillo-Domínguez, E., Chan, T. L., Chang, C.-C., Chang, D. O., Chang, S.-H., Chang, S.-C., Chen, C.-C., Chilson, R., Chuter, T. C., Ciechanowicz, M., Colin-Beltran, E., Coulson, I. M., Crowley, J., Degenaar, N., Dornbusch, S., Durán, C. A., Everett, W. B., Faber, A., Forster, K., Fuchs, M. M., Gale, D. M., Geertsema, G., González, E., Graham, D., Gueth, F., Halverson, N. W., Han, C.-C., Han, K.-C., Hasegawa, Y., Hernández-Rebollar, J. L., Herrera, C., Herrero-Illana, R., Heyminck, S., Hirota, A., Hoge, J., Hostler Schimpf, S. R., Howie, R. E., Huang, Y.-D., Jiang, H., Jinchi, H., John, D., Kimura, K., Klein, T., Kubo, D., Kuroda, J., Kwon, C., Lacasse, R., Laing, R., Leitch, E. M., Li, C.-T., Liu, C.-T., Liu, K.-Y., Lin, L. C. C., Lu, L.-M., Mac-Auliffe, F., Martin-Cocher, P., Matulonis, C., Maute, J. K., Messias, H., Meyer-Zhao, Z., Montaña, A., Montenegro-Montes, F., Montgomerie, W., Moreno Nolasco, M. E., Muders, D., Nishioka, H., Norton, T. J., Nystrom, G., Ogawa, H., Olivares, R., Oshiro, P., Pérez-Beaupuits, J. P., Parra, R., Phillips, N. M., Poirier, M., Pradel, N., Qiu, R., Raffin, P. A., Rahlin, A. S., Ramírez, J., Ressler, S., Reynolds, M., Rodríguez-Montoya, I., Saez-Madain, A. F., Santana, J., Shaw, P., Shirkey, L. E., Silva, K. M., Snow, W., Sousa, D., Sridharan, T. K., Stahm, W., Stark, A. A., Test, J., Torstensson, K., Venegas, P., Walther, C., Wei, T.-S., White, C., Wieching, G., Wijnands, R., Wouterloot, J. G. A., Yu, C.-Y., Yu, W., and Zeballos, M. (2022). First Sagittarius A* Event Horizon Telescope Results. I. The Shadow of the Supermassive Black Hole in the Center of the Milky Way. *ApJ*, 930(2):L12.

Event Horizon Telescope Collaboration, Akiyama, K., Alberdi, A., Alef, W., Asada, K., Azulay, R., Baczko, A.-K., Ball, D., Baloković, M., Barrett, J., Bintley, D., Blackburn, L., Boland, W., Bouman, K. L., Bower, G. C., Bremer, M., Brinkerink, C. D., Brissenden, R., Britzen, S., Broderick, A. E., Broguiere, D., Bronzwaer, T., Byun, D.-Y., Carlstrom, J. E., Chael, A., Chan, C.-k., Chatterjee, S., Chatterjee, K., Chen, M.-T., Chen, Y., Cho, I., Christian, P., Conway, J. E., Cordes, J. M., Crew, G. B., Cui, Y., Davelaar, J., De Laurentis, M., Deane, R., Dempsey, J., Desvignes, G., Dexter, J., Doeleman, S. S., Eatough, R. P., Falcke, H., Fish, V. L., Fomalont, E., Fraga-Encinas, R., Freeman, W. T., Friberg, P., Fromm, C. M., Gómez, J. L., Galison, P., Gammie, C. F., García, R., Gentaz, O., Georgiev, B., Goddi, C., Gold, R., Gu, M., Gurwell, M., Hada, K., Hecht, M. H., Hesper, R., Ho, L. C., Ho, P., Honma, M., Huang, C.-W. L., Huang, L., Hughes, D. H., Ikeda, S., Inoue, M., Issaoun, S., James, D. J., Jannuzi, B. T., Janssen, M., Jeter, B., Jiang, W., Johnson, M. D., Jorstad, S., Jung, T., Karami, M., Karuppusamy, R., Kawashima, T., Keating, G. K., Kettenis, M., Kim, J.-Y., Kim, J., Kim, J., Kino, M., Koay, J. Y., Koch, P. M., Koyama, S., Kramer, M., Kramer, C., Krichbaum, T. P., Kuo, C.-Y., Lauer, T. R., Lee, S.-S., Li, Y.-R., Li, Z., Lindqvist, M., Liu, K., Liuzzo, E.,

Lo, W.-P., Lobanov, A. P., Loinard, L., Lonsdale, C., Lu, R.-S., MacDonald, N. R., Mao, J., Markoff, S., Marrone, D. P., Marscher, A. P., Martí-Vidal, I., Matsushita, S., Matthews, L. D., Medeiros, L., Menten, K. M., Mizuno, Y., Mizuno, I., Moran, J. M., Moriyama, K., Moscibrodzka, M., Müller, C., Nagai, H., Nagar, N. M., Nakamura, M., Narayan, R., Narayanan, G., Natarajan, I., Neri, R., Ni, C., Noutsos, A., Okino, H., Olivares, H., Ortiz-León, G. N., Oyama, T., Özel, F., Palumbo, D. C. M., Patel, N., Pen, U.-L., Pesce, D. W., Piétu, V., Plambeck, R., PopStefanija, A., Porth, O., Prather, B., Preciado-López, J. A., Psaltis, D., Pu, H.-Y., Ramakrishnan, V., Rao, R., Rawlings, M. G., Raymond, A. W., Rezzolla, L., Ripperda, B., Roelofs, F., Rogers, A., Ros, E., Rose, M., Roshanineshat, A., Rottmann, H., Roy, A. L., Ruszczyk, C., Ryan, B. R., Rygl, K. L. J., Sánchez, S., Sánchez-Arguelles, D., Sasada, M., Savolainen, T., Schloerb, F. P., Schuster, K.-F., Shao, L., Shen, Z., Small, D., Sohn, B. W., SooHoo, J., Tazaki, F., Tiede, P., Tilanus, R. P. J., Titus, M., Toma, K., Torne, P., Trent, T., Trippe, S., Tsuda, S., van Bemmel, I., van Langevelde, H. J., van Rossum, D. R., Wagner, J., Wardle, J., Weintroub, J., Wex, N., Wharton, R., Wielgus, M., Wong, G. N., Wu, Q., Young, K., Young, A., Younsi, Z., Yuan, F., Yuan, Y.-F., Zensus, J. A., Zhao, G., Zhao, S.-S., Zhu, Z., Algaba, J.-C., Allardi, A., Amestica, R., Anczarski, J., Bach, U., Baganoff, F. K., Beaudoin, C., Benson, B. A., Berthold, R., Blanchard, J. M., Blundell, R., Bustamente, S., Cappallo, R., Castillo-Domínguez, E., Chang, C.-C., Chang, S.-H., Chang, S.-C., Chen, C.-C., Chilson, R., Chuter, T. C., Córdova Rosado, R., Coulson, I. M., Crawford, T. M., Crowley, J., David, J., Derome, M., Dexter, M., Dornbusch, S., Dudevoir, K. A., Dzib, S. A., Eckart, A., Eckert, C., Erickson, N. R., Everett, W. B., Faber, A., Farah, J. R., Fath, V., Folkers, T. W., Forbes, D. C., Freund, R., Gómez-Ruiz, A. I., Gale, D. M., Gao, F., Geertsema, G., Graham, D. A., Greer, C. H., Grosslein, R., Gueth, F., Haggard, D., Halverson, N. W., Han, C.-C., Han, K.-C., Hao, J., Hasegawa, Y., Henning, J. W., Hernández-Gómez, A., Herrero-Illana, R., Heyminck, S., Hirota, A., Hoge, J., Huang, Y.-D., Impellizzeri, C. M. V., Jiang, H., Kamble, A., Keisler, R., Kimura, K., Kono, Y., Kubo, D., Kuroda, J., Lacasse, R., Laing, R. A., Leitch, E. M., Li, C.-T., Lin, L. C. C., Liu, C.-T., Liu, K.-Y., Lu, L.-M., Marson, R. G., Martin-Cocher, P. L., Massingill, K. D., Matulonis, C., McColl, M. P., McWhirter, S. R., Messias, H., Meyer-Zhao, Z., Michalik, D., Montaña, A., Montgomerie, W., Mora-Klein, M., Muders, D., Nadolski, A., Navarro, S., Neilsen, J., Nguyen, C. H., Nishioka, H., Norton, T., Nowak, M. A., Nystrom, G., Ogawa, H., Oshiro, P., Oyama, T., Parsons, H., Paine, S. N., Peñalver, J., Phillips, N. M., Poirier, M., Pradel, N., Primiani, R. A., Raffin, P. A., Rahlin, A. S., Reiland, G., Risacher, C., Ruiz, I., Sáez-Madaín, A. F., Sassella, R., Schellart, P., Shaw, P., Silva, K. M., Shiokawa, H., Smith, D. R., Snow, W., Souccar, K., Sousa, D., Sridharan, T. K., Srinivasan, R., Stahm, W., Stark, A. A., Story, K., Timmer, S. T., Vertatschitsch, L., Walther, C., Wei, T.-S., Whitehorn, N., Whitney, A. R., Woody, D. P., Wouterloot, J. G. A., Wright, M., Yamaguchi, P., Yu, C.-Y., Zeballos, M., Zhang, S., and Ziurys, L. (2019). First M87 Event Horizon Telescope Results. I. The Shadow of the Supermassive

Black Hole. *ApJ*, 875(1):L1.

Ferrarese, L. and Ford, H. (2005). Supermassive Black Holes in Galactic Nuclei: Past, Present and Future Research. *Space Sci. Rev.*, 116(3-4):523–624.

Fisher, D. and Drory, N. (2011). Demographics of bulge types within 11 mpc and implications for galaxy evolution. *ApJ*, 733:L47.

Flesch, E. (2013). Optical Corrections to the Véron-Cetty and Véron Quasar Catalogue. *PASA*, 30:e004.

Flesch, E. W. (2023). The Million Quasars (Milliquas) Catalogue, v8. *arXiv e-prints*, page arXiv:2308.01505.

Gallo, E. and Sesana, A. (2019). Exploring the Local Black Hole Mass Function below Solar Masses. *ApJ*, 883(1):L18.

Gao, H., Ho, L. C., Barth, A. J., and Li, Z.-Y. (2020). The Carnegie-Irvine Galaxy Survey. IX. Classification of Bulge Types and Statistical Properties of Pseudo Bulges. *ApJS*, 247(1):20.

Ge, X., Gu, Q.-S., Chen, Y.-Y., and Ding, N. (2018). Physical properties variation across the green valley for local galaxies. *arXiv e-prints*, page arXiv:1808.01709.

Genzel, R., Eisenhauer, F., and Gillessen, S. (2010). The Galactic Center massive black hole and nuclear star cluster. *Reviews of Modern Physics*, 82(4):3121–3195.

Graham, A. W. (2016). *Galaxy Bulges and Their Massive Black Holes: A Review*, pages 263–313. Springer International Publishing, Cham.

Greene, J. E., Strader, J., and Ho, L. C. (2020). Intermediate-Mass Black Holes. *ARA&A*, 58:257–312.

Grundler, A., Dazer, M., and Herzig, T. (2022). Statistical power analysis in reliability demonstration testing: The probability of test success. *Applied Sciences*, 12(12).

Gültekin, K., King, A. L., Cackett, E. M., Nyland, K., Miller, J. M., Di Matteo, T., Markoff, S., and Rupen, M. P. (2019). The Fundamental Plane of Black Hole Accretion and Its Use as a Black Hole-Mass Estimator. *ApJ*, 871(1):80.

Guo, S., Qi, Z., Liao, S., Cao, Z., Lattanzi, M. G., Bucciarelli, B., Tang, Z., and Yan, Q.-Z. (2018). Identifying quasars with astrometric and mid-infrared methods from APOP and ALLWISE. *A&A*, 618:A144.

Häring, N. and Rix, H.-W. (2004). On the Black Hole Mass-Bulge Mass Relation. *ApJ*, 604(2):L89–L92.

Harris, C. R., Millman, K. J., van der Walt, S. J., Gommers, R., Virtanen, P., Cournapeau, D., Wieser, E., Taylor, J., Berg, S., Smith, N. J., Kern, R., Picus, M., Hoyer, S., van Kerkwijk, M. H., Brett, M., Haldane, A., del Río, J. F., Wiebe, M., Peterson, P., Gérard-Marchant, P., Sheppard, K., Reddy,

T., Weckesser, W., Abbasi, H., Gohlke, C., and Oliphant, T. E. (2020). Array programming with NumPy. *Nature*, 585(7825):357–362.

Hickox, R. C. and Alexander, D. M. (2018). Obscured Active Galactic Nuclei. *ARA&A*, 56:625–671.

Huchra, J. P., Macri, L. M., Masters, K. L., Jarrett, T. H., Berlind, P., Calkins, M., Crook, A. C., Cutri, R., Erdoğdu, P., Falco, E., George, T., Hutcheson, C. M., Lahav, O., Mader, J., Mink, J. D., Martimbeau, N., Schneider, S., Skrutskie, M., Tokarz, S., and Westover, M. (2012). The 2MASS Redshift Survey—Description and Data Release. *ApJS*, 199(2):26.

Hunter, J. D. (2007). Matplotlib: A 2d graphics environment. *Computing in Science & Engineering*, 9(3):90–95.

Hviding, R. E., Hainline, K. N., Rieke, M., Juneau, S., Lyu, J., and Pucha, R. (2022). A New Infrared Criterion for Selecting Active Galactic Nuclei to Lower Luminosities. *AJ*, 163(5):224.

Inayoshi, K., Visbal, E., and Haiman, Z. (2020). The Assembly of the First Massive Black Holes. *ARA&A*, 58:27–97.

Jarrett, T. H., Chester, T., Cutri, R., Schneider, S., Skrutskie, M., and Huchra, J. P. (2000). 2MASS Extended Source Catalog: Overview and Algorithms. *AJ*, 119(5):2498–2531.

Jarrett, T. H., Cluver, M. E., Brown, M. J. I., Dale, D. A., Tsai, C. W., and Masci, F. (2019). The WISE Extended Source Catalog (WXSC). I. The 100 Largest Galaxies. *ApJS*, 245(2):25.

Jarrett, T. H., Cluver, M. E., Taylor, E. N., Bellstedt, S., Robotham, A. S. G., and Yao, H. F. M. (2023). A New Wide-field Infrared Survey Explorer Calibration of Stellar Mass. *ApJ*, 946(2):95.

Jarrett, T. H., Cohen, M., Masci, F., Wright, E., Stern, D., Benford, D., Blain, A., Carey, S., Cutri, R. M., Eisenhardt, P., Lonsdale, C., Mainzer, A., Marsh, K., Padgett, D., Petty, S., Ressler, M., Skrutskie, M., Stanford, S., Surace, J., Tsai, C. W., Wheelock, S., and Yan, D. L. (2011). The Spitzer-WISE Survey of the Ecliptic Poles. *ApJ*, 735(2):112.

Jarrett, T. H., Masci, F., Tsai, C. W., Petty, S., Cluver, M. E., Assef, R. J., Benford, D., Blain, A., Bridge, C., Donoso, E., Eisenhardt, P., Koribalski, B., Lake, S., Neill, J. D., Seibert, M., Sheth, K., Stanford, S., and Wright, E. (2013). Extending the Nearby Galaxy Heritage with WISE: First Results from the WISE Enhanced Resolution Galaxy Atlas. *AJ*, 145(1):6.

Jarrett, T. H., Masci, F. J., Tsai, C., Petty, S., Cluver, M., Assef, R. J., Benford, D. J., Blain, A. W., Bridge, C., Donoso, E., Eisenhardt, P., Koribalski, B. S., Lake, S. E., Neill, J. D., Seibert, M., Sheth, K., Stanford, S. A., and Wright, E. L. (2012). Extending the nearby galaxy heritage withwise: first results from thewiseenhanced resolution galaxy atlas. *AJ*, 145:6.

Johnson, M. D., Akiyama, K., Blackburn, L., Bouman, K. L., Broderick, A. E., Cardoso, V., Fender, R. P., Fromm, C. M., Galison, P., Gómez, J. L., Haggard, D., Lister, M. L., Lobanov, A. P., Markoff, S., Narayan, R., Natarajan, P., Nichols, T., Pesce, D. W., Younsi, Z., Chael, A., Chatterjee, K., Chaves, R., Doboszewski, J., Dodson, R., Doeleman, S. S., Elder, J., Fitzpatrick, G., Haworth, K., Houston, J., Issaoun, S., Kovalev, Y. Y., Levis, A., Lico, R., Marcoci, A., Martens, N. C. M., Nagar, N. M., Oppenheimer, A., Palumbo, D. C. M., Ricarte, A., Rioja, M. J., Roelofs, F., Thresher, A. C., Tiede, P., Weintroub, J., and Wielgus, M. (2023). Key science goals for the next-generation event horizon telescope. *Galaxies*, 11(3).

Karademir, G. S., Taylor, E. N., Blake, C., Cluver, M. E., Jarrett, T. H., and Triani, D. P. (2023). Measurement of the evolving galaxy luminosity and mass function using clustering-based redshift inference. *MNRAS*, 522(3):3693–3709.

Kettlety, T., Hesling, J., Phillipps, S., Bremer, M. N., Cluver, M. E., Taylor, E. N., Bland-Hawthorn, J., Brough, S., De Propris, R., Driver, S. P., Holwerda, B. W., Kelvin, L. S., Sutherland, W., and Wright, A. H. (2018). Galaxy and mass assembly (GAMA): the consistency of GAMA and WISE derived mass-to-light ratios. *MNRAS*, 473(1):776–783.

Kollmeier, J. A., Zasowski, G., Rix, H.-W., Johns, M., Anderson, S. F., Drory, N., Johnson, J. A., Pogge, R. W., Bird, J. C., Blanc, G. A., Brownstein, J. R., Crane, J. D., De Lee, N. M., Klaene, M. A., Kreckel, K., MacDonald, N., Merloni, A., Ness, M. K., O'Brien, T., Sanchez-Gallego, J. R., Sayres, C. C., Shen, Y., Thakar, A. R., Tkachenko, A., Aerts, C., Blanton, M. R., Eisenstein, D. J., Holtzman, J. A., Maoz, D., Nandra, K., Rockosi, C., Weinberg, D. H., Bovy, J., Casey, A. R., Chaname, J., Clerc, N., Conroy, C., Eracleous, M., Gänsicke, B. T., Hekker, S., Horne, K., Kauffmann, J., McQuinn, K. B. W., Pellegrini, E. W., Schinnerer, E., Schlafly, E. F., Schwope, A. D., Seibert, M., Teske, J. K., and van Saders, J. L. (2017). SDSS-V: Pioneering Panoptic Spectroscopy. *arXiv e-prints*, page arXiv:1711.03234.

Kong, M. and Ho, L. C. (2018). The Black Hole Masses and Eddington Ratios of Type 2 Quasars. *ApJ*, 859(2):116.

Kormendy, J. and Ho, L. C. (2013). Coevolution (Or Not) of Supermassive Black Holes and Host Galaxies. *ARA&A*, 51(1):511–653.

Koyama, S., Koyama, Y., Yamashita, T., Hayashi, M., Matsuhara, H., Namiki, S., Suzuki, T., Fukagawa, N., Kodama, T., Lin, L., Morokuma-Matsui, K., Shimakawa, R., and Tanaka, I. (2019). Do galaxy morphologies really affect the efficiency of star formation during the phase of galaxy transition? *ApJ*, 874:142.

Kroupa, P. (2001). On the variation of the initial mass function. *MNRAS*, 322(2):231–246.

Kuhn, L., Shubat, M., and Barmby, P. (2022). Comparing NED and SIMBAD classifications across the contents of nearby galaxies. *MNRAS*, 515(1):807–816.

Kurcz, A., Bilicki, M., Solarz, A., Krupa, M., Pollo, A., and Małek, K. (2016). Towards automatic classification of all WISE sources. *A&A*, 592:A25.

Laurikainen, E., Salo, H., Buta, R., and Knapen, J. (2007). Properties of bars and bulges in the hubble sequence. *MNRAS*, 381:401–417.

Lavaux, G. and Hudson, M. J. (2011). The 2M++ galaxy redshift catalogue. *MNRAS*, 416(4):2840–2856.

Lee, G.-H., Hwang, H. S., Sohn, J., and Lee, M. G. (2017). The Fastest Galaxy Evolution in an Unbiased Compact Group Sample with WISE. *ApJ*, 835(2):280.

Lee, J. C., Hwang, H. S., and Ko, J. (2013). The Calibration of Star Formation Rate Indicators for WISE 22 μm-Selected Galaxies in the Sloan Digital Sky Survey. *ApJ*, 774(1):62.

Li, F., Wang, J., Xu, F., Kong, X., Chen, X., Lin, Z., and Wang, S. (2023). The Interstellar Medium Scaling Relations Using Inner H I and an Application of Estimating Dust Mass. *ApJ*, 950(2):84.

Li, J. and Shen, Y. (2023). Constraining AGN Torus Sizes with Optical and Mid-infrared Ensemble Structure Functions. *ApJ*, 950(2):122.

Liepold, E. R., Ma, C.-P., and Walsh, J. L. (2023). Keck Integral-field Spectroscopy of M87 Reveals an Intrinsically Triaxial Galaxy and a Revised Black Hole Mass. *ApJ*, 945(2):L35.

Liu, D., Lang, P., Magnelli, B., Schinnerer, E., Leslie, S., Fudamoto, Y., Bondi, M., Groves, B., Jiménez-Andrade, E., Harrington, K., Karim, A., Oesch, P. A., Sargent, M., Vardoulaki, E., Bădescu, T., Moser, L., Bertoldi, F., Battisti, A., da Cunha, E., Zavala, J., Vaccari, M., Davidzon, I., Riechers, D., and Aravena, M. (2019). Automated Mining of the ALMA Archive in the COSMOS Field (A³COSMOS). I. Robust ALMA Continuum Photometry Catalogs and Stellar Mass and Star Formation Properties for $\sim$700 Galaxies at z = 0.5-6. *ApJS*, 244(2):40.

Liu, T., Buchner, J., Nandra, K., Merloni, A., Dwelly, T., Sanders, J. S., Salvato, M., Arcodia, R., Brusa, M., Wolf, J., Georgakakis, A., Boller, T., Krumpe, M., Lamer, G., Waddell, S., Urrutia, T., Schwope, A., Robrade, J., Wilms, J., Dauser, T., Comparat, J., Toba, Y., Ichikawa, K., Iwasawa, K., Shen, Y., and Medel, H. I. (2022). The eROSITA Final Equatorial-Depth Survey (eFEDS). The AGN catalog and its X-ray spectral properties. *A&A*, 661:A5.

López, I. E., Brusa, M., Bonoli, S., Shankar, F., Acharya, N., Laloux, B., Dolag, K., Georgakakis, A., Lapi, A., Ramos Almeida, C., Salvato, M., Chaves-Montero, J., Coelho, P., Díaz-García, L. A., Fernández-Ontiveros, J. A., Hernán-Caballero, A., González Delgado, R. M., Marquez, I., Pović, M., Soria, R., Queiroz, C., Rahna, P. T., Abramo, R., Alcaniz, J., Benitez, N., Carneiro, S., Cenarro, J., Cristóbal-Hornillos, D., Dupke, R., Ederoclite, A., López-Sanjuan, C., Marín-Franch, A., Mendes de Oliveira, C., Moles, M., Sodré, L., J., Taylor, K., Varela,

J., and Ramió, H. V. (2023). The miniJPAS survey: AGN and host galaxy coevolution of X-ray-selected sources. *A&A*, 672:A137.

Lyu, J. and Rieke, G. H. (2022). Polar Dust Emission in Quasar IR SEDs and Its Correlation with Narrow-line Regions. *ApJ*, 940(2):L31.

Lyu, J., Rieke, G. H., and Smith, P. S. (2019). Mid-IR Variability and Dust Reverberation Mapping of Low-z Quasars. I. Data, Methods, and Basic Results. *ApJ*, 886(1):33.

Mainzer, A., Bauer, J., Grav, T., Masiero, J., Cutri, R. M., Dailey, J., Eisenhardt, P., McMillan, R. S., Wright, E., Walker, R., Jedicke, R., Spahr, T., Tholen, D., Alles, R., Beck, R., Brandenburg, H., Conrow, T., Evans, T., Fowler, J., Jarrett, T., Marsh, K., Masci, F., McCallon, H., Wheelock, S., Wittman, M., Wyatt, P., DeBaun, E., Elliott, G., Elsbury, D., Gautier, T., I., Gomillion, S., Leisawitz, D., Maleszewski, C., Micheli, M., and Wilkins, A. (2011). Preliminary Results from NEOWISE: An Enhancement to the Wide-field Infrared Survey Explorer for Solar System Science. *ApJ*, 731(1):53.

Makarov, D., Prugniel, P., Terekhova, N., Courtois, H., and Vauglin, I. (2014). HyperLEDA. III. The catalogue of extragalactic distances. *A&A*, 570:A13.

Maraston, C., Pforr, J., Henriques, B. M., Thomas, D., Wake, D., Brownstein, J. R., Capozzi, D., Tinker, J., Bundy, K., Skibba, R. A., Beifiori, A., Nichol, R. C., Edmondson, E., Schneider, D. P., Chen, Y., Masters, K. L., Steele, O., Bolton, A. S., York, D. G., Weaver, B. A., Higgs, T., Bizyaev, D., Brewington, H., Malanushenko, E., Malanushenko, V., Snedden, S., Oravetz, D., Pan, K., Shelden, A., and Simmons, A. (2013). Stellar masses of SDSS-III/BOSS galaxies at z ∼ 0.5 and constraints to galaxy formation models. *MNRAS*, 435(4):2764–2792.

Maraston, C. and Strömbäck, G. (2011). Stellar population models at high spectral resolution. *MNRAS*, 418(4):2785–2811.

Massaro, E., Maselli, A., Leto, C., Marchegiani, P., Perri, M., Giommi, P., and Piranomonte, S. (2016). VizieR Online Data Catalog: The Roma BZCAT - 5th edition (Massaro+, 2015). *VizieR Online Data Catalog*, page VII/274.

Mateos, S., Alonso-Herrero, A., Carrera, F. J., Blain, A., Watson, M. G., Barcons, X., Braito, V., Severgnini, P., Donley, J. L., and Stern, D. (2012). Using the Bright Ultrahard XMM-Newton survey to define an IR selection of luminous AGN based on WISE colours. *MNRAS*, 426(4):3271–3281.

Mei, S., Hatch, N. A., Amodeo, S., Afanasiev, A. V., De Breuck, C., Stern, D., Cooke, E. A., Gonzalez, A. H., Noirot, G., Rettura, A., Seymour, N., Stanford, S. A., Vernet, J., and Wylezalek, D. (2023). Morphology-density relation, quenching, and mergers in CARLA clusters and protoclusters at 1.4 < z < 2.8. *A&A*, 670:A58.

Meidt, S. E., Schinnerer, E., Knapen, J. H., Bosma, A., Athanassoula, E., Sheth,

K., Buta, R. J., Zaritsky, D., Laurikainen, E., Elmegreen, D., Elmegreen, B. G., Gadotti, D. A., Salo, H., Regan, M., Ho, L. C., Madore, B. F., Hinz, J. L., Skibba, R. A., Gil de Paz, A., Muñoz-Mateos, J.-C., Menéndez-Delmestre, K., Seibert, M., Kim, T., Mizusawa, T., Laine, J., and Comerón, S. (2012). Reconstructing the Stellar Mass Distributions of Galaxies Using S^{4}G IRAC 3.6 and 4.5 μm Images. I. Correcting for Contamination by Polycyclic Aromatic Hydrocarbons, Hot Dust, and Intermediate-age Stars. *ApJ*, 744(1):17.

Mendel, J. T., Simard, L., Palmer, M., Ellison, S. L., and Patton, D. R. (2014). A Catalog of Bulge, Disk, and Total Stellar Mass Estimates for the Sloan Digital Sky Survey. *ApJS*, 210(1):3.

Mezcua, M., Hlavacek-Larrondo, J., Lucey, J. R., Hogan, M. T., Edge, A. C., and McNamara, B. R. (2018). The most massive black holes on the Fundamental Plane of black hole accretion. *MNRAS*, 474(1):1342–1360.

Michalik, D. and Lindegren, L. (2016). Quasars can be used to verify the parallax zero-point of the Tycho-Gaia Astrometric Solution. *A&A*, 586:A26.

Montero-Dorta, A. D., Bolton, A. S., Brownstein, J. R., Swanson, M., Dawson, K., Prada, F., Eisenstein, D., Maraston, C., Thomas, D., Comparat, J., Chuang, C.-H., McBride, C. K., Favole, G., Guo, H., Rodríguez-Torres, S., and Schneider, D. P. (2016). The high-mass end of the red sequence at z $\sim$ 0.55 from SDSS-III/BOSS: completeness, bimodality and luminosity function. *MNRAS*, 461(2):1131–1153.

Morell, D. F., Ribeiro, A. L. B., de Carvalho, R. R., Rembold, S. B., Lopes, P. A. A., and Costa, A. P. (2020). Classification and evolution of galaxies according to the dynamical state of host clusters and galaxy luminosities. *MNRAS*, 494(3):3317–3327.

Netzer, H. (2015). Revisiting the Unified Model of Active Galactic Nuclei. *ARA&A*, 53:365–408.

Noda, H., Kawamuro, T., Kokubo, M., and Minezaki, T. (2020). Dust reverberation mapping of type 2 AGN NGC 2110 realized with X-ray and 3-5 μm IR monitoring. *MNRAS*, 495(3):2921–2929.

Norris, M. A., Meidt, S., Van de Ven, G., Schinnerer, E., Groves, B., and Querejeta, M. (2014). Being WISE. I. Validating Stellar Population Models and M$_{sstarf}$/L Ratios at 3.4 and 4.6 μm. *ApJ*, 797(1):55.

Padovani, P., Alexander, D. M., Assef, R. J., De Marco, B., Giommi, P., Hickox, R. C., Richards, G. T., Smolčić, V., Hatziminaoglou, E., Mainieri, V., and Salvato, M. (2017). Active galactic nuclei: what's in a name? *A&A Rev.*, 25(1):2.

Pahre, M. A., Ashby, M. L. N., Fazio, G. G., and Willner, S. P. (2004). Mid-Infrared Galaxy Morphology along the Hubble Sequence. *ApJS*, 154(1):235–241.

Pesce, D. W., Palumbo, D. C. M., Narayan, R., Blackburn, L., Doeleman, S. S., Johnson, M. D., Ma, C.-P., Nagar, N. M., Natarajan, P., and Ricarte, A. (2021). Toward Determining the Number of Observable Supermassive Black Hole Shadows. *ApJ*, 923(2):260.

Pesce, D. W., Palumbo, D. C. M., Ricarte, A., Broderick, A. E., Johnson, M. D., Nagar, N. M., Natarajan, P., and Gómez, J. L. (2022). Expectations for horizon-scale supermassive black hole population studies with the ngeht. *Galaxies*, 10(6).

Planck Collaboration, Aghanim, N., Akrami, Y., Ashdown, M., Aumont, J., Baccigalupi, C., Ballardini, M., Banday, A. J., Barreiro, R. B., Bartolo, N., Basak, S., Battye, R., Benabed, K., Bernard, J. P., Bersanelli, M., Bielewicz, P., Bock, J. J., Bond, J. R., Borrill, J., Bouchet, F. R., Boulanger, F., Bucher, M., Burigana, C., Butler, R. C., Calabrese, E., Cardoso, J. F., Carron, J., Challinor, A., Chiang, H. C., Chluba, J., Colombo, L. P. L., Combet, C., Contreras, D., Crill, B. P., Cuttaia, F., de Bernardis, P., de Zotti, G., Delabrouille, J., Delouis, J. M., Di Valentino, E., Diego, J. M., Doré, O., Douspis, M., Ducout, A., Dupac, X., Dusini, S., Efstathiou, G., Elsner, F., Enßlin, T. A., Eriksen, H. K., Fantaye, Y., Farhang, M., Fergusson, J., Fernandez-Cobos, R., Finelli, F., Forastieri, F., Frailis, M., Fraisse, A. A., Franceschi, E., Frolov, A., Galeotta, S., Galli, S., Ganga, K., Génova-Santos, R. T., Gerbino, M., Ghosh, T., González-Nuevo, J., Górski, K. M., Gratton, S., Gruppuso, A., Gudmundsson, J. E., Hamann, J., Handley, W., Hansen, F. K., Herranz, D., Hildebrandt, S. R., Hivon, E., Huang, Z., Jaffe, A. H., Jones, W. C., Karakci, A., Keihänen, E., Keskitalo, R., Kiiveri, K., Kim, J., Kisner, T. S., Knox, L., Krachmalnicoff, N., Kunz, M., Kurki-Suonio, H., Lagache, G., Lamarre, J. M., Lasenby, A., Lattanzi, M., Lawrence, C. R., Le Jeune, M., Lemos, P., Lesgourgues, J., Levrier, F., Lewis, A., Liguori, M., Lilje, P. B., Lilley, M., Lindholm, V., López-Caniego, M., Lubin, P. M., Ma, Y. Z., Macías-Pérez, J. F., Maggio, G., Maino, D., Mandolesi, N., Mangilli, A., Marcos-Caballero, A., Maris, M., Martin, P. G., Martinelli, M., Martínez-González, E., Matarrese, S., Mauri, N., McEwen, J. D., Meinhold, P. R., Melchiorri, A., Mennella, A., Migliaccio, M., Millea, M., Mitra, S., Miville-Deschênes, M. A., Molinari, D., Montier, L., Morgante, G., Moss, A., Natoli, P., Nørgaard-Nielsen, H. U., Pagano, L., Paoletti, D., Partridge, B., Patanchon, G., Peiris, H. V., Perrotta, F., Pettorino, V., Piacentini, F., Polastri, L., Polenta, G., Puget, J. L., Rachen, J. P., Reinecke, M., Remazeilles, M., Renzi, A., Rocha, G., Rosset, C., Roudier, G., Rubiño-Martín, J. A., Ruiz-Granados, B., Salvati, L., Sandri, M., Savelainen, M., Scott, D., Shellard, E. P. S., Sirignano, C., Sirri, G., Spencer, L. D., Sunyaev, R., Suur-Uski, A. S., Tauber, J. A., Tavagnacco, D., Tenti, M., Toffolatti, L., Tomasi, M., Trombetti, T., Valenziano, L., Valiviita, J., Van Tent, B., Vibert, L., Vielva, P., Villa, F., Vittorio, N., Wandelt, B. D., Wehus, I. K., White, M., White, S. D. M., Zacchei, A., and Zonca, A. (2020). Planck 2018 results. VI. Cosmological parameters. *A&A*, 641:A6.

Poitevineau, R., Castignani, G., and Combes, F. (2023). Black hole and galaxy co-evolution in radio-loud active galactic nuclei at z ∼ 0.3-4. *A&A*, 672:A164.

Polletta, M., Weedman, D., Hönig, S., Lonsdale, C. J., Smith, H. E., and Houck, J. (2008). Obscuration in Extremely Luminous Quasars. *ApJ*, 675(2):960–984.

Quilley, L. and de Lapparent, V. (2022). Aging of galaxies along the morphological sequence, marked by bulge growth and disk quenching. *A&A*, 666:A170.

Quilley, L. and de Lapparent, V. (2023). Tailoring galaxies: size-luminosity-surface brightness relations of bulges and disks along the morphological sequence. *arXiv e-prints*, page arXiv:2305.02069.

Ramakrishnan, V., Nagar, N., Arratia, V., Hernández-Yévenes, J., Pesce, D. W., Nair, D. G., Bandyopadhyay, B., Medina-Porcile, C., Krichbaum, T. P., Doeleman, S., Ricarte, A., Fish, V. L., Blackburn, L., Falcke, H., Bower, G., and Natarajan, P. (2023). Event horizon and environs (ether): A curated database for eht and ngeht targets and science. *Galaxies*, 11(1).

Reback, J., jbrockmendel, McKinney, W., Van den Bossche, J., Augspurger, T., Roeschke, M., Hawkins, S., Cloud, P., gfyoung, Sinhrks, Hoefler, P., Klein, A., Petersen, T., Tratner, J., She, C., Ayd, W., Naveh, S., Darbyshire, J., Garcia, M., Shadrach, R., Schendel, J., Hayden, A., Saxton, D., Gorelli, M. E., Li, F., Zeitlin, M., Jancauskas, V., McMaster, A., Wörtwein, T., and Battiston, P. (2022). pandas-dev/pandas: Pandas 1.4.2. Zenodo.

Runge, J. and Walker, S. A. (2021). Probing within the Bondi radius of the ultramassive black hole in NGC 1600. *MNRAS*, 502(4):5487–5494.

Sadler, E. M., Ekers, R. D., Mahony, E. K., Mauch, T., and Murphy, T. (2014). The local radio-galaxy population at 20 GHz. *MNRAS*, 438(1):796–824.

Saglia, R. P., Opitsch, M., Erwin, P., Thomas, J., Beifiori, A., Fabricius, M., Mazzalay, X., Nowak, N., Rusli, S. P., and Bender, R. (2016). The SINFONI Black Hole Survey: The Black Hole Fundamental Plane Revisited and the Paths of (Co)evolution of Supermassive Black Holes and Bulges. *ApJ*, 818(1):47.

Schutte, Z., Reines, A. E., and Greene, J. E. (2019). The Black Hole-Bulge Mass Relation Including Dwarf Galaxies Hosting Active Galactic Nuclei. *ApJ*, 887(2):245.

Seabold, S. and Perktold, J. (2010). statsmodels: Econometric and statistical modeling with python. In *9th Python in Science Conference.*

Shankar, F., Bernardi, M., Sheth, R. K., Ferrarese, L., Graham, A. W., Savorgnan, G., Allevato, V., Marconi, A., Läsker, R., and Lapi, A. (2016). Selection bias in dynamically measured supermassive black hole samples: its consequences and the quest for the most fundamental relation. *MNRAS*, 460(3):3119–3142.

Shankar, F., Weinberg, D. H., and Miralda-Escudé, J. (2009). Self-Consistent Models of the AGN and Black Hole Populations: Duty Cycles, Accretion Rates, and the Mean Radiative Efficiency. *ApJ*, 690(1):20–41.

Singh, S., Ashby, M. L. N., Vig, S., Ghosh, S. K., Jarrett, T., Crawford, T. M.,

Malkan, M. A., Archipley, M., and Vieira, J. D. (2021). The cold dust content of the nearby galaxies IC 5325, NGC 7496, NGC 7590, and NGC 7599. *MNRAS*, 504(3):4143–4159.

Sofue, Y. (2016). Rotation curve decomposition for size-mass relations of bulge, disk, and dark halo components in spiral galaxies. *PASJ*, 68(1):2.

Stern, D., Assef, R. J., Benford, D. J., Blain, A., Cutri, R., Dey, A., Eisenhardt, P., Griffith, R. L., Jarrett, T. H., Lake, S., Masci, F., Petty, S., Stanford, S. A., Tsai, C.-W., Wright, E. L., Yan, L., Harrison, F., and Madsen, K. (2012). Mid-infrared Selection of Active Galactic Nuclei with the Wide-Field Infrared Survey Explorer. I. Characterizing WISE-selected Active Galactic Nuclei in COSMOS. *ApJ*, 753(1):30.

Suh, K.-W. (2021). A New Catalog of Asymptotic Giant Branch Stars in Our Galaxy. *ApJS*, 256(2):43.

Tacconi, L. J., Neri, R., Genzel, R., Combes, F., Bolatto, A., Cooper, M. C., Wuyts, S., Bournaud, F., Burkert, A., Comerford, J., Cox, P., Davis, M., Förster Schreiber, N. M., García-Burillo, S., Gracia-Carpio, J., Lutz, D., Naab, T., Newman, S., Omont, A., Saintonge, A., Shapiro Griffin, K., Shapley, A., Sternberg, A., and Weiner, B. (2013). Phibss: Molecular Gas Content and Scaling Relations in z ⌣1-3 Massive, Main-sequence Star-forming Galaxies. *ApJ*, 768(1):74.

Taylor, M. B. (2005). TOPCAT & STIL: Starlink Table/VOTable Processing Software. In Shopbell, P., Britton, M., and Ebert, R., editors, *Astronomical Data Analysis Software and Systems XIV*, volume 347 of *Astronomical Society of the Pacific Conference Series*, page 29.

Thater, S., Krajnović, D., Cappellari, M., Davis, T. A., de Zeeuw, P. T., McDermid, R. M., and Sarzi, M. (2019). Six new supermassive black hole mass determinations from adaptive-optics assisted SINFONI observations. *A&A*, 625:A62.

Tsai, C.-W., Eisenhardt, P. R. M., Wu, J., Stern, D., Assef, R. J., Blain, A. W., Bridge, C. R., Benford, D. J., Cutri, R. M., Griffith, R. L., Jarrett, T. H., Lonsdale, C. J., Masci, F. J., Moustakas, L. A., Petty, S. M., Sayers, J., Stanford, S. A., Wright, E. L., Yan, L., Leisawitz, D. T., Liu, F., Mainzer, A. K., McLean, I. S., Padgett, D. L., Skrutskie, M. F., Gelino, C. R., Beichman, C. A., and Juneau, S. (2015). The Most Luminous Galaxies Discovered by WISE. *ApJ*, 805(2):90.

van den Bosch, R. C. E. (2016). Unification of the fundamental plane and Super Massive Black Hole Masses. *ApJ*, 831(2):134.

van den Bosch, R. C. E., Gebhardt, K., Gültekin, K., Yıldırım, A., and Walsh, J. L. (2015). Hunting for Supermassive Black Holes in Nearby Galaxies With the Hobby-Eberly Telescope. *ApJS*, 218(1):10.

Vavilova, I. B., Dobrycheva, D. V., Vasylenko, M. Y., Elyiv, A. A., Melnyk, O. V., and Khramtsov, V. (2021). Machine learning technique for morphological classification of galaxies from the SDSS. I. Photometry-based approach. *A&A*, 648:A122.

Vavilova, I. B., Khramtsov, V., Dobrycheva, D. V., Vasylenko, M. Y., Elyiv, A. A., and Melnyk, O. V. (2022). Machine learning technique for morphological classification of galaxies from SDSS. II. The image-based morphological catalogs of galaxies at 0.02<z<0.1. *Kosmichna Nauka i Tekhnologiya*, 28(1):03–22.

Véron-Cetty, M. P. and Véron, P. (2010). A catalogue of quasars and active nuclei: 13th edition. *A&A*, 518:A10.

Virtanen, P., Gommers, R., Oliphant, T. E., Haberland, M., Reddy, T., Cournapeau, D., Burovski, E., Peterson, P., Weckesser, W., Bright, J., van der Walt, S. J., Brett, M., Wilson, J., Millman, K. J., Mayorov, N., Nelson, A. R. J., Jones, E., Kern, R., Larson, E., Carey, C. J., Polat, İ., Feng, Y., Moore, E. W., VanderPlas, J., Laxalde, D., Perktold, J., Cimrman, R., Henriksen, I., Quintero, E. A., Harris, C. R., Archibald, A. M., Ribeiro, A. H., Pedregosa, F., van Mulbregt, P., and SciPy 1.0 Contributors (2020). SciPy 1.0: Fundamental Algorithms for Scientific Computing in Python. *Nature Methods*, 17:261–272.

Wang, F., Yang, J., Fan, X., Hennawi, J. F., Barth, A. J., Banados, E., Bian, F., Boutsia, K., Connor, T., Davies, F. B., Decarli, R., Eilers, A.-C., Farina, E. P., Green, R., Jiang, L., Li, J.-T., Mazzucchelli, C., Nanni, R., Schindler, J.-T., Venemans, B., Walter, F., Wu, X.-B., and Yue, M. (2021). A Luminous Quasar at Redshift 7.642. *ApJ*, 907(1):L1.

Wang, L., Xu, D., Gao, L., Guo, Q., Qu, Y., and Pan, J. (2019). Comparing galaxy morphology in hydrodynamical simulation and in semi-analytic model. *MNRAS*, 485:2083–2091.

Waskom, M. L. (2021). seaborn: statistical data visualization. *Journal of Open Source Software*, 6(60):3021.

Whyte, L. F., Abraham, R. G., Merrifield, M. R., Eskridge, P. B., Frogel, J. A., and Pogge, R. W. (2002). Morphological classification of the OSU Bright Spiral Galaxy Survey. *MNRAS*, 336(4):1281–1286.

Willett, K. W., Lintott, C. J., Bamford, S. P., Masters, K. L., Simmons, B. D., Casteels, K. R. V., Edmondson, E. M., Fortson, L. F., Kaviraj, S., Keel, W. C., Melvin, T., Nichol, R. C., Raddick, M. J., Schawinski, K., Simpson, R. J., Skibba, R. A., Smith, A. M., and Thomas, D. (2013). Galaxy Zoo 2: detailed morphological classifications for 304 122 galaxies from the Sloan Digital Sky Survey. *MNRAS*, 435(4):2835–2860.

Willmer, C. N. A. (2018). The Absolute Magnitude of the Sun in Several Filters. *ApJS*, 236(2):47.

Wright, E. L., Eisenhardt, P. R. M., Mainzer, A. K., Ressler, M. E., Cutri, R. M.,

Jarrett, T., Kirkpatrick, J. D., Padgett, D., McMillan, R. S., Skrutskie, M.,
Stanford, S. A., Cohen, M., Walker, R. G., Mather, J. C., Leisawitz, D., Gautier,
Thomas N., I., McLean, I., Benford, D., Lonsdale, C. J., Blain, A., Mendez,
B., Irace, W. R., Duval, V., Liu, F., Royer, D., Heinrichsen, I., Howard, J.,
Shannon, M., Kendall, M., Walsh, A. L., Larsen, M., Cardon, J. G., Schick, S.,
Schwalm, M., Abid, M., Fabinsky, B., Naes, L., and Tsai, C.-W. (2010). The
Wide-field Infrared Survey Explorer (WISE): Mission Description and Initial
On-orbit Performance. *AJ*, 140(6):1868–1881.

Yao, H. F. M., Jarrett, T. H., Cluver, M. E., Marchetti, L., Taylor, E. N., Santos,
M. G., Owers, M. S., Lopez-Sanchez, A. R., Gordon, Y. A., Brown, M. J. I.,
Brough, S., Phillipps, S., Holwerda, B. W., Hopkins, A. M., and Wang, L.
(2020). Galaxy and Mass Assembly (GAMA): A WISE Study of the Activity of
Emission-line Systems in G23. *ApJ*, 903(2):91.

Yao, Y., Ravi, V., Gezari, S., van Velzen, S., Lu, W., Schulze, S., Somalwar, J. J.,
Kulkarni, S. R., Hammerstein, E., Nicholl, M., Graham, M. J., Perley, D. A.,
Cenko, S. B., Stein, R., Ricarte, A., Chadayammuri, U., Quataert, E., Bellm,
E. C., Bloom, J. S., Dekany, R., Drake, A. J., Groom, S. L., Mahabal, A. A.,
Prince, T. A., Riddle, R., Rusholme, B., Sharma, Y., Sollerman, J., and Yan,
L. (2023). Tidal Disruption Event Demographics with the Zwicky Transient
Facility: Volumetric Rates, Luminosity Function, and Implications for the Local
Black Hole Mass Function. *ApJ*, 955(1):L6.